Pure Bending Characterization of Nb$_3$Sn Superconducting Strands Using Experimentation and FEA Modeling

Submitted By

Nathaniel Allen
B.S. Mechanical Engineering (2011)
University of New Hampshire

In partial fulfillment of the requirements for the degree of

Master of Science in Mechanical Engineering

Tufts University
School of Engineering
Medford, Massachusetts

May 2013

Author …………………………...   Certified By …………………………...
Nathaniel Allen   Dr. Gary Leisk
Department of Mechanical Engineering   Senior Lecturer, Tufts University
Tufts University   Department of Mechanical Engineering

Certified By …………………………...   Certified By …………………………...
Dr. Luisa Chiesa   Dr. Makoto Takayasu
Assistant Professor, Tufts University   Research Scientist, MIT
Department of Mechanical Engineering   Plasma Science and Fusion Center
Research Advisor

Abstract

Superconductors are important technological materials for developing high field magnets. Nb_3Sn is a particularly common superconducting material for these magnets because of its high current and field capabilities. However, Nb_3Sn is also very sensitive to strain which can degrade its electrical performance. For this reason, the strain-dependent behavior of Nb_3Sn has been an important research topic for many decades. This thesis focuses on characterizing the strain-dependent behavior of Nb_3Sn strands under pure bending loads. This work is the continuation of pure bending research that started in 2005 at the MIT.

A discrepancy in the critical current results of two different sample holders at the same amount of applied bending was observed in prior pure bending experiments conducted in 2012. The unknown cause behind this discrepancy led to the focus and motivation behind the current pure bending research.

An in-depth FEA investigation of the samples holders was undertaken to identify a potential cause for the observed difference in experimental critical current results. The FEA modeling focused on characterizing the strain distributions within the Nb_3Sn strands mounted on the sample holders. A comparison between the critical current results and the strain distributions from each sample holder uncovered an adverse characteristic which may have caused the discrepancy.

Following these findings improved sample holders were designed to eliminate this adverse characteristic. The performance of the newly developed sample holders

were then validated through experiments. Both bronze-route and internal-tin type Nb$_3$Sn strands were tested up to an applied bending strain of 1.25% on the strand surface. Both type of samples exhibited consistent critical current degradations over the entire bending range. No discrepancies were found between the low and high bending range sample holders.

The Nb$_3$Sn samples tested all experienced a reduction in critical current between 40% and 60% at the maximum bending strain of 1.25%. The internal-tin samples experienced filament breakage and saw a permanent 30% reduction in critical current upon removal of bending. The critical current of the bronze-route samples was completely recoverable and returned to its initial critical current value upon removal of the bending strain.

The experimental results of the critical current as a function of applied pure bending were evaluated with an existing integrated model. The behavior of the samples was characterized and found to be on par with previous findings for internal-tin and bronze-route wire.

Acknowledgements

I want to convey my deepest appreciation to all those who contributed to the completion of this thesis. Most importantly I want to thank my advisor, Dr. Luisa Chiesa for all of her support, guidance and mentorship. I could always find relief knowing her door was open even in the midst of her busy schedule.

I am also very grateful for the guidance and help given by Dr. Makoto Takayasu along the way. I have learned many things and gained much from his advice, wisdom and expertise. I would also like to thank Dr. Gary Leisk who has been a helpful mentor to me during my graduate studies and has provided important insight into this thesis.

I am extremely grateful to my fiancée, Maren Gray who has fully supported me throughout this journey. I find comfort knowing she is always there for me and always has my back. I also want to thank my family who has always played a vital role in my life and will support me through anything.

Table of Contents

List of Figures

5.0   Sample Holder Optimization

6.0   Experimentation and Results

List of Tables

Nomenclature

A –   ampere
B –   magnetic flux density
CICC –   Cable-in-Conduit Conductor
DAQ –   data acquisition
E –   electric field
FEA –   finite element analysis
ft –   feet
H_c –   critical magnetic field
HIT –   Hitachi Cable, Ltd.
HTS –   high temperature superconductor
I –   current
I_c –   critical current
I_{c0} –   baseline critical current
J_c –   critical current density
K –   kelvins
kg –   kilogram
LTS –   low temperature superconductor
m –   meter
mm –   millimeter
Nb_3Sn –   niobium-tin
NHMFL –   National High Magnetic Field Laboratory
T –   tesla
T_c –   critical temperature
OST –   Oxford Superconducting Technology
V –   volt
μV –   microvolt

1.0 Introduction

1.1 Thesis Objective

The research presented in this thesis is focused on the current work that has been done to characterize the strain-dependent behavior of Nb_3Sn superconducting stands under pure bending loads. The strain behavior is characterized using a continuously variable bending mechanism design by David Harris in 2005 [1]. The device works by placing the superconducting strands on a thin beam-like sample holder that can be bent through a continuous evolution of bending states. This allows a single strand to be characterized over a large range of bending strains using a single device.

Prior experiments conducted in 2012 by Joe King discovered a discrepancy in critical current values for the same sample tested in two different samples holders at the same amount of applied bending [2]. This has given rise to the focus of the current research, which is to identify the cause of this discrepancy by fully analyzing the characteristics and behavior of the current sample holders using finite element analysis (FEA). The goal of the analysis is to determine any potential shortcomings in the sample holder designs by detecting any differences that may exist in the strain-state of their Nb_3Sn samples. Any difference in the magnitude, uniformity or overall strain could help explain the discrepancy in critical current results.

The end objective of this work is to develop new and improved sample holders

which eliminate the differences in critical current results found prior. The sample holders will be optimized so that they place the samples in an acceptable state of true "pure bending." The newly developed sample holder will be validated through critical current experiments done at the National High Magnetic Field Laboratory in Tallahassee, FL. The ideal outcome of the experiments will be to collect accurate and dependable critical current data which can be used to improve the current predicative scaling laws for Nb_3Sn magnet design, allowing for more advanced superconducting magnets to be developed.

1.2 Background of Superconductivity

A superconductor is defined as a material with the ability to conduct electrical current without resistance. This behavior is made possible by the Meissner Effect which is a superconductor's ability to expel magnetic fields from within the material. Dutch physicist Kamerlingh Onnes discovered this phenomenon in 1911, three short years after he successfully liquefied helium. He made the discovery while testing the temperature dependence of resistance within a sample of mercury. As Onnes lowered the temperature below 4 kelvins (K), he noticed that the resistance within the sample suddenly dropped to zero. In response to this discovery he wrote, "Mercury has passed into a new state, which on account of its extraordinary electrical properties may be called the superconductive state" [3].

Onnes soon discovered several other materials that also exhibited this superconductive state under appropriate conditions. These appropriate conditions led to the discovery that a material's superconductive state is governed not only

by its temperature but also by the magnetic field and current. The transition

between the superconductive and normal resistive states for a superconductor is

controlled by three critical values: the critical temperature (T_c), critical magnetic

field (H_c), and critical current density (J_c). The magnitudes of these critical

properties are specific to each individual superconducting material. These

governing parameters can be plotted together to create what is called a critical

surface, as shown in Figure 1.1.
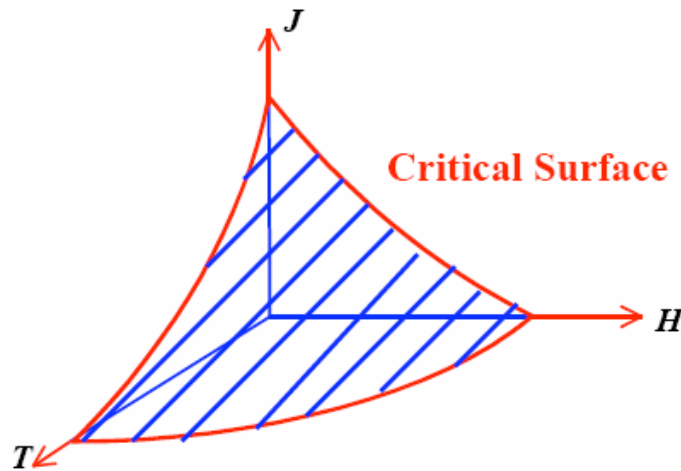
Figure 1.1 – Characteristic critical surface of a superconductor.

If a superconductor remains on or beneath this critical surface it will remain in a

superconductive state; however, if any one of the parameters varies outside of the

surface the superconductor will quench. A quench refers to the rapid transition of

a superconductor to a resistive state. A superconductor is generally operated a

safe amount beneath the surface to accommodate small fluctuations in each

parameter without quenching.

Superconductors are often grouped into two categories based on their critical

temperature. High temperature superconductors (HTS) have critical temperatures

above 77 K, while low temperature superconductors (LTS) have critical

temperatures below 77 K [3]. This transition temperature of 77 K signifies the

boiling point of liquid nitrogen at atmospheric pressure. One common LTS is

Nb_3Sn, which has a critical temperature of 18.2 K and a max critical field of 24.5

T at a temperature of 4.2 K. Most LTS are cooled using liquid helium as was done

in the initial experiments conducted by Onnes.

The original superconducting materials that were identified by Onnes and his

colleagues are classified as Type-I superconductors and are mostly pure metals.

These superconductors could not carry any appreciable current under low

magnetic fields. Type I superconductors are classified as having one critical

magnetic field value, at which point the Meissner effect completely breaks down

and the material becomes resistive. The applicability of superconductors for high

power applications came with the development of Type II superconductors.

Type II superconductors are a mixture of Type I superconductors and normal

resistive materials. The resistive material allows magnetic flux lines to locally

penetrate the material without destroying its overall superconductive state. This

phenomenon allows materials to remain superconductive at higher magnetic fields

while carrying substantial amounts of current.

These Type II superconductors are classified as having two critical field values

(lower and upper). Below the lower critical field (H_{c1}) the superconducting

material exhibits perfect diamagnetism as described by the Meissner effect. In

between the two critical fields, the material will experience partial magnetic flux

penetration while remaining in a superconductive state. Above the upper critical field (H_{c2}) magnetic flux lines fully penetrate the superconducting material returning it to the normal resistive state. The upper magnetic field value is used to denote the critical surface for these type superconductors [4].

1.3 Applications of Superconductivity

Since its discovery in 1911, the unique phenomenon of superconductivity has sparked interest in many scientists as to its future widespread applications. Although superconductivity is an extremely beneficial technology its widespread implementation has only recently become more practical for certain applications as our understanding of the properties and behavior of superconducting materials increases. The largest application for superconductors is electromagnets. Powerful new superconducting magnets can be made much smaller than a resistive magnet, because the windings can carry large currents with no energy loss and therefore can achieve greater magnetic fields.

1.3.1 High-Field Magnets

High-field magnet industries have become one of the largest areas for widespread use of superconducting materials. Particle accelerators used in high-energy physics are one primary application for these superconducting magnets. The world's largest accelerator is the Large Hadron Collider (LHC) built in Geneva which contains over 1,500 of these high-field magnets [5]. Another primary application of high-field superconducting magnets is in fusion energy. The high

temperature plasma in a fusion reactor is generally contained using a magnetic confinement system composed of large superconducting magnets. Fusion reactions have been demonstrated in the past and have shown promise of one day being a clean and abundant energy source. The International Thermonuclear Experimental Reactor (ITER) is an international collaborative project aimed at demonstrating the feasibility of fusion energy for power generation. ITER has been the motivation behind this research and will be discussed more in the following section.

1.3.2   Magnetic Resonance Imaging (MRI)

Superconducting electromagnets have already become crucial components of medical imaging systems and are specifically well suited for magnetic resonance imaging (MRI) machines. Superconducting magnets are desirable in this application because they provide a very stable high magnetic field over a large volume. In addition to this, they require less electrical power compared to conventional magnets.

Advances in medical imaging systems are giving doctors greater ability to diagnose medical problems and therefore are becoming more prevalent. The growing demand for MRI machines makes this industry one of the largest branches of superconducting applications [6].

1.3.3   Magnetic Levitation

In the railroad and high-speed commuter train industries, magnetic levitation

transport is an emerging field that has shown significant promise. The ability to create small high-field magnets using superconductors make them the primary choice magnetic system used to levitate, guide and propel the trains. Magnetically levitated trains would eliminate the need for wheels and moving components which are constantly deteriorating by high loading and friction. These trains would also have the ability to travel smoother at higher speeds. If magnetic levitation becomes more widespread it has the ability to greatly change the transportation industry [7].

1.3.4   Power Distribution and Storage

Superconductivity could play an integral part of our power distribution system in the near future. Superconducting electrical transmission lines have been shown to exploit a superconductor's ability to conduct electricity with zero resistance and have greatly reduced transmission losses. They have also greatly reduced the amount of transmission lines necessary by exploiting the high current capabilities of superconductors.

Along with this, superconductors could also be used to upgrade conventional high voltage transformers. And most importantly, superconducting magnet energy storage (SMES) systems currently have the ability to store a large capacity of energy for indefinite periods of time while still having fast discharge rates. Greater implementation of these SMES systems would increase the power grid's ability to accommodate more non-continuous power sources like renewable energy [6].

7

1.4 Importance of Nb$_3$Sn Research

Niobium-tin (Nb$_3$Sn) is a Type-II low temperature superconductor that was discovered in the 1950's and developed into a feasible magnet conductor in the late 1970's. Nb$_3$Sn is a high-quality superconducting material because of its ability to have high critical current at very large magnetic fields, greater than 20 teslas at 4.2 K. These impressive electrical attributes make it one of the few superconducting materials that can meet the extreme demands of high field magnet applications.

As mentioned above, one of the most currently active areas for high field Nb$_3$Sn magnets is the development of the magnetic plasma confinement system for ITER's fusion reactor presently being constructed in Cadarache, France. The magnetic confinement system is a tokamak design which contains the plasma in the shape of a torus. A computer model of the tokamak design for the ITER experimental reactor is shown in Figure 1.2 on the following page. For a sense of scale, a person is standing at the bottom of the image.

Figure 1.2 clearly indicates the three main components of the magnetic confinement system which are the 18 superconducting toroidal field coils, 6 poloidal field coils and the large central solenoid consisting of 6 modules. A special alloy of Nb$_3$Sn has been selected as the superconducting material for the toroidal field and central solenoid magnet coils [8]. Therefore, the majority of the magnetic system uses Nb$_3$Sn superconductors making it an essential component of the overall magnet confinement system.
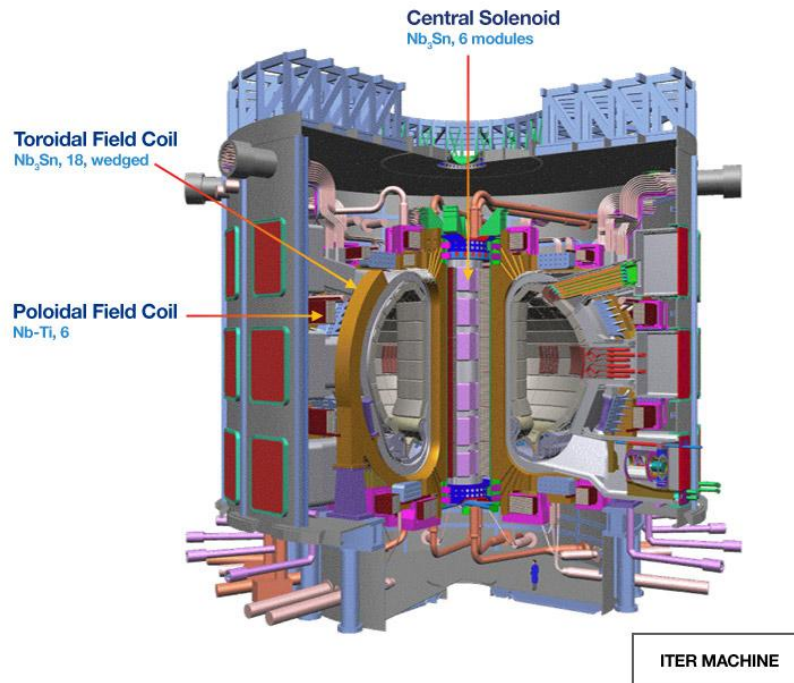
Figure 1.2 – Computer rendered schematic of the ITER fusion reactor [9].

The Nb_3Sn magnet components indicated above will be constructed using cable-in-conduit conductors (CICC) containing more than 800 superconducting strands. These CICCs are described in more details in the following section and are shown in Figure 1.3. High current test of the central solenoid magnet coils has shown lower maximum current than the design expectation [10]. Considering the major role these magnets play in the fusion reactor, meeting their design specifications is a crucial requirement for the future success of the ITER project. Therefore, the limited current results gave rise to a large amount of research aimed at understanding the potential causes.

Although Nb_3Sn's strain sensitivity is known, its performance under complex loading conditions, like a magnet winding, is not. A superconducting strand within a CICC is experiencing a compound strain-state which may be any

combination of axial, bending and transverse compressive stains. To fully understand how the strands are being affected, each type of loading has been investigated independently. Prior research has already been done on Nb_3Sn under axial tension and compression, which is why characterizing Nb_3Sn under transverse compression and bending loads is essential and has been the focus of current research. Once the strain-dependent behavior of Nb_3Sn strands under these loading conditions has been fully characterized, this information can be used to improve the current scaling laws. These scaling laws are designed to predict the overall performance of a CICC magnet coil based on the results of a single strand. Therefore, the improved scaling laws will more accurately predict the performance of the ITER model coils. With this information, magnets that meet or exceed all ITER design requirements can be created.

1.5 Cable-in-Conduit Conductor (CICC)

A cable-in-conduit conductor (CICC) is a cabled superconductor that is placed within a metal conduit and is cooled by a forced flow of a liquid cryogenic. It is regarded as a standard cabled-conductor design for large magnet applications since it can meet all key requirements. It is for this reason that this cabling technique has been chosen for the ITER model magnetic coils of the central solenoid and toroidal field magnets.

In general, CICC designs are composed of a high-strength metal jacket for mechanical support, a method for cooling the superconducting strands and an electrically conductive stabilizing material. The ITER conductors use bronze-

route and internal-tin type Nb_3Sn strands for their superconductor and copper wire as their stabilizing material for quench protection. The cooling method is achieved through a central cooling channel that carries a forced flow of liquid helium through the conductor. A specially developed stainless steel is used for the high-strength conduit material in ITER model CICC.

The strands are combined using precise several stage twisting technique designed to reduce electrical losses and achieve optimal performance. The overall twist pattern for the ITER CICC is 3x-3x-4x-5x-6x. This indicates the number of groups twisted together at each stage of winding. Initially three strands are twisted together into a group. Then three of those groups are twisted together. This continues until there are 6 bundles remaining as indicated in the images in Figure 1.3. The final six bundles are twisted around a central cooling channel and then placed inside the conduit which is compressed around the twisted cable. A cross-section of the final ITER CICC cable is shown in Figure 1.3 below.

Figure 1.3 – Cable-in-Conduit Conductors (CICC) for ITER magnets [11].

Due to the strain sensitivity and brittle nature of the Nb_3Sn material, the CICC cables are assembled using unreacted strands. Unreacted strands refer to non-heat treated Nb_3Sn wires which contain isolated niobium and tin materials as described more in the following section. After the CICC is fully assembled it goes through a long heat treatment process which diffuses the niobium and tin materials in the strands together creating the superconductive compound Nb_3Sn. For the ITER magnets this heat treatment is done after the CICC has been formed into the magnet coils to prevent any damage that may be caused during winding.

1.6 Production of Nb_3Sn

Superconducting wires are not composed purely of superconducting material, but rather a combination of resistive and superconductive materials. Most LTS, like Nb_3Sn are comprised of a copper stabilizing layer surrounding a central region of superconducting filaments. Copper is most often chosen as the stabilizing material because it is a highly ductile material that has excellent electrical conductivity.

The standard method that is used for producing superconducting wires starts by combining all the raw materials into a large billet as seen in Figure 1.4. For Nb_3Sn wire, these materials include niobium and some form of tin for the superconductor, copper for the stabilizer, and usually tantalum for a diffusive barrier. The billet then goes through a number of extruding, annealing (if applicable) and drawing steps until the final desired diameter is achieved. The strands then go through a long heat treatment process that takes place to diffuse the niobium and tin together creating the superconducting Nb_3Sn filaments. The

reacted wire is very brittle and sensitive to strain which is why the heat treatment process is generally done after the wire is in its final form.
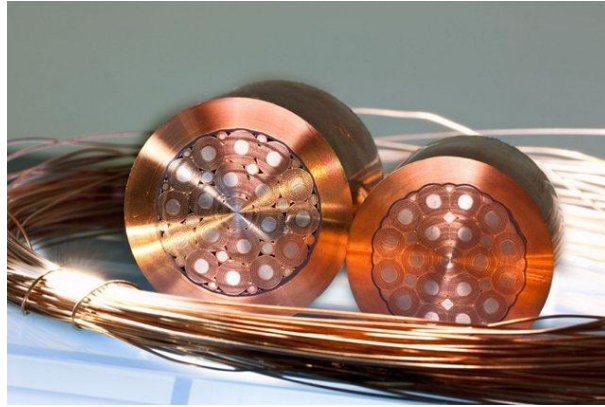
Figure 1.4 – ITER type Nb₃Sn billets before being drawn into wire form [12].

The exact design and manufacturing technique for producing these superconducting wires is critical to the performance of the strand and consequently the performance of the entire conductor. Numerous methods exist for developing superconducting wires; however, only two methods relevant to this research will be discussed. These are the bronze-route and internal-tin processes.

The bronze-route process starts with small billets of bronze which is an alloy of copper and tin. A pattern of holes are drilled into the billet and are filled with a pure niobium alloy. These small billets are then extruded and drawn into hexagonal shapes as seen in Figure 1.5. Multiple hexagonal billets are then drawn together into a bundle and placed inside a hollow copper tube with a thin tantalum barrier inside. The entire assembly is then extruded and drawn down to the final diameter of the superconducting wire. This is referred to as unreacted Nb_3Sn wire which then undergoes a heat treatment process to diffuse the tin out of the bronze reacting it with the pure niobium creating the Nb_3Sn superconducting filaments.
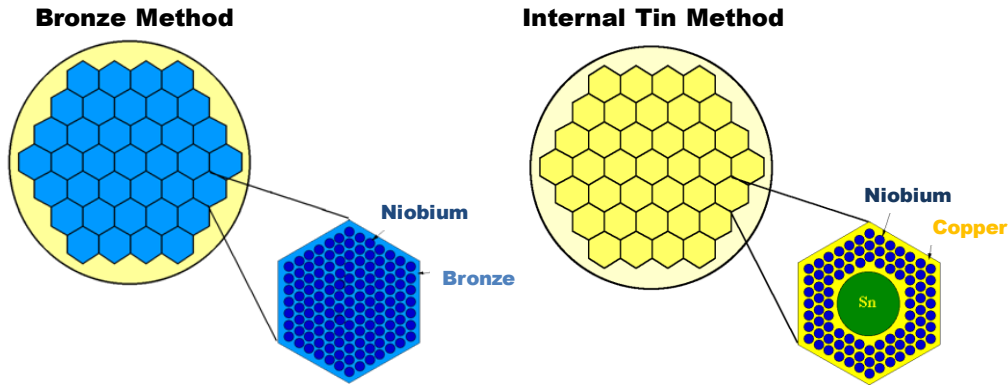
Figure 1.5 – Schematics of the bronze-route and internal-tin methods.

The internal-tin process starts with a pure copper billet. Holes are drilled and filled with tubes of niobium and tin. Generally a pattern similar to Figure 1.5 is used which has one large central hole for the tin and many smaller surrounding holes for niobium. These billets are then drawn into hexagonal shapes and bundled together. This bundle is again placed inside a hollow copper tube with a diffusive tantalum barrier and drawn to its final diameter. Lastly, the strand is heat treated which causes the tin to diffuse through the copper and into the surrounding niobium tubes creating Nb_3Sn filaments.

1.7 Strain Characterization of Nb_3Sn

Mechanical strain has been discovered to significantly affect the performance and stability of superconducting materials. This strain sensitivity is a big limitation to Nb_3Sn and must be considered during the design of a superconducting magnet. Currently Nb_3Sn coils are designed using the universal predictive scaling law developed by Ekin [13]. The scaling law predicts the behavior of full scale magnets based on the strain-dependent behavior of single Nb_3Sn strands.

Although this scaling law is useful, it is not exact and is based on the limited experimental data that is available. Most of the available experimental data are for axial compression and tension affects. Therefore, the scaling law will become more accurate with an increased amount of experimental data. This is why research continues to focus on determining the strain-dependent behavior of Nb_3Sn strands under loading; specifically transverse compression and bending.

The effect of bending on critical current of Nb_3Sn strands was first studied by Senkowicz, Takayasu and Lee [14]. Their experiments were conducted using a fixed bending device that statically tested strands at one bending state at a time. The samples were initially heat treated and then manually placed in the channel of the sample holder. The sample holder was then gently clamped down on the strand placing it into the appropriate bending curvature. This research covered a wide range of bending strains up to 1.4% strain on the strand surface using multiple sample holders, each with a specific bending curvature.

The one main drawback of this bending characterization technique was its inability to vary the bending applied to the sample. Every sample only experienced one bending state, which consequently limited the amount of data that could be taken to characterize the samples under bending loads. This limitation led to the development of a new variable-strain bending device designed by Harris [1]. This variable-strain device allows samples to be continuously bent through an evolution of bending states. This new device is the focus of this research and will be described in details in the following sections.

2.0 Pure Bending Mechanism

The pure bending mechanism was originally designed and built by David Harris at the Massachusetts Institute of Technology (MIT) in 2005 [1]. The probe, gear system and general procedure from his experiment have been the basis of all research that has followed. Since his work in 2005 three other graduate students have worked on this research and have run experiments using his device. Allegritti and Mallon both added design improvements to the sample holders, which will be discussed more in the succeeding sections.

2.1 Test Conditions

Pure bending critical current tests of Nb_3Sn superconducting strands were done at the National High Magnetic Field Laboratory (NHMFL) in Tallahassee, Florida. The experiments were conducted in a 20 teslas (T), Bitter resistive magnet with a 195 mm (7.68 inch) diameter warm bore. A cryostat was used inside the magnet to provide an environment suitable for performing cryogenic tests on LTS samples. The cryostat reduces the available magnet bore diameter to only 170 mm (6.70 inches). Magnetic field intensities during experimentation ranged from 12 to 15 T. During testing the electrical current in the background magnetic field induces an electromagnetic Lorentz load on the sample. An average critical current value for ITER type Nb_3Sn strands is 300 amperes (A) at 4.2 K in a 12 T field. These conditions would produce a Lorentz load of 420 N (95 lbf) on the 116.4 mm (4.58 inch) long test sample.

A schematic of the cryostat is shown below in Figure 2.1. The red region indicates the Bitter resistive magnet, the blue region represents the inner chamber of the cryostat and the yellow region represents the outer cryostat chamber. The inner chamber is filled with liquid helium to cool the test samples while the outer chamber is filled with liquid nitrogen to facilitate cooling and reduce boil-off of the helium. The field produced by the magnets can vary near its top and bottom. For this reason, the samples are tested in the middle of the magnet, as indicted below, which provides the most uniform field. The distance from the top of the cryostat to the middle of the magnet is 1883 mm (74.13 inches).
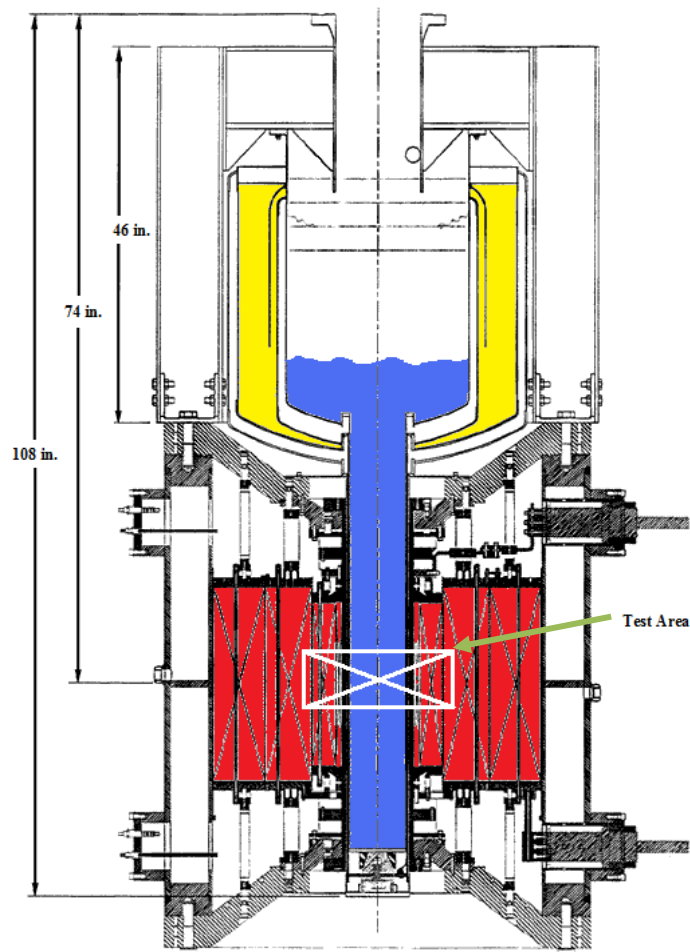
Figure 2.1 – Schematic of magnet and cryostat assembly at NHMFL.

17

2.2 Probe Design

As mentioned above, the samples are tested in the middle of the magnet which provides the most uniform and stable field during testing. Placing the samples at the correct location is achieved using a long probe which contains the bending mechanism mounted at the bottom. The probe is placed within the inner chamber of the cryostat as indicated in Figure 2.1. It extends down into the magnet bore placing the samples at center of the magnet, also represented in Figure 2.1. The probe not only places the samples at the appropriate location but also the correct orientation with the field.

A picture of the probe is provided in Figure 2.2. The round stainless steel plate at right of the picture is the bottom of the bending mechanism. The larger stainless steel plate located at the other end of the probe is the cryostat mounting plate. Below the mounting plate is pink foam which insulates the inner chamber of the cryostat reducing the amount of helium boil-off. The structure of the probe is built using stainless steel rods and G10 plates.
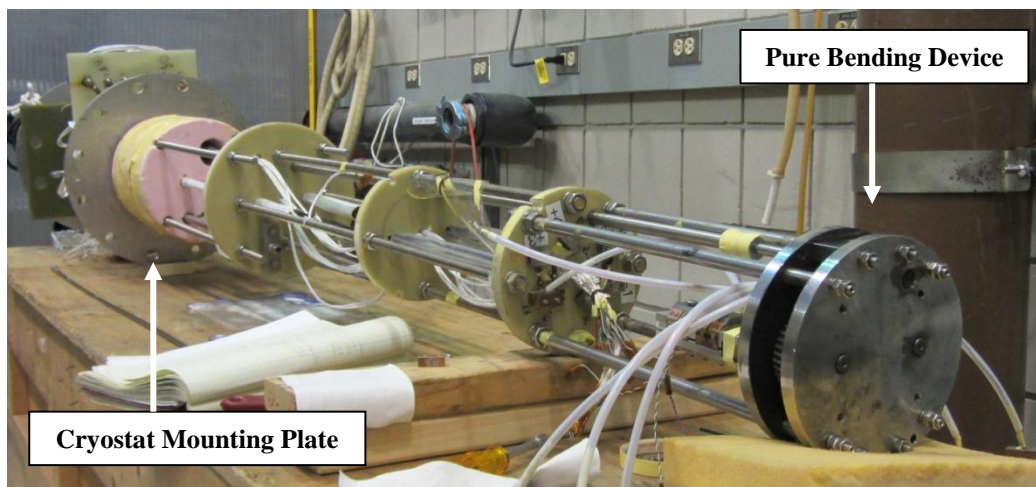
Figure 2.2 – Image of pure bending device mounted to the probe used in experiments.

The probe not only places the samples at the correct location it also provides a means of remotely accessing the bending mechanism. This allows us to make adjustments to the applied bending load without having to remove the probe. This is achieved using a long input shaft that runs the length of the probe. At the bottom it attaches to the gear box of the bending mechanism and at the top it connects to a DC motor located outside the cryostat.

In addition to this, the probe also provides the necessary framework for all wiring and instrumentation that is needed for the experiments. The probe carries the liquid helium fill tube, the helium level sensors, the current leads and the wiring for the voltage taps. Lastly, the probe acts as the rigid mechanical structure which holds the pure bending mechanism stationary during testing. It achieves this by resisting the electromagnetic forces that are generated on the pure bending device during testing.

2.3 Bending Mechanism

The bending mechanism refers to the device that applies the bending loads to the Nb_3Sn samples. As mentioned previously, the device was developed by Harris and is depicted in the Figure 2.3. The design consists of two main components; the sample holder mounting assembly and the gear box. Details of these two components are given in the following sections.

The bending device works by converting the rotation from the vertical input shaft into bending of the sample holder. This is achieved through a gear train consisting

of two continuous worm drives. The rotation of the input shaft is provided by a DC motor located on top of the probe. The vertical input shaft runs from the DC motor at the top of the probe to the gear box at the bottom. The rotation of the input shaft drives the gear train which produces the bending of the device.
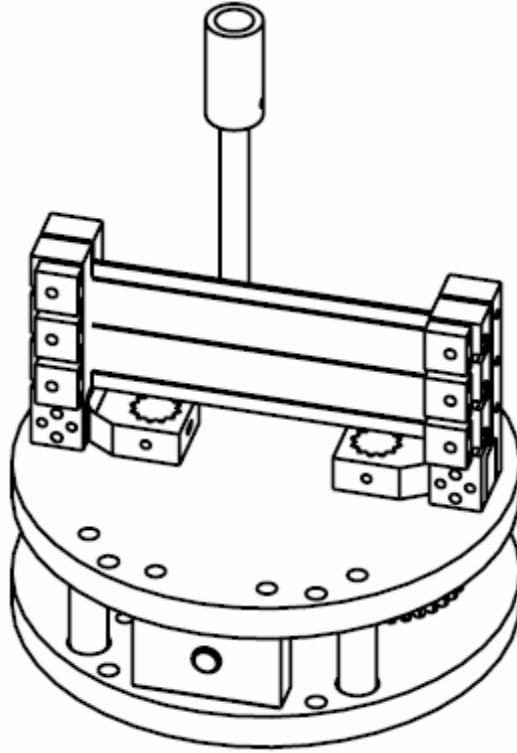
Figure 2.3 – Wire frame image of the pure bending mechanism [1].

2.3.1 Gear Box

The gear box is located beneath the sample mounting assembly and contains the entire gear train which is comprised of two continuous worm drives. The gear train is depicted in Figure 2.4, which shows a wire frame schematic of the entire gear train. All components of the gear train and its housing are made out of austenitic 316 grade stainless steel because of its high strength at cryogenic temperatures and low magnetic permeability.
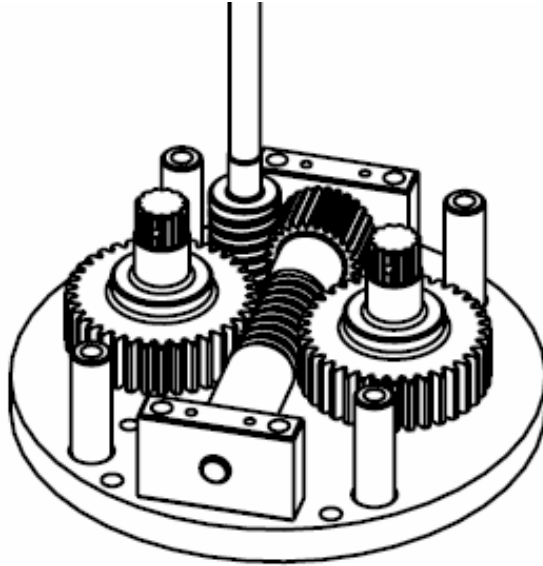
Figure 2.4 – Wire frame image of the gear train components [1].

The gear train begins with the rotation of the input shaft. At the end of the input shaft is a worm, which is a screw like gear. The worm on the input shaft meshes with the worm gear located on the end of a central drive shaft, creating the first worm drive. This drive converts the vertical rotation of the input shaft into the horizontal rotation of the drive shaft.

Located in the middle of the drive shaft is another worm, screw-like gear. This worm meshes with two more worm gears, one on either side of the drive shaft. These worm gears are located on the vertical torque shafts that transmit the rotation out of the gear box. This generates the second worm drive which converts the horizontal rotation of the drive shaft into two opposite vertical rotations of the torque shafts. The overall gear ratio of the device is 972 to 1.

2.3.2 Sample Mounting Assembly

The sample mounting assembly consists of 4 components; the sample holder,

current terminals, vertical supports and torque arms. As the torque arms rotate in

opposite directions they produce a moment on the ends of the sample holder

causing it to bend. A schematic of the sample mounting assembly with the

absence of torque arms can be seen in Figure 2.5. In this figure the sample holder

is shown in grey, the current terminals are shown in bronze and the vertical

supports are shown in blue.
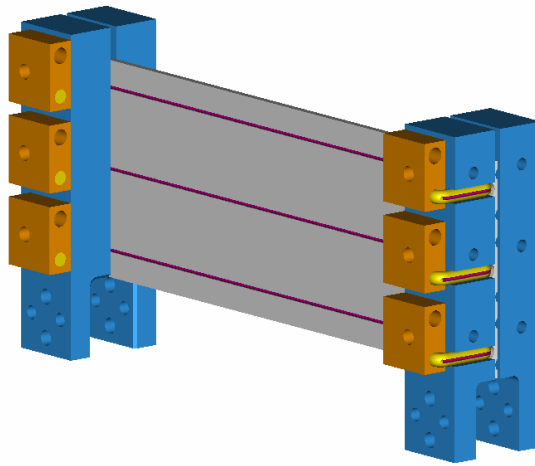
Figure 2.5 – CAD rendering of the sample mounting assembly.

The sample mounting assembly is built by first joining the current terminals to the

ends of the sample holder. Following this, the Nb_3Sn superconducting samples are

mounted. The samples are mounted in their unreacted state so that no damage is

done to the wire while mounting. The samples are then heat treated on the sample

holder, to create the Nb_3Sn filaments within the wire. After the samples are heat

treated, the vertical supports are attached to the ends of the sample holder. The

whole sub-assembly is then mounted on the torque arms. The two torque arms are

first attached to the torque shafts coming out of the gear box to ensure appropriate

orientation, as shown in Figure 2.6.

22
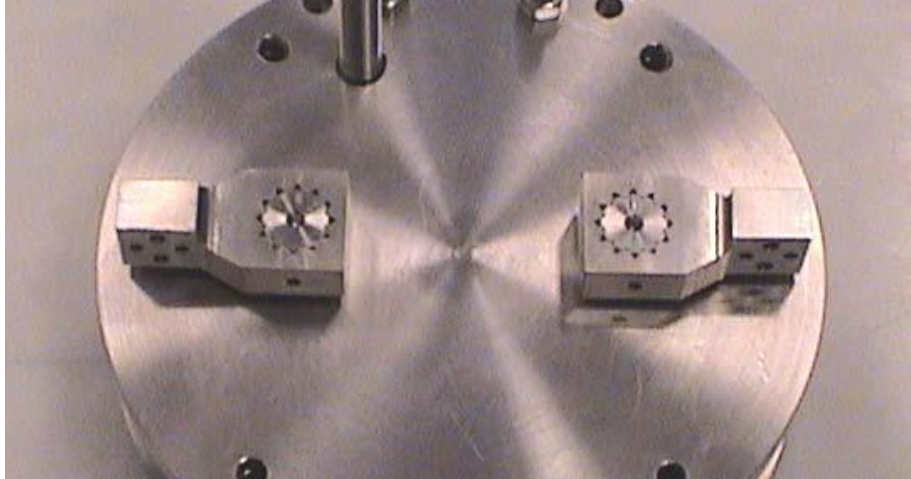
Figure 2.6 – Torque arms mounted to the torque shafts exiting the gear box.

Sample Holder

The sample holder is the thin flat beam that is depicted in grey in Figure 2.5.

Because it holds the superconducting test samples, it is of critical importance. It is

the one component that places the strand into a state of bending and the only

component that can resist the Lorentz loads that develop on the strands. For this

reason, the sample holder must be strong enough to resist the large bending

stresses. It must also have a coefficient of thermal expansion similar to that of

Nb_3Sn, to insure that the superconducting strands are not pre-strained during cool

down. The titanium alloy Ti-6Al-4V was chosen to have the best combination of

properties for the sample holder. The original bending mechanism contained one

large sample holder (as shown in the figure) while the modern designs host two

smaller sample holders held together by the vertical supports. More details and

images of the sample holders will be given in the succeeding sections.

Current Terminals

The current terminals are mounted to the ends of the sample holder and provide

the means of transitioning the current from the current leads to the

superconducting strands. The design of the terminals plays an important role in

the amount of current transferred to the samples and in the distribution of current

within the samples. The terminals are made out of oxygen-free copper (OFC) to

facilitate good electrical performance. In Figure 2.5 the copper terminals are

indicated by the three bronze colored square cubes protruding from the ends of

the sample holder. Newer current terminals can also be seen in Figure 2.7

mounted to the newest sample holders. The terminals employee a U-shaped

design to increase the current transfer length.
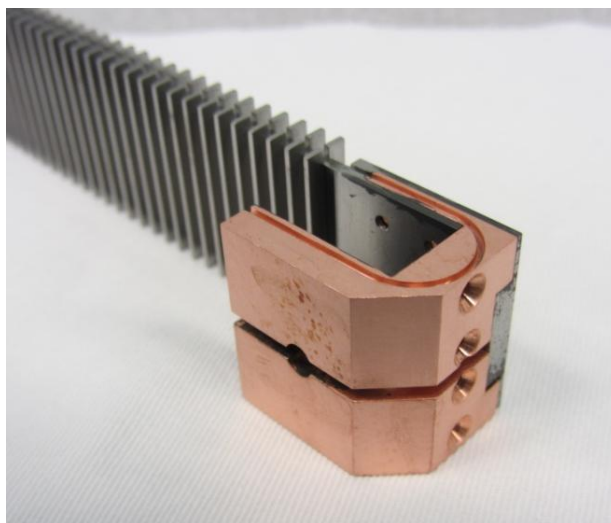
Figure 2.7 – Current terminals mounted on the sample holder.

Vertical Supports and Torque Arms

The vertical supports shown above in blue are designed to connect the sample

holder to the torque arms. These supports are designed to sandwich the ends of

the sample holder, clamping them in place. In modern designs, the vertical

supports are also used to fix both sample holders together, one on top of the other.

These supports are then joined to the torque arms using a pinned connection. Four

pins are used to make the connection. The four pins are oriented in a diamond

configuration shown in Figure 2.8.
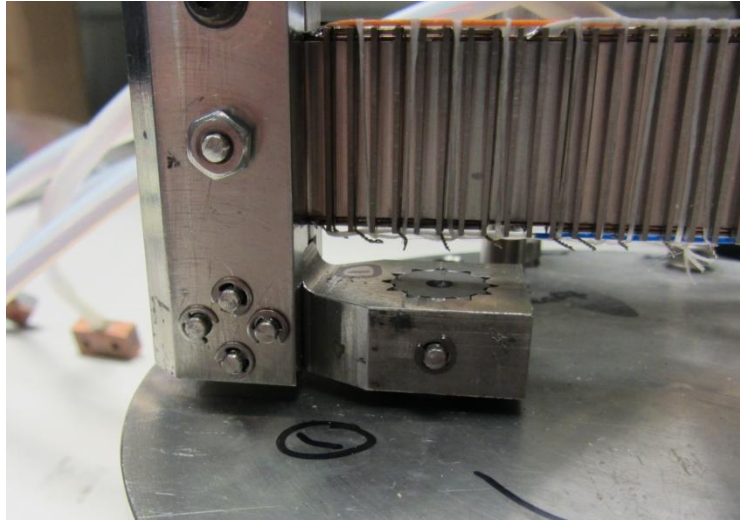
Figure 2.8 – Pinned attachment of the vertical support to the torque arm.

The torque arms refer to the two horizontal arms that are connected to the torque

shafts using a spline connection as seen in Figure 2.6. The torque arms provide

the axis of rotation for the sample holder. Because the axis of rotation is fixed, the

sample holder will not bend into a perfect circle at high bending. Therefore, the

length of the torque arm has been optimized to produce the least amount of

deviation or error in the deformed shape of the sample holder, over the entire

bending evolution. Both the torque arm and vertical support are manufactured

from 316 stainless steel (SS) to stay consistent with the gear train material. This

minimizes any thermal contraction effects that may occur during the cool down to

cryogenic temperatures.

3.0 Sample Holder History

The original sample holder was created by David Harris in 2005 in parallel with the development of the entire bending mechanism [1]. Based on undesirable results uncovered by Harris, Andrea Allegritti developed a new sample holder with major design alterations in 2006 [15]. With a need to characterize Nb_3Sn at higher stain levels, Phil Mallon modified Allegritti's sample holder in 2011 to achieve this [16]. Joe King took over Mallon's research and did further experiments using the same sample holders in 2012 [2].

3.1 First Generation

3.1.1 Sample Holder Design

The original sample holder created by Harris was designed to test three Nb_3Sn superconducting strands up to a maximum bending strain up to 0.9%. The original design was 50.8 mm (2 inches) tall and had a thickness of 1.588 mm (0.0625 inches). Based on his analytical design development Harris tested two sample holder lengths; 118.66 mm (4.672 inches) long for the maximum bending of 0.7% and 115.64 mm (4.553 inches) long for the maximum bending of 0.9%. Each length corresponds to a different torque arm radius which was optimized to reduce bending error for the maximum bending in the sample holder.

In this design, the Nb_3Sn strands were placed in three longitudinal grooves that were machined on one side of his sample holder. These grooves would allow the

strand to conform to the shape of the sample holder as it is bent and would use the thickness of the sample holder to resist the induced Lorentz load. The Nb_3Sn strands were only held in place by the current terminals at the ends. This ensured no shear coupling occurred within the grooves. This sample holder design with its three sample grooves can be seen below in Figure 3.1.
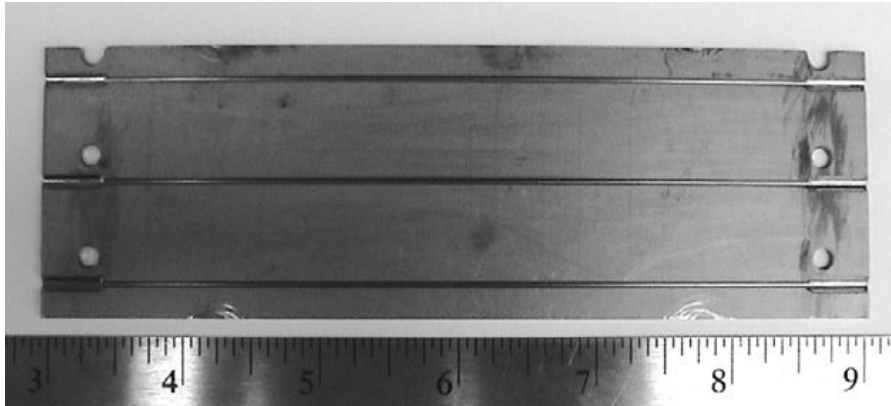
Figure 3.1 – First generation sample holder designed by Harris [1].

The sample grooves were machined to a depth of 0.91 mm (0.036 inches) placing the center of the strands 0.3 mm (0.012 inches) away from the geometric neutral axis of the beam. To eliminate this offset, additional smaller grooves were machined in the opposite side of the beam. These grooves can be seen in Figure 3.2 and were designed to shift the theoretical neutral axis of the beam to the location of the sample.
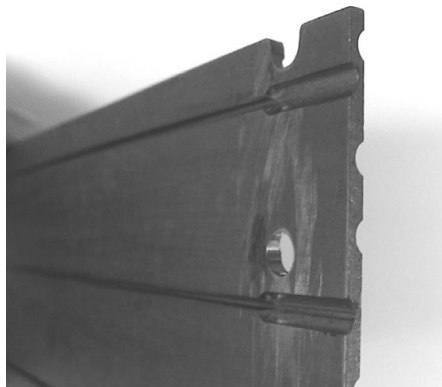
Figure 3.2 – Harris's sample holder showing neutral axis offset grooves [1].

3.1.2 Experimental Findings

One of the main findings of Harris's experiments was a low-current phenomenon. This low critical current behavior was worst at zero bending as indicated in the following figure. Figure 3.3 below depicts the experimental critical current results of an Intermagnetics General Corporation (IGC) sample tested by Harris. The critical current at zero bending is below 60 A where its manufacturing specifications indicate the critical current should be upwards of 200 A. This low-current behavior was also seen throughout testing. Another unexplained phenomenon that Harris noticed in the majority of his samples was a decrease in critical current around 0.2% bending strain which also is indicated below.
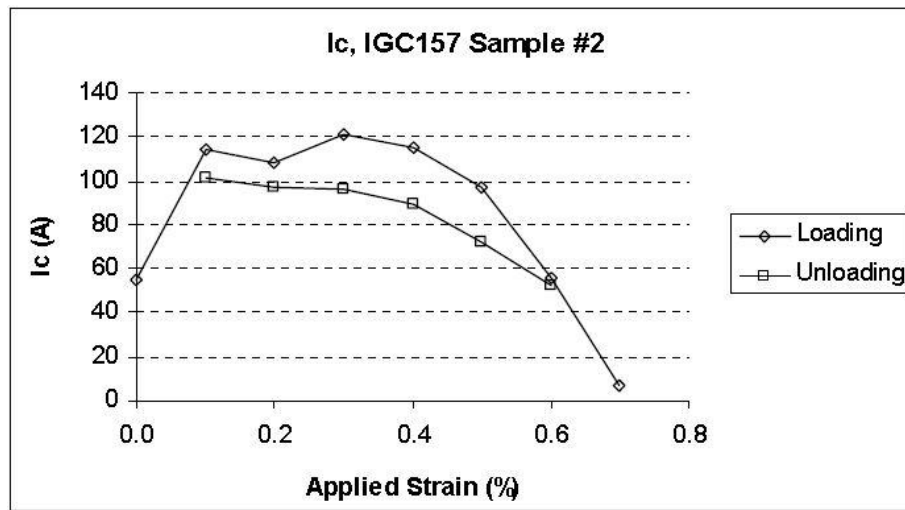
Figure 3.3 – Critical current results for one IGC sample test by Harris [1].

After experimentation the Nb_3Sn strands were found to be permanently elongated and bowed out of the sample holder grooves as shown in Figure 3.4. A post analysis indicated that the neutral axis offset slots did not work as expected. The offset of the strand from the true geometric middle of the sample holder superimposed an increased tensile strain on the strand. This increased tensile

28

strain likely caused the plastic elongation that occurred in the samples and is also

likely the cause of the decreased critical current seen in the experiments.
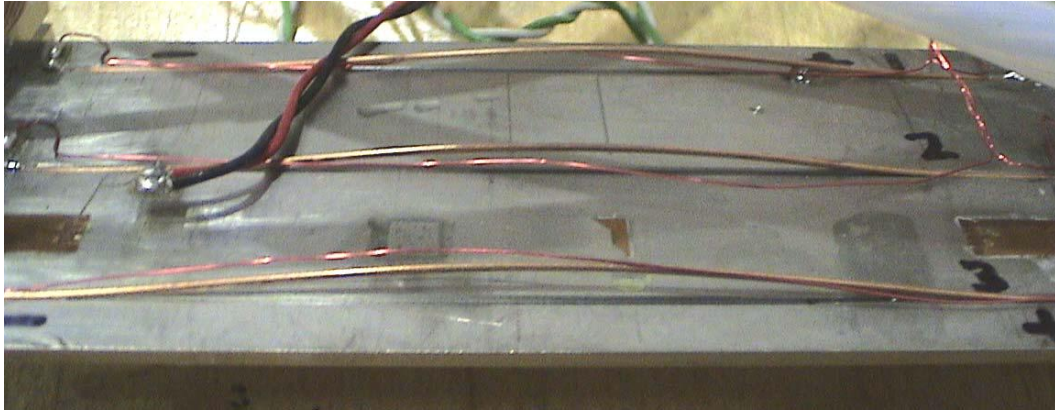
Figure 3.4 – Permanently elongated samples after experimentation [1].

3.2 Second Generation

3.2.1 Sample Holder Design

Based on outcome of the previous experiments, an improved sample holder was

designed to mitigate the problems that arose in the original design. This improved

sample holder was developed by Allegritti and has become the basis for all future

designs [15]. The sample holder was designed to place the Nb$_3$Sn strands in channels

machined along the top and bottom edges of the sample holder. This was done to

ensure the strands would always remain at the geometric neutral axis of the sample

holder during bending. This method eliminates the potential for an axial strain

increase caused by a geometric offset of the samples, as seen in the original design.

Because the samples are mounted in the top and bottom edge, only two samples

can be tested on any single sample holder. However, to accurately validate the

experimental critical current results, more than two test samples are needed. For

this reason, the second generation design replaces the one 50.8 mm (2 inch) tall

original sample holder carrying 3 strands with two new 26.06 mm (1.026 inch)

tall sample holders containing 2 strands each [15]. These new shorter sample

holders are depicted in the CAD rendering shown in Figure 3.5. This double beam

configuration allows for 4 samples to be tested at once, which is enough to fully

validate the critical current results for each sample.
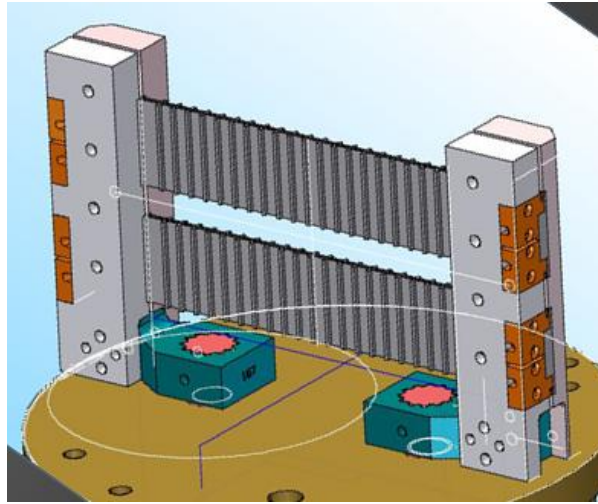
Figure 3.5 – Rendering of pure bending device with Allegritti's sample holder design [15].

Allegritti faced the same maximum bending limitation problem as Harris and had to

keep his overall sample holder thickness to 1.6764 mm (0.066 inches) to ensure the

sample holder did not yield before reaching the maximum bending strain of 0.7%.

However, this imposed a problem in his design, because the channel walls at the top

and bottom were now to thin too support the full Lorentz loads. Therefore, to support

the Lorentz load evenly spaced vertical support ribs were added along the length

of the sample holder as seen above in Figure 3.5. These support ribs provide the

extra support needed to resist the electromagnetic Lorentz load on the strands

while keeping the beam at an acceptable thickness.

The ribbed sample holder design can also be seen in the photo provided in Figure 3.6. This figure points out the evenly spaced nature of the vertical support ribs as well as the location of the superconducting strand; top and bottom edges.
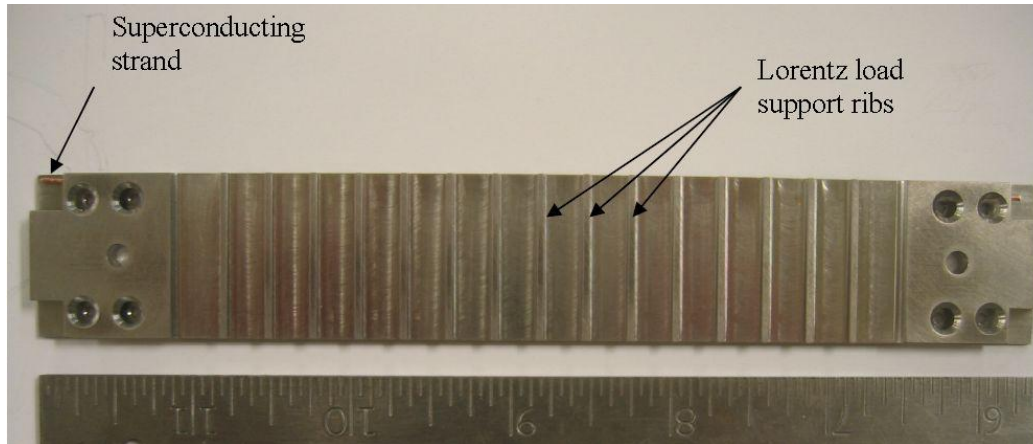
Figure 3.6 – Second generation sample holder designed by Allegritti [16].

As done previously, Allegritti also tested two sample holder lengths, 116.38 mm (4.582 inches) and 119.38 mm (4.700 inches). These lengths were again chosen based on analytical predictions for the optimal torque arm length. The tests were done to validate the analytical predictions and to determine the ideal length to be used in future experiements.

3.2.2 Experimental Findings

The critical current results from Allegritti's three days of experiments had good overall characteristics. The results of the first day showed significantly low critical current at zero bending. These initial degradations were continually improved on the following two days by more careful sample preparation. The general critical current trend found for all samples was a steady critical current up to 0.4% followed by steep decline upon further bending.

This critical current degradation is well represented in Figure 3.7, which shows the experimental results of an internal-tin type Nb_3Sn strand manufactured by Outokumpu. The critical current results were taken at 15 T and are plotted against the nominal bending rate which refers to the applied bending strain. In the figure, the results shown in blue (Eup) are from the top sample while the data shown in red (Elow) is from the bottom sample.
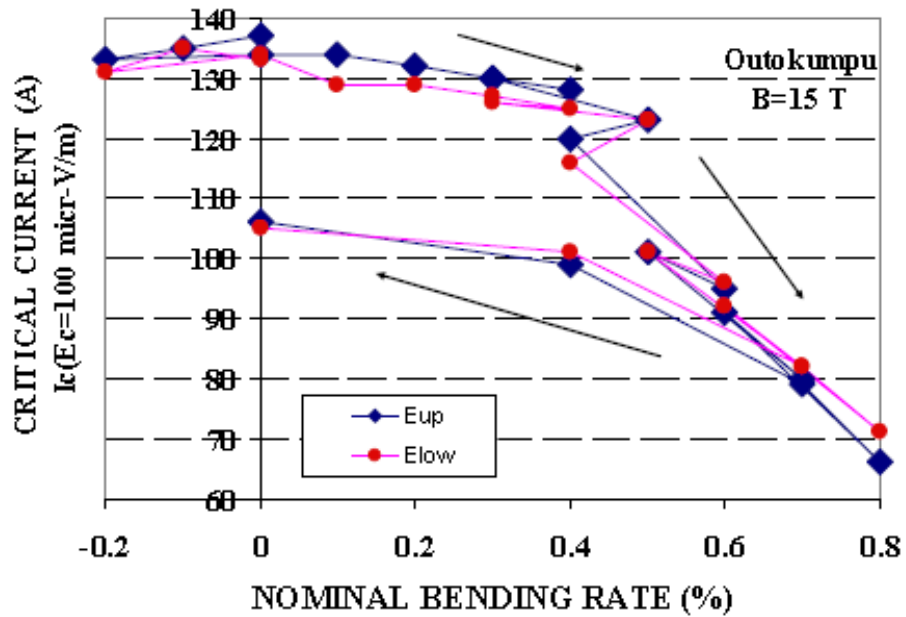
Figure 3.7 – Critical current results for Outokumpu samples tested by Allegritti [15].

Similar amounts of current reduction were experienced for all samples at the maximum bending state. These reductions were around 50% of the maximum critical current as shown in Figure 3.7. After bending was applied the strands tested from two different manufacturers, Outokompu and Oxford, saw permanent degradations in their critical current. The Outokompu samples had a 20% permanent reduction in critical current, while the Oxford samples saw around 35% permanent reduction.

3.3 Third Generation

3.3.1 Sample Holder Design

Following the relative success of Allegritti's experiments, there was a desire to continue the variable strain pure bending characterization tests over a wider range of bending. Mallon designed the next generation of sample holders to achieve this wider range of bending, up to a setting bending of 1.4% strain [16]. This level of bending was chosen based on the prior pure bending static experiments that were conducted [14].

To achieve this large strain without plastic deformation, Mallon also employed the vertical support rib design that was pioneered by Allegritti. Mallon's new sample holder incorporated three different sample holder designs each having a different overall thickness. CAD renderings of the sample holders are shown in Figure 3.8. The low bending sample holder is the thickest to help support the larger Lorentz load at low bending and conversely the high bending sample holder is the thinnest so it can achieve higher bending before yielding.
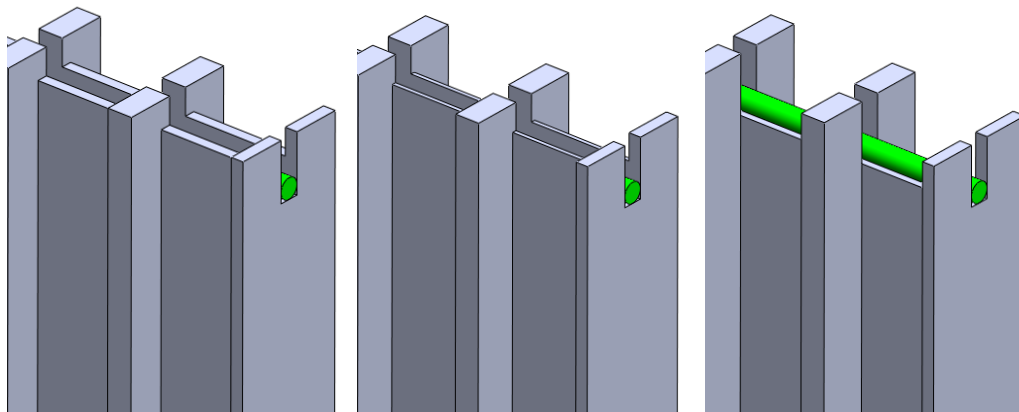
Figure 3.8 – The low (left), medium & high (right) bending sample holders design by Mallon.

The low bending sample holder was the same as Allegritti's and had a thickness of 1.6764 mm (0.066 inches). This sample holder was suitable for applying up to 0.7% bending strain. The medium bending sample holder was designed to cover up to a setting strain of 1.1% by using a slightly thinner sample holder that was 1.1564 mm (0.0455 inches) thick. The high bending sample holder was only 0.80 mm (0.0315 inches) thick and therefore could operate up to a setting strain of 1.4% bending without yielding [16].

For the high bending sample holder, the beam thickness is slightly less than the strand diameter. This means the high bending sample holder has an absence of channels walls, which is illustrated in Figure 3.8. The Nb_3Sn strands are therefore only supported intermittently by the vertical support ribs. This is the only major difference between the three designs besides their overall thicknesses.

The sample holders were designed to be the same height as the previous generation, 26.06 mm (1.026 inch) tall. This height was selected so that two sample holders could again be tested at the same time while using the same infrastructure. The sample holder length was chosen to be 116.38 mm (4.582 inches) long based on the findings from Allegritti's experiments.

3.3.2 Experimental Findings

Mallon's experiments were successful in covering a bending range up to a setting strain of 1.4% bending using the three new sample holders. All three beams performed adequately during the three days of experiments. Limited data was recorded for the medium bending sample holder because the input shaft galled to

34

the gear box in the middle of experiments. Some degradation in critical current was found after cycling the bending strain. These degradations were seen in all three sample holders. Two internal-tin Nb_3Sn samples were tested and each saw around a 60% loss in critical current at 1.3% setting strain.

The results for the Oxford samples tested by Mallon are shown in Figure 3.9. Samples 1 and 2 were tested on the low bending sample holder, 3 and 4 on the medium bending sample holder and 5 and 6 were test on the high bending sample holder. Results are only presented up to 1.3% strain due to loss voltage taps at maximum bending.
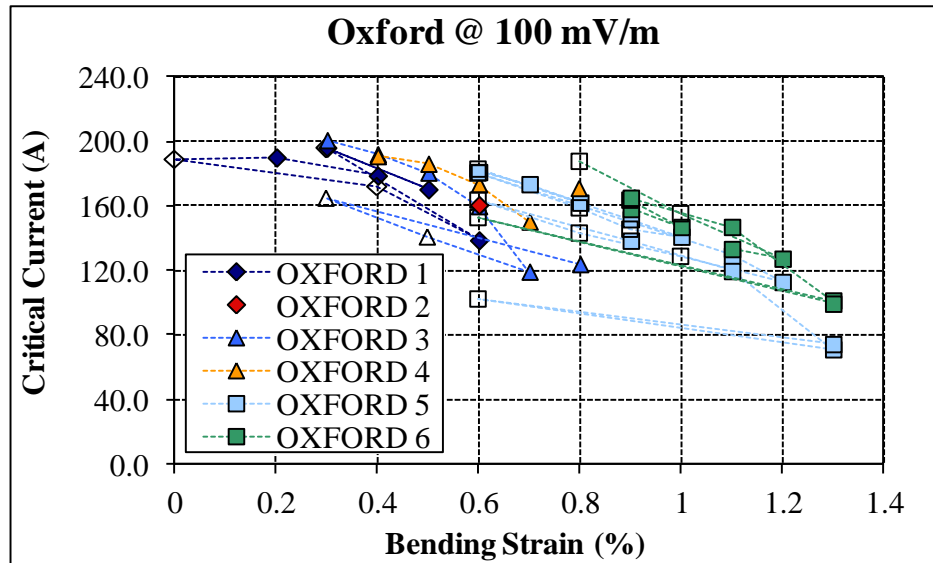
Figure 3.9 – Critical current results for Oxford samples tested by Mallon [16].

The results in Figure 3.9 show a gradual decrease in critical current as the amount of bending is increased. This is the characteristic trend that is expected for a superconducting sample under bending loads. However, the results do show a noticeable spread in critical current results at each percent bending. This spread could be caused by noisy experimental results, damage of the sample or a

35

discrepancy in critical current between the sample holders. The ideal trend would be indicated by overlapping critical current results showing one characteristic trend or line that degrades as the bending is increased.

King continued Mallon's research and tested two bronze-route Nb_3Sn strands using the same sample holder designs. He conducted successful experiments that gathered a large amount of critical current results for each sample holder. The critical current (Ic) results for the Hitachi samples from King's experiments are shown below in Figure 3.10 and are plotted against the applied bending strain. Again, samples 1 and 2 are from the low bending sample holder, 3 and 4 from the medium and 5 and 6 were from the high bending sample holder.
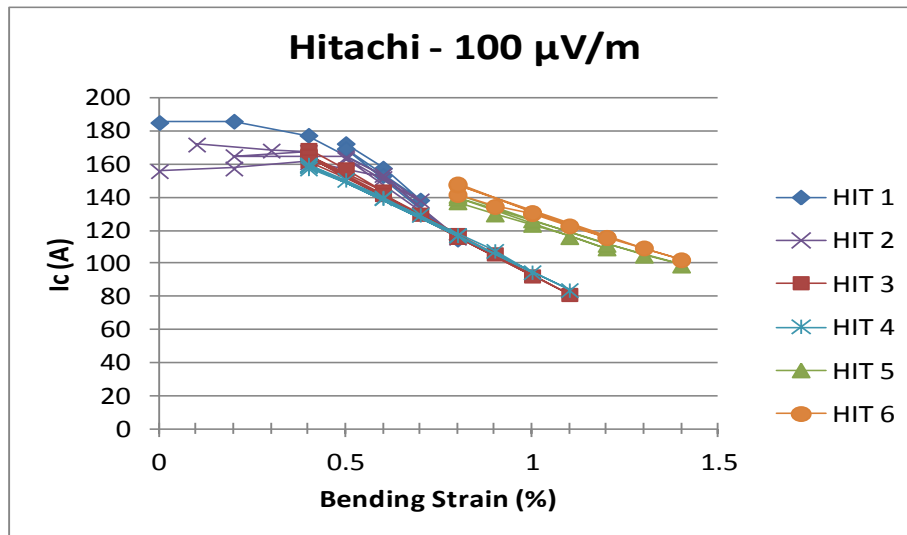
Figure 3.10 – Critical current results for Hitachi samples tested by King [2].

The results presented above clearly have less spread or variance in the critical current results compared to Mallon's data presented above. These very clear and ideal critical current results indicate unique characteristics of each sample holder that were unable to be seen in the previous results.

One of the unique characteristics that was identified from the results shown in Figure 3.10 was the lower critical current behavior seen in the medium and low bending sample holders. The current in these sample holders begins to degrade earlier and degrades more sharply than the current seen in the high bending sample holder. At 1.0% bending the critical current of the medium bending samples is roughly 95 A while the critical current of the high bending sample is 125 A. This is a clear discrepancy in results between the high bending and medium bending sample holders. This critical current discrepancy between the sample holders was identified for all of the samples tested by King and therefore has been the motivation for the work presented in this thesis [2].

4.0 Finite Element Analysis

The discrepancy in the critical current trends of the three sample holders has led to more detailed and in-depth finite element analysis (FEA) to try and identify the possible causes. Basic FEA modeling of the sample holder under bending was done previously. More accurate FEA modeling was undertaken in this research to appropriately model the true interaction between the superconducting strand and the sample holder, which has not been done prior. Also, for the first time the FEA models incorporated the influence of the electromagnetic loading on the samples.

The objective of these more true-to-life simulations was to identify an accurate strain distribution within the superconducting strand and then to compare that strain with the experimental critical current data. This comparison will help shed light on why the low and medium bending sample holders experienced lower critical currents.

4.1 Prior Sample Holder Modeling

As mentioned above, prior finite element modeling of the sample holder alone was done by Allegritti, Mallon and King. Allegritti was the first to initiate the FEA modeling and began with straightforward simulations of the sample holder under bending [15]. Mallon built upon these simulations by conducting a top-down modeling approach to better characterize the behavior of the sample holder under bending [16]. King briefly continued this modeling and focus on simulating the medium and high bending sample holders up to their maximum bending [2].

Mallon began by initially modeling the sample holder as a purely flat beam. Having a simplified model devoid of all features was useful in identifying the true behavior of a thin beam under bending. This modeling was able to successfully identify two important characteristics of the sample holder under bending; neutral axis shift and transverse warping of the beam [16].

Under bending, one side of the sample holder is in tension while the other is in compression and in between there is a location that experiences zero strain. This location is referred to as the neutral axis and theoretically should lie in the center of the geometry for a beam under bending. The FEA results gathered by Mallon indicated that the actual zero strain location occurred shifted towards the inside (concave side) of the sample holder. This neutral axis shift was explained by the second finding; warping of the sample holder.

The FEA modeling revealed that the beam bowed transversely along the height of the sample holder. A pictorial representation of this bowing is shown in the FEA image presented in Figure 4.1. In the image, the vertical height of the beam is rotated horizontally to more clearly indicate the warping effect. This warping can be best described by a Poisson's ratio effect [17]. The outer half of the sample holder is under longitudinal tension contracting its cross section. The inner half of the sample holder is under longitudinal compression expanding its cross section. As one side contracts the other side expands causing the whole cross section to distort producing the warping that is shown in Figure 4.1. This warping effect was validated through experimentation and was found to be worse for wider beams.

39
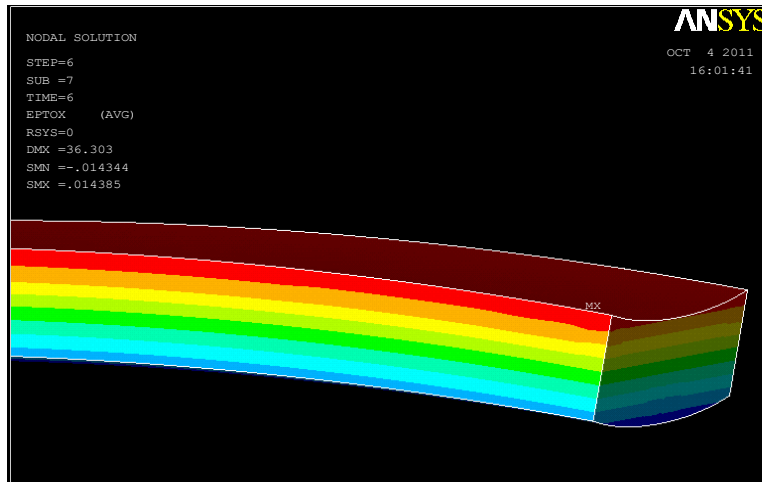
Figure 4.1 – Contour plot showing warping of a flat beam under bending [16].

Although this simplified modeling is good for understanding the mechanisms behind the bending behavior, it is also beneficial to analyze the actual design to identify its bending characteristics. Mallon's initial findings for a model with vertical support ribs and a channel are that the ribs decreased this warping effect by almost 60% for the low bending sample holder [16].

King continued the FEA work that Mallon started, focusing on analyzing the full sample holder models with the support ribs and channels up to higher bending. The main finding from these simulations was a unique non-uniform strain contour in the channel walls of the sample holder. It appears that the support ribs have inadvertently created localized high axial strain regions [2]. An example of this high strain region is shown in Figure 4.2 which is a contour plot of the longitudinal strain in the sample holder channel wall. It seems the support ribs locally provide enhanced flexural stiffness which exaggerates the deformation experienced in channel walls in between ribs. This strain behavior was identified in both the low and medium bending sample holders.

40
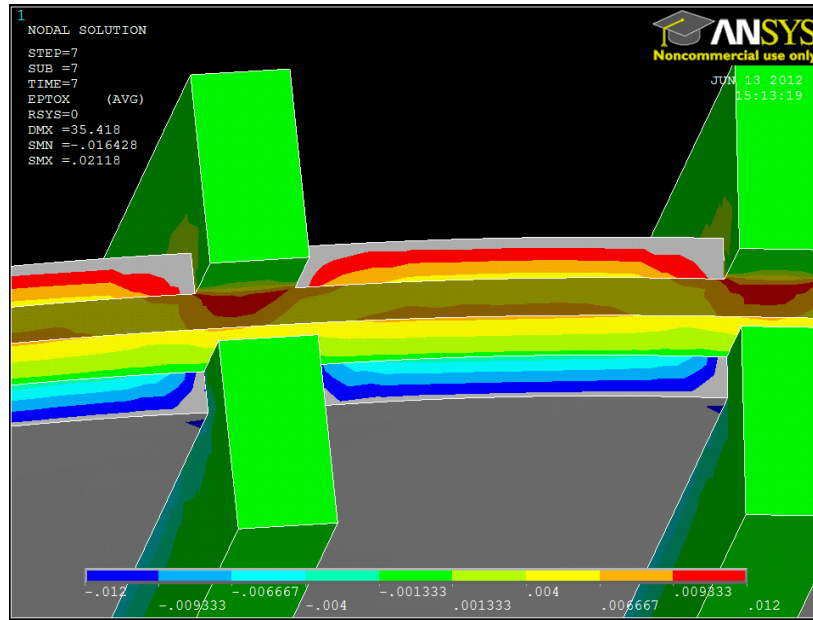
Figure 4.2 – Longitudinal strain plot showing localized strain gradients at the ribs [2].

The simulations conducted by King were the first to show the deformed shape of the sample holders at their maximum bending states. The ideal shape for a state of true pure bending is a perfect circle. The FEA results for the deformed shape of the high bending sample holder are presented in Figure 4.3 for three bending states. In the figure, the green curves are for a bending strain of 0.6%, the grey curves for 1.1% strain and the light blue curves for the maximum applied bending of 1.4% strain. The perfect circle at each of these bending states is also plotted and is denoted by the dashed lines. The solid colored lines indicate the results from the FEA model.

Figure 4.3 shows that the deformed shape of the sample holder closely matches the ideal shape at 0.6% bending. At 1.1% and 1.4% setting strain, the sample holders show a noticeable deviation from the ideal perfect circle. This behavior was predicted by Harris during his analytical development of the device and could

not be removed; only minimized to reduce the deviation. This deviation from a true perfect circle may influence the strain state of the sample. The effect that the deformed shape has on the actual strain in the samples, specifically at high bending strain, will be discussed in more detail in the following sections.
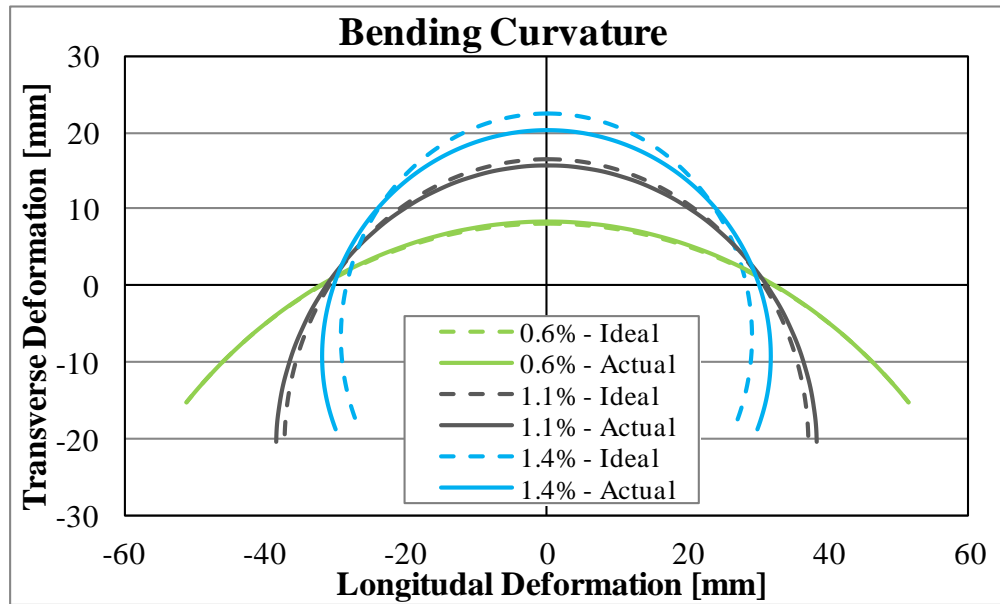
Figure 4.3 – Deformed shape of sample showing deviation from a perfect circle.

4.2 Constraints, Loads & Contact Pairs

All simulations run using ANSYS® incorporated the same basic simulation settings, boundary conditions, contact pair definitions and loads. The model geometry was imported into ANSYS® from SolidWorks®. A half model was created using a symmetry plane to reduce the simulation complexity by half. The Nb_3Sn strands were constrained to their channels using appropriate contact pair definitions. The rotation of the torque arms was applied using a pilot node contact pair definition and the Lorentz load was applied as a pressure load on a line effect element located in the middle of the Nb_3Sn strands.

4.2.1 Boundary Conditions

The three main boundary conditions or constraints that were applied to the FEA

model include a symmetry condition, in-plane motion and a fixed axis of rotation.

Symmetry

To run the simulations using only a half model, a symmetry boundary condition

was used. This condition was applied to the ends of the sample holder and strands.

This constraint is depicted as the orange symbols in the following two FEA

images presented in Figure 4.4. The symbols are orange triangles which indicate

the translation degrees of freedom that are constrained for symmetry.
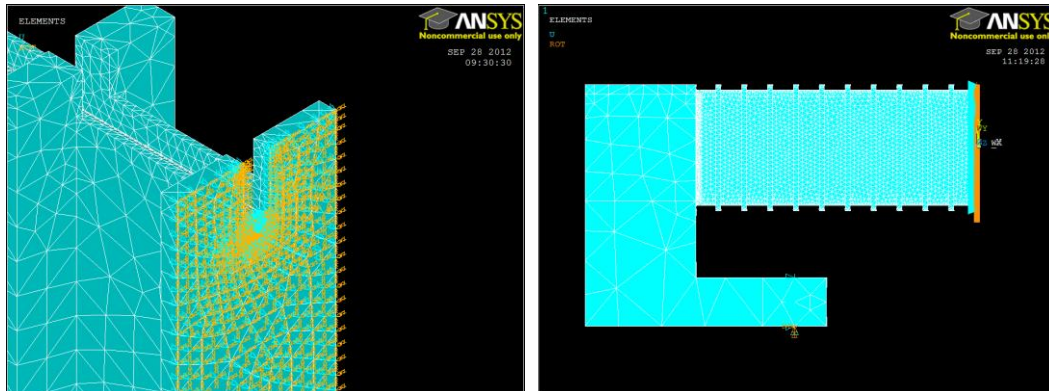
Figure 4.4 – Symmetry boundary condition applied end of sample holder and strand.

In-Plane Motion

The torque arms that apply the bending motion to the sample holder rotate in-

plane about the torque shafts. To achieve this in-plane motion, the entire bottom

surface of the torque arm is prescribed to have zero displacement in the vertical

(Y) direction. This boundary condition is represented in Figure 4.5 by the small

white triangles located at the base of the torque arm. These triangles point in the

direction of the prescribed fixed displacement.
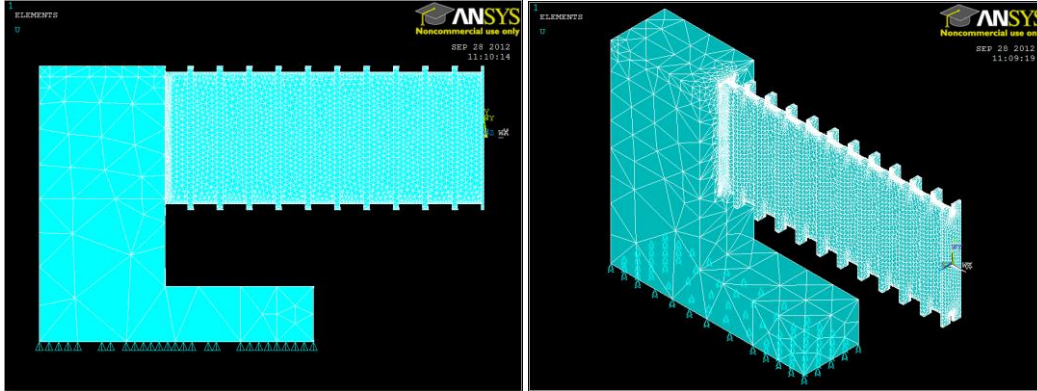
Figure 4.5 – In-plane boundary condition applied to base of torque arm.

Fixed Axis of Rotation

As mentioned above the torque arms rotate about the torque shafts. To emulate

this rotational behavior of the torque arms, their axis of rotation was fixed. This

was achieved by applying a zero displacement condition in all 3 translational

degrees of freedom (X, Y & Z), allowing it to only rotate about this axis. This

constraint is again represented by the small white triangles in the following figure.
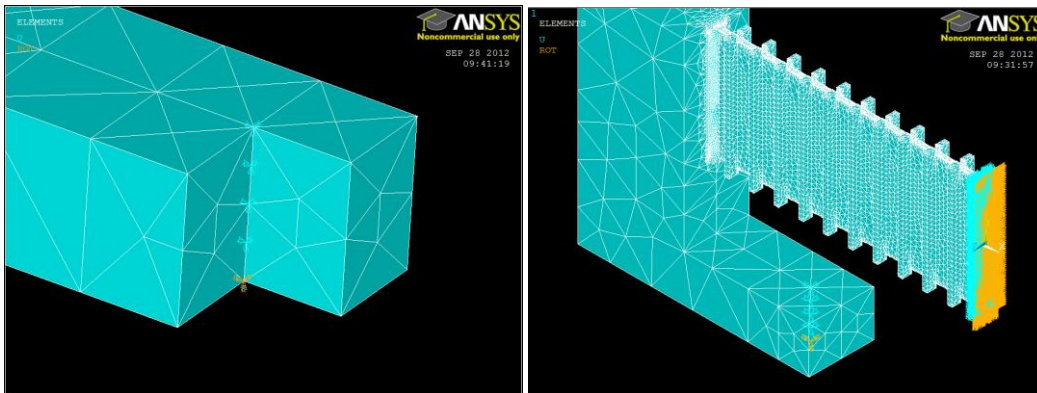
Figure 4.6 – Fixed constraint applied to the axis of rotation.

4.2.2   Loading

Two main types of loads were applied to the model; pilot node rotation and

uniform distributed load. The pilot node rotation was applied to bend the sample

holder and the uniform distributed load was used to simulate the electromagnetic loading on the sample.

Pilot Node Rotation

To apply the rotation of the torque arms in the model, a pilot node contact pair was chosen which allows rotation to be directly prescribed to the model. The pilot node contact pair was created by first meshing the node at the base of the axis of rotation using target elements and then meshing the bottom surface of the torque arm with contact elements. The contact settings are defined so that, if a rotation is applied to the pilot node the contact elements are also rotated the same amount. This contact pair relationship is clearly shown in Figure 4.7. The contact nodes are shown in pink and are constrained to the target node (pilot node) which is indicated in the figures.
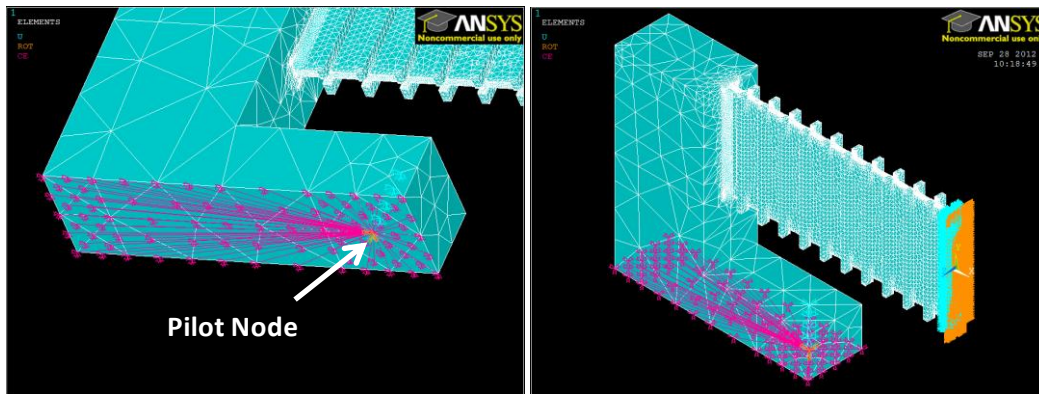
Figure 4.7 – Pilot node contact pair applied on the base of the torque arm.

Lorentz Load

The interaction between the current in the superconducting strand and the background magnetic field creates an electromagnetic Lorentz force on the sample. For our application the Lorentz load always acts in a plane that goes

45

through the center of the strand and remains perpendicular to the height of the sample holder. The load will be directed either radially inward towards the center of curvature of the sample holder or radially outward depending on the current direction within the strand. The Lorentz load was simulated by applying a uniform distributed load to a line-effect element located in the exact center of the superconducting strand. The load is prescribed as a pressure so that the load vectors will always remain perpendicular to the deformed shape of the strand as it bends. An inward facing Lorentz load is depicted by red arrows in Figure 4.8.
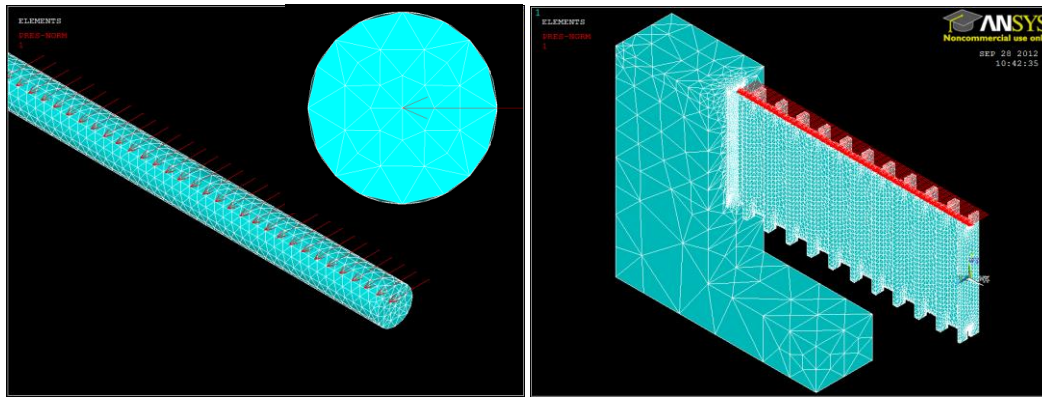
Figure 4.8 – Uniform distributed load applied to a line at the center of strand.

4.2.3   Contact Pairs

The primary importance of this modeling was to identify the superconducting strand's strain distribution under bending conditions with an applied electromagnetic loading. To accurately achieve this, the interaction of the strand with the sample holder channel walls was of utmost importance. This interaction was modeled using a surface-to-surface contact pair definition.

A contact pair is defined as having a target surface and a contact surface which share a set of defined characteristics or settings. The contact surface is defined as

46

the surface that makes contact with the target surface. Which surface is the target and which is the contact is based on the specific application. For the contact pairs in our FEA model, the channel walls and/or support ribs were meshed as the target surfaces while the strand was meshed as the contact surfaces. Both these contact surfaces are generated on top of the existing solid geometry and are solely used to model the interaction between the solid geometries. Individual contact pairs were defined for the inner and outer walls as well as the channel base. The contact pair characteristics are described in more detail below.

Contact Pair Settings

The characteristics of the contact behavior were defined in ANSYS® using keyopts; which essentially are different settings that can be chosen for the contact pair relationship. The contact pair was selected to have translational degrees of freedom (UX, UY & UZ) only. An augmented Lagrangian approach was used as the contact algorithm and the contact point detection was specified on the Gaussian integration points.

Automatic contact surface adjustment (ICONT) was specified, allowing ANSYS® to move all initially open contact points onto the target surface. This adjustment is best depicted in the schematic presented in Figure 4.9. This setting was specified to help improve the convergence of the contact pairs during the simulation.

Initial geometric penetration was excluded which moves the contact detection locations to the target surface as illustrated in Figure 4.10. This setting was also selected to help improve convergence of the simulation.
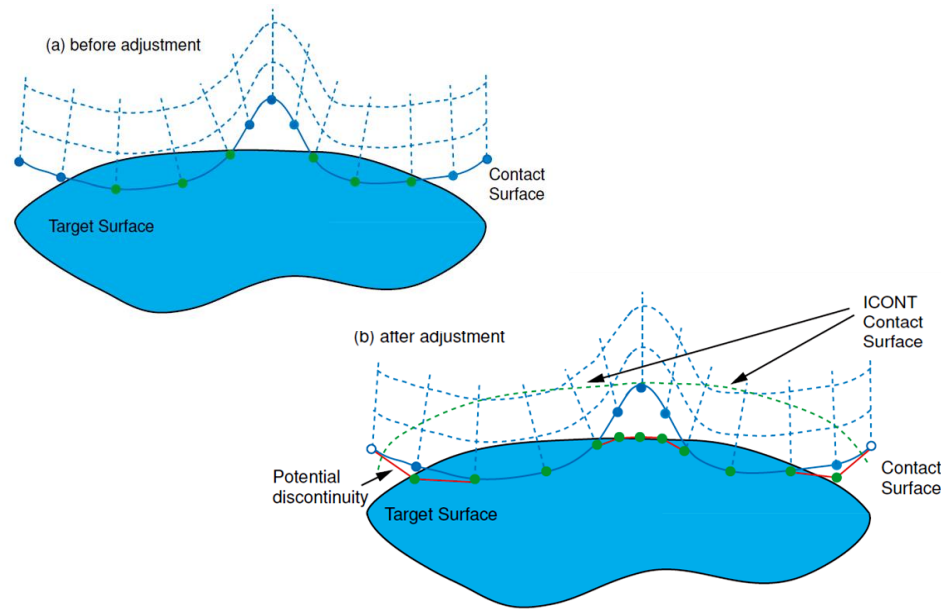
Figure 4.9 – Pictorial representation of auto ICONT setting [18].
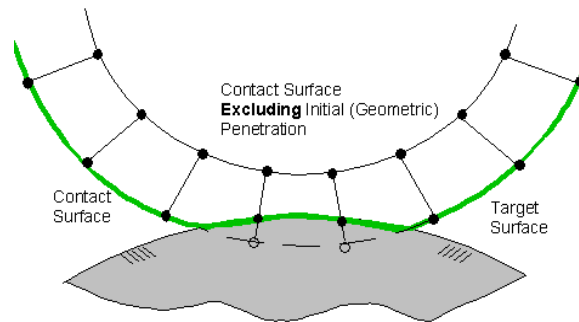
Figure 4.10 – Pictorial representation of initial penetration setting [18].

Contact Surface Definitions

The outer and inner channel wall contact pairs are prescribed as standard contacts with frictional sliding. The channel base contact pair is the same with the addition of a no-separation condition, keeping the strand within the channel. The three contact pairs are shown below in Figure 4.11. The target surfaces were meshed on the channel walls. In the figure these target surfaces are indicated as the purple surfaces. The contact surfaces were meshed on the strand and are indicated by the red and blue surfaces.
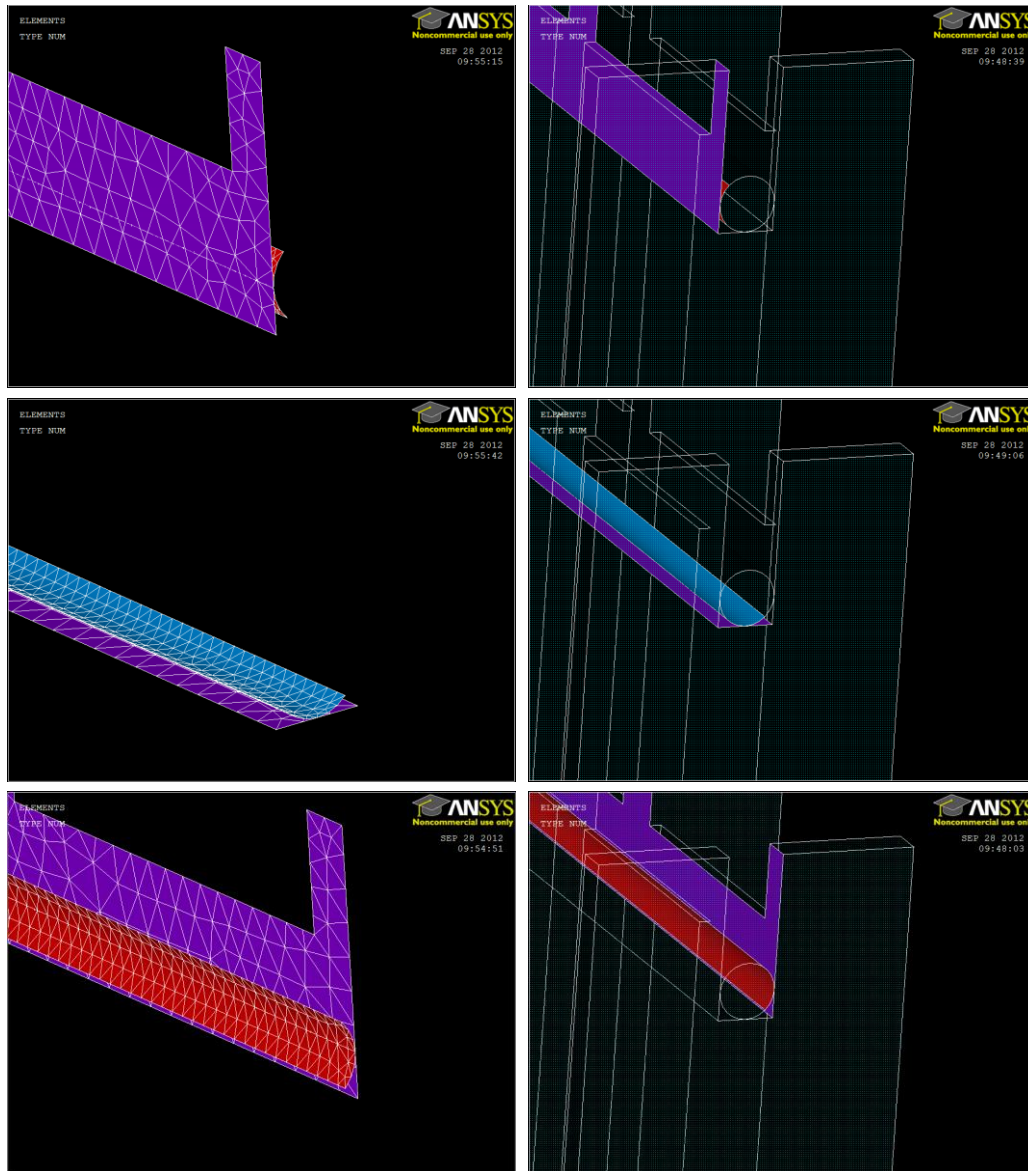
Figure 4.11 – Contact and target surfaces applied to the strand and channel walls.

The end of the superconducting sample was modeling using a bonded surface-to-surface contact. The end of the strand was meshed as the contact surface and the sample holder was meshed as the target surface. The FEA simplification of the sample's end condition is shown in the right image in Figure 4.12. The image shows that the sample holder is modeled as a flat wall and the end of the strand is mated up to that surface. This was a simplification that was done for modeling;

49

however, the real end condition of the sample is much different and is shown in the left image of Figure 4.12. In the real sample holder the sample continues past the end of the sample holder into a channel in the current terminator as seen below. The sample gets soldered in this channel which constrains it.
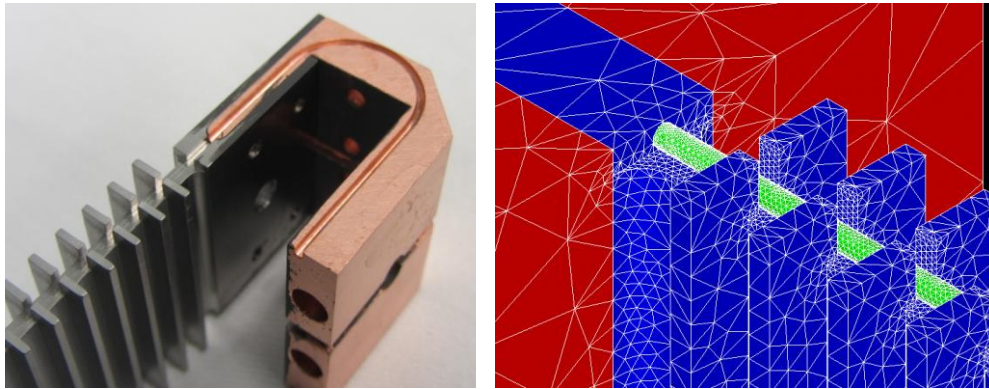
Figure 4.12 – FEA end condition for sample (right) and actual end condition (left).

Our chosen FEA end condition for the sample was selected as an acceptable simplification for the model. However, it is unclear if this style constraint will have any effects on the strain distribution within the sample near this end. The constraint could potentially cause a stress build up near these ends. That being said, it also may have no effect because the end condition does constrain the motion of the sample in a similar fashion to real life.

4.3 Elements, Mesh and Model Settings

4.3.1 Element Types

Solid Model Elements

The type of element used to mesh the solid model was the SOLID95 3D structural solid element. The element shape chosen was a tetrahedral configuration which

can tolerate irregular shapes without much loss of accuracy. It is also well suited to model curved boundaries. The element is defined by 20 nodes having three degrees of freedom per node: translations in the X, Y, and Z directions. It has plasticity, creep, stress stiffening, large deflection and strain capabilities which make it a good choice for the current application. Brick elements were appropriate for the torque arms, but tetrahedrals were used for consistency.

Contact Elements

The contact pairs were defined using TARGE170 and CONTA174 element types in ANSYS®. The TARGE170 element is a general 3-D target surface element that can be either rigid or deformable. This element takes on the shape of the underlying solid model elements; therefore, a tetrahedral solid element will map into a triangular surface elements. The CONTA174 element is an 8 node surface-to-surface contact element. It is used to represent sliding contact between rigid target surfaces and deformable contact surfaces. The element is applicable to 3-D structural analyses and is overlaid onto the solid geometry creating a contact surface. These elements also take on the same geometric characteristics as the solid elements they are covering and will be meshed as triangular elements. Contact is detected when the contact element's surface penetrates one of the elements on a specified target surface.

4.3.2 Mesh Density

Finite element analysis is an approximation technique that produces results based on the calculations of many simplified discrete elements. For this reason, the

mesh density of the model is of critical importance. If the mesh is extremely coarse, the calculations will produce poor approximations and erroneous results. However, if the mesh density is adequate the calculations will produce accurate approximations which are potentially indistinguishable from the exact values.

To ensure appropriate results from our FEA simulations, a detailed mesh analysis was conducted. The mesh analysis was done to determine an appropriate mesh density to produce accurate results, while maintaining an acceptable computation time. A course mesh will compute quickly but produce poor results. A refined mesh will take longer to run but will produce more accurate results. A very fine mesh will take an extremely long time to compute and will produce results with minimal improved accuracy. Therefore, the goal of the analysis is to determine the degree of mesh refinement that initially begins to produce consistent accurate results within a reasonable simulation time.

First, a course mesh was tried for the sample holder. Then the mesh was continually refined until an appropriate mesh density was determined. Following this, the mesh only inside the channel of the sample holder was refined further to locally increase the accuracy of the results in region. A similar process was done for the Nb_3Sn strands. The mesh began coarse and then was continually refined until an adequate mesh density was determined.

The overall mesh density for the entire model consists of 4 main levels. The levels of mesh refinement can be seen in Figure 4.13. Each model was meshed with roughly 125,000 elements and 250,000 nodes.
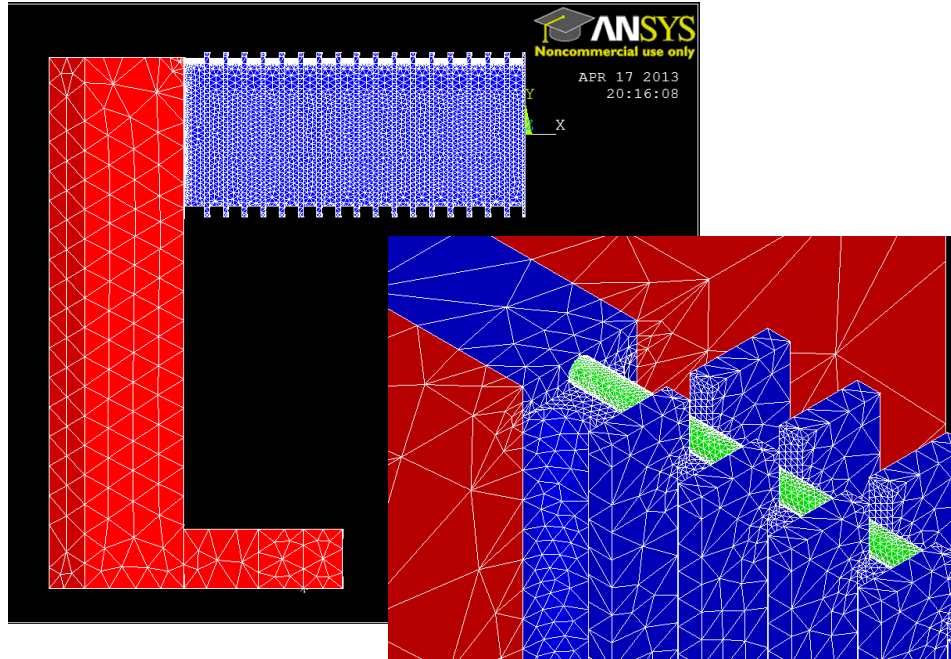
Figure 4.13 – FEA images indicating the differences in mesh refinement.

The torque arms are meshed very course because they are only used to apply the bending and the strain within them is not important. The sample holder has a more refined mesh because its deformation behavior is critical to the modeling. The channel walls of the sample holder are refined further to ensure an accurate interaction takes place between the channel and the strand. And lastly, the samples have the finest mesh density ensuring the most accurate strain results.

4.3.3 Material Definitions

The sample holder was modeled using the multi-linear stress-strain curve for Ti-6Al-4V titanium alloy shown in Figure 4.14 [19]. For simplicity, the Nb_3Sn strands were modeled as a uniform material with the bi-linear material model for annealed copper that is shown in the following figure [20]. In Figure 4.14, the stress is denoted by SIG and the strain is denoted by EPS. The stress is defined in

units of mega-pascals while the strain is unit less parameter. The vertical supports
and torque arms were modeled as an elastic 316 stainless steel. All material
properties were taken from literature and are defined for a temperature of 4.2 K.
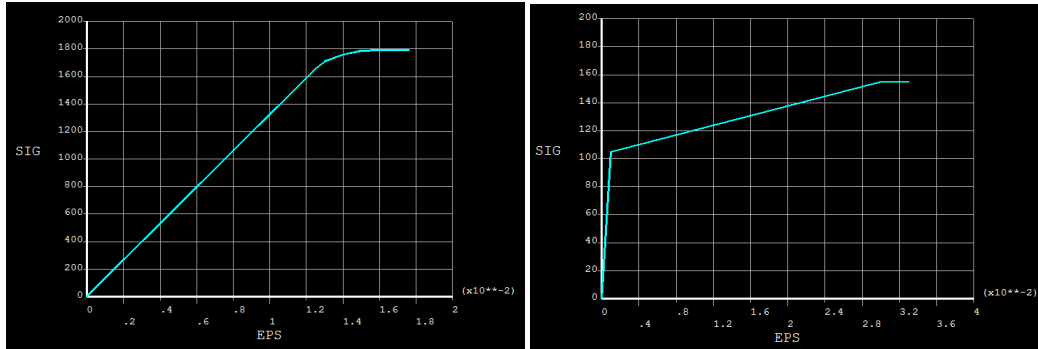
Figure 4.14 – Ti-6Al-4V (left) and Cu (right) material models used in ANSYS® [19][20].

4.3.4 Model Settings

The model was run as a static non-linear analysis including large deformation and
strain effects. This was done because these FEA models have many forms of
nonlinearity including, sliding, large rotation and non-linear materials. The
frictional sliding contact behavior introduces nonlinearities into the analysis. The
large deformation and rotation can cause the structure to respond nonlinearly. The
nonlinear stress–strain material relationships are also a direct cause of nonlinear
structural behavior. For the non-linear analysis, the Newton-Raphson integration
technique was specified.

A friction coefficient of 0.2 was defined for all material interactions. This low
value was chosen because the components were given a light coating of graphite
to reduce friction in the experiments. However, its exact effectiveness in a
cryogenic environment is unknown and therefore a realistic value was estimated.

54

Automatic time stepping was used so that ANSYS® could make the appropriate adjustments to increase the convergence rate. The rotation and Lorentz loads were incremented gradually incremented to facilitate initial convergence. Stress and strain results were recorded for each load step.

4.4 Strand-in-Channel Models

Care has been taken to appropriately model the interaction between the strand and the channel walls of the sample holder. Creating the most realistic contact behavior is crucial to the accuracy of the strain distribution within the strands. If inappropriate contact is defined the strain results in the strand may be erroneous and misleading. The specific settings and contact characteristics used were described in detail in the preceding section.

The three ribbed sample holders designed by Mallon were each analyzed separately. All results presented below are for models excluding the Lorentz load. Regardless of their operational range, all sample holders were first compared at a bending strain of 0.6% on the outer edge of the strand. Strain results for the medium and high bending beam at their max bending state are also presented.

4.4.1 Low Bending Sample Holder

To determine the full strain distribution throughout the strand, data was collected for a number of locations through the width of the strand. The superconducting strands tested have a copper matrix surrounding the Nb_3Sn filaments. The filaments start at a diameter that is roughly 70% of the overall strand diameter.

Therefore, it is of utmost importance to know the strain distribution within the strand so that the strain at the filament level can be determined.

ANSYS[®] path plot operations were used to collect longitudinal strain data along the length of the sample at 9 different radial locations through its diameter as shown Figure 4.15. Path location A corresponds to the inner edge of the strand where it contacts the channel wall, path location E is the exact middle of the strand and path location I is the outer edge of the strand where it contacts the other channel wall. Each location is separated by approximately 0.1 mm along the diameter. As mentioned previously in section 1.6, the Nb_3Sn strands have a copper stabilizing layer on the outside of the wire; consequently, the actual Nb_3Sn filaments are located between paths B and H. This indicates that the strain the filaments experience will be slightly less than the strain on the surface, E and I.
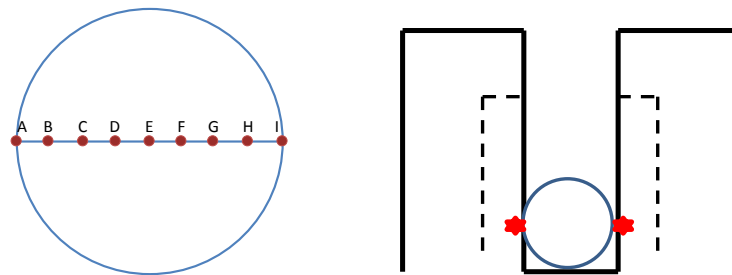
Figure 4.15 – Data collection locations in the strand (left) and sample holder (right).

The axial strain results from these locations are plotted in Figure 4.16 for the low bending model at 0.6% bending strain. The strain is plotted versus the position along the length of the sample; -58 mm refers to the end of the sample near the torque arm and 0 mm refers to the middle of the sample. The curve at the top of the plot (light green) represents the outer surface (path I) and the curve at the very bottom (blue) represents the inner surface of the sample (path A).

56
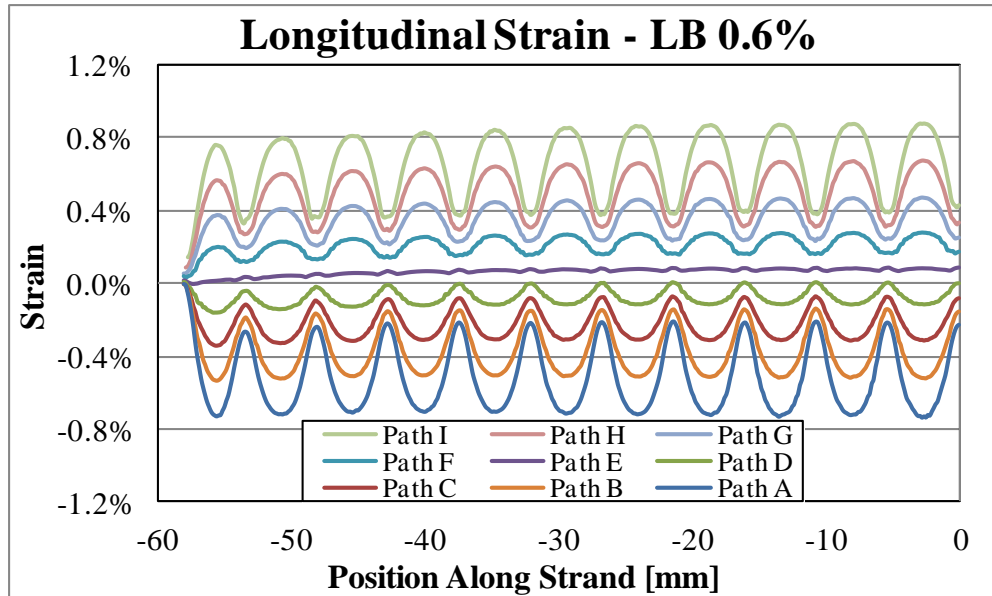
Figure 4.16 – Longitudinal strain within strand for low bending sample holder

The main finding from these strain results is a very large strain fluctuation on the surface of the samples. On top of this, these strain fluctuations penetrate all the way through the strand and are noticeable at the center. These fluctuations on the surface of the sample have a magnitude of greater than 0.4%. This is an adverse effect which will definitely influence the amount of current the sample can carry.

In addition to the fluctuations, the results also show a neutral axis shift. The strain at the center of the strand, Path E, is experiencing 0.075% strain in the center of the sample (0 mm). Ideally the center of the strand would have zero strain if it was in a state of true pure bending. This shift is caused by the warping effect that was described previously. Because the width of the low bending sample holder is greatest, the warping effect is more pronounced and consequently is seen even with the presences of the support ribs.

These axial strain results can be visualized in the contour plot seen in Figure 4.17

57

which shows the ANSYS® results for the inside surface of the top sample. In this figure, blue indicates negative or compressive strain and red is the positive or tensile strain. For pure bending the sample should have a uniform compressive strain on the inner surface of the strand. Instead, the contour plot indicates clear regions of high compressive strain on the inner surface. The high strain regions indicate the strain fluctuations that were seen in the above plot. The outer surface has similar periodic locations of high tensile strain. These high strain regions will degrade the Nb$_3$Sn filaments locally reducing the sample's performance.
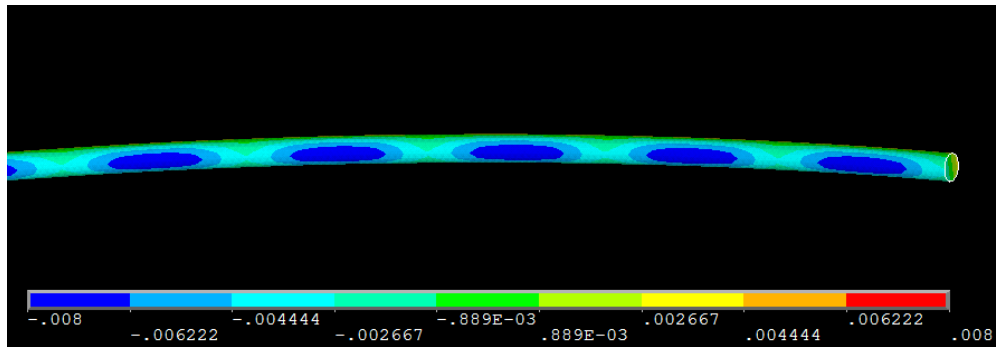
Figure 4.17 – Contour plot of axial strain for low bending sample holder.

From the above results it is obvious that the support ribs and the channel wall are affecting the strain distribution along the strand. To identify what is directly causing these strain fluctuations; data in the outer and inner channel walls was collected. This strain data was collected along the length of the sample holder at the contact height of the strand as shown in Figure 4.15. The axial strain results for the channel walls are plotted in Figure 4.18 and are indicated by the red curves. The strain results from the outer surface of the sample also plotted and are indicated by blue curves.

From the plot it is clear that the strain distributions in the channel and in the

58

strand are very different from each other. The strain felt in the strand is a much
smoother and repeatable wave like fluctuation while the strain in the channel is a
more irregular fluctuation having very large strain concentrations. These large
spikes in the channel wall strain are at the location of each rib and are most likely
caused by the ribs creating a local stiffing effect in the channel walls. This
indicates that the strain in the channel is not directly transmitted into the strand.
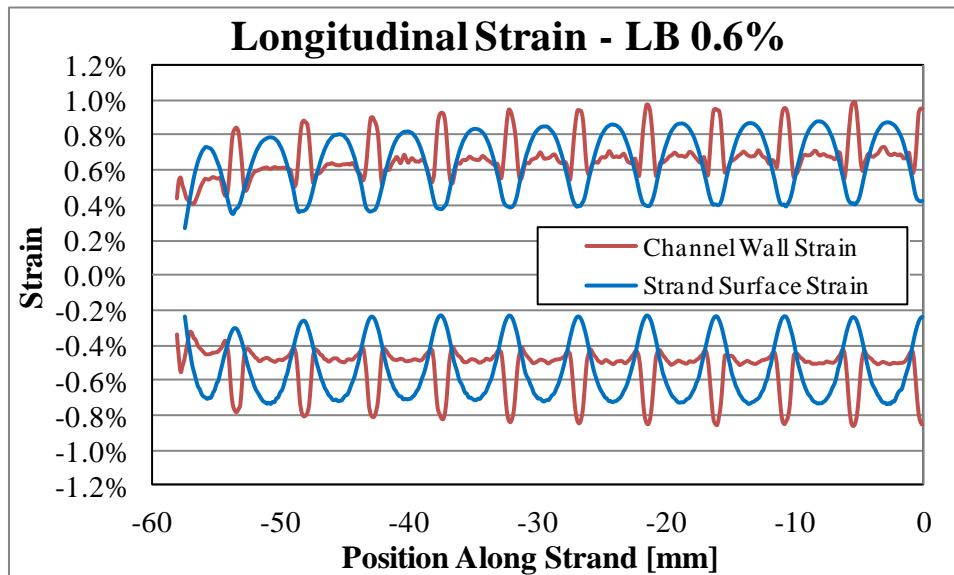
Figure 4.18 – Longitudinal strain for low bending sample holder.

The strain results presented above proved to be inconclusive in determining an
exact cause for the strain fluctuations in the strand. For this reason, further
investigation was done to determine the exact mechanisms behind the strain
distributions presented in Figure 4.18. From this investigation, it was identified
that the channel walls have a tendency to bow or distort during bending. The
bowing is most severe for the inner channel walls and is clearly shown in Figure
4.19. The deformation in these figures is not exaggerated. The sample was
removed from the images for clarity.
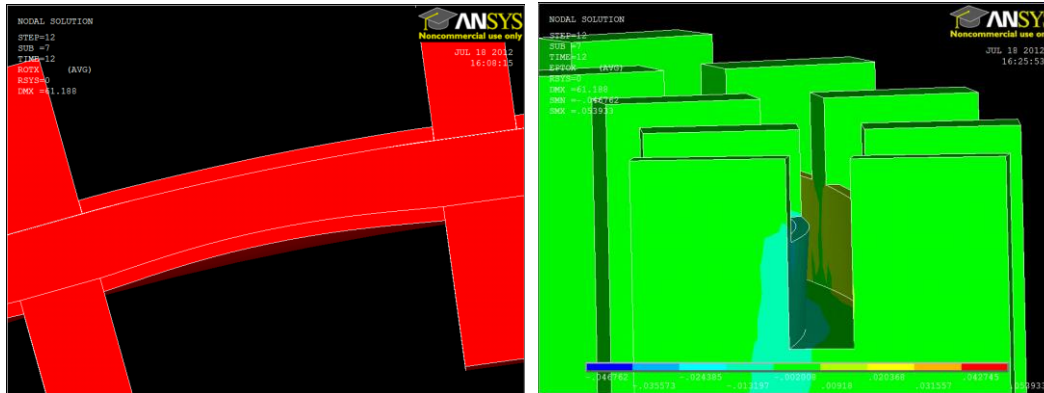
Figure 4.19 – Simulation images showing bowing of the inner channel walls.

The large bowing of the inner channel wall is likely caused by a buckling type effect. The buckling is created from the thin channel wall on the inner surface being put under axial compression causing it to deform or buckle. This bowing deformation in the channel walls can be used to explain the strain profile found in Figure 4.18. This effect is best represented using the slightly exaggerated schematic shown below in Figure 4.20.
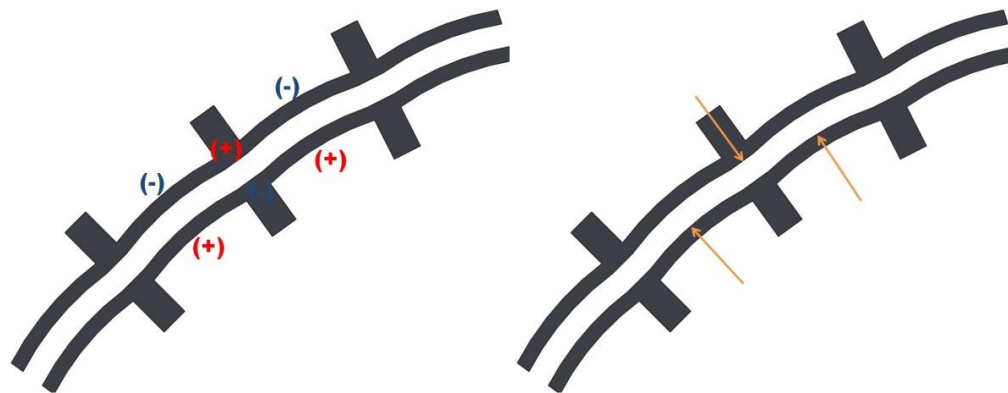
Figure 4.20 – Exaggerated schematic of channel wall bowing effect.

The schematic on the left indicates the "localized" compression (blue minus sign) and tension (red addition sign) regions on the channel wall. On the compressive side of the sample holder, the locations of the ribs are in concave regions where they experience localized compression. Oppositely, the channel walls are bowed

60

in a convex shape and are being put in localized tension. These "localized" effects will either increase or decrease the overall compressive strain state of the inner channel wall. Therefore, these effects create the strain fluctuations and spikes seen in Figure 4.18. A similar but opposite trend is experienced on the outer, tensile surface.

The schematic on the right in Figure 4.20 can be used to explain how this channel wall bowing phenomenon influences the strain that is transmitted into the strand. The arrows in the schematic point to the regions that apply contact pressure on the sample. As the inner channel walls bow, they protrude into the channel and apply contact pressure on the inner surface of the strand. This radially outward contact pressure from the inner walls, forces the strand outward. As the strand tries to move outward it is constrained by the support ribs which apply contact pressure on the outer surface of the strand.

These pressure point locations correlate to regions of "localized" high compressive strain on the surfaces of the sample. On the inner strand surface, this "localized" high compression creates regions of maximum compressive strain. On the outer strand surface, this "localized" high compression creates regions of minimum tensile strain. This min and max strain can be clearly indicated on the large strain fluctuations presented in Figure 4.16 and Figure 4.18.

Because the contact pressure points are at different longitudinal locations on the inner and outer surface, the sample is forced to slightly bend back and forth in a serpentine pattern. On the opposite surface from these pressure points, the strand

is experiencing "localized" tension due to the bending. This "localized" tension leads to the maximum strain on the outer tensile surface of the sample and the minimum strain on the inner compressive surface of the sample. Again, these min and max strains can be clearly identified on the strain fluctuations shown prior.

In addition to determining the strain state of the strand, these FEA simulations allowed us to identify the deformed shape of the sample holder. For the strand to be in a state of pure bending the deformed shape must match that of a perfect circle. From the design of the device it is known that the deformed shape of the sample holder should diverge from a perfect circle at higher bending. This is due to physical and mechanical limitations of the device and cannot be overcome [1].

To identify the accuracy of the low bending sample holders, its deformation at three bending levels is plotted alongside a perfect circle in Figure 4.21. The deformation data presented in the plot was taken from the center of sample. The results were extrapolated to show the deformed shape of the entire sample holder. In the figure above, the dashed lines represent the shape of a perfect circle for the corresponding bending level.

From these curves plotted in Figure 4.21, it is apparent that the low bending sample holder deforms quite closely to a perfect circle over its entire bending range. As mentioned above, this behavior was expected for low bending strains. There is a slight difference in the sample holder deformation but not significant enough to cause error. Therefore, it is obvious that the low bending sample holders deform in a state of pure bending over their entire bending range.
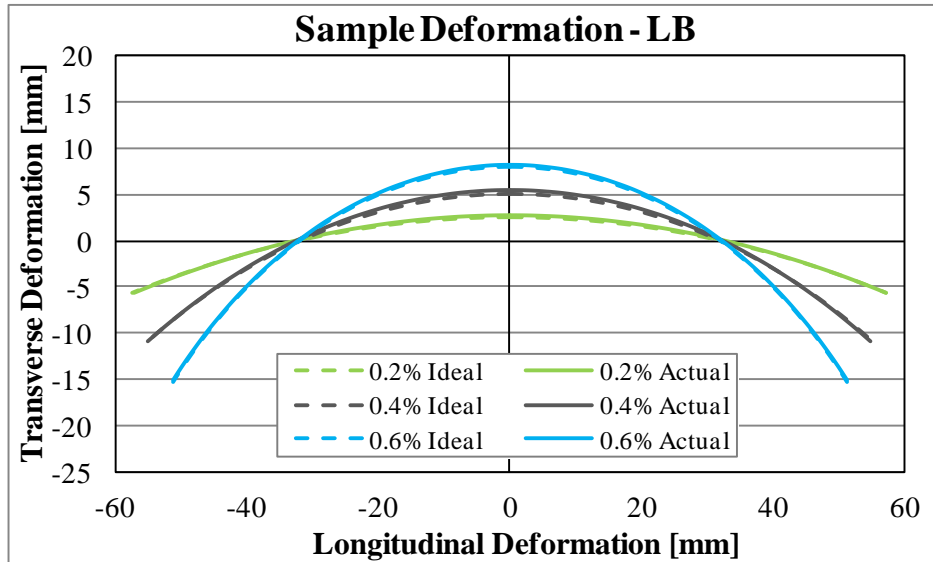
Figure 4.21 – Deformed shape of strand in the low bending sample holder.

4.4.2 Medium Bending Sample Holder

As done for the low bending sample holder, the longitudinal strain data was collected along the length of the sample at the same 9 radial positions through the diameter. These strain results are plotted at a bending strain of 0.6% in Figure 4.22. The middle of the sample is at 0 mm and the end is at -58 mm.
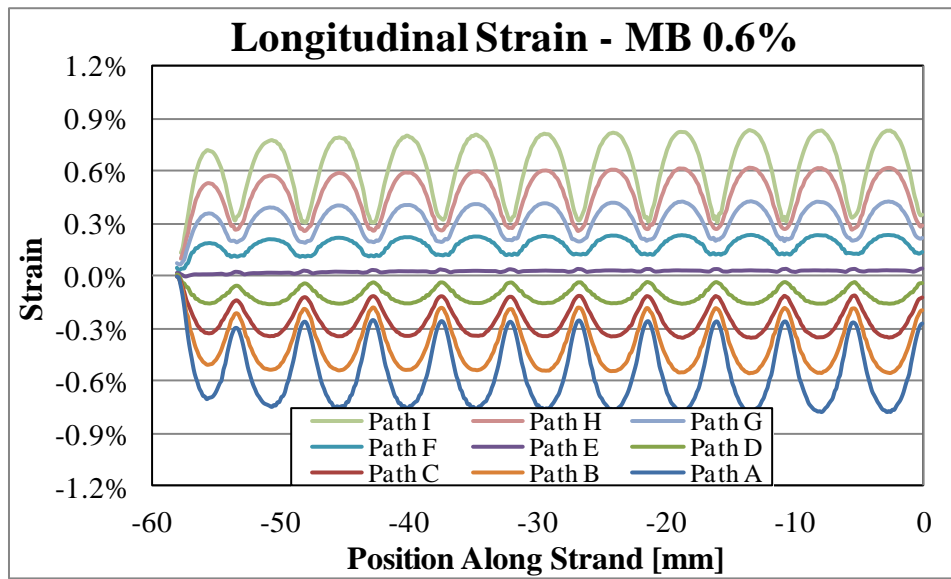
Figure 4.22 – Longitudinal strain in strand for the medium bending sample holder.

63

The medium bending sample holder results presented above are very similar to those found for the low bending sample holder. The magnitude of the strain fluctuations on the surface of the strand are again greater than 0.4% and consequently penetrate through the cross-section of the sample. Because the strain results for medium bending sample holder are so close to those found for the low bending sample holder at the same amount of applied bending, the contour plots are indistinguishable. For that reason the contour plot is not shown in this section, but can be seen previously in Figure 4.17.

This similarity in strain results was an expected characteristic since both sample holders were at the same amount of applied bending and have very similar designs. They have the same overall size, the same number of support ribs and they both have channel walls. The difference in the sample holders is their width. The width of the medium bending sample holder is narrower and therefore has thinner channel walls. The narrower nature of the sample holder was shown to reduce the severity of warping that was experienced. This reduction in warping is indicated by the noticeably smaller shift in the neutral axis as seen in Figure 4.22. The strain at the center of the strand is now less than 0.035% in comparison to the previous 0.75% for the low bending sample holder.

The medium bending sample holder was also simulated up to a rotation of 89.49° which is equivalent to an applied setting value of 1.1% bending strain on the outer surface of the sample. The strain results over the entire bending range are given in Figure 4.23. The data was taken from the outer, inner and middle of the sample as

indicated by Paths A, E and I in Figure 4.15. The general trend of large periodic

strain fluctuations appears to be evident at all bending states. In addition to this,

the magnitude of the fluctuations appears to grow as bending is increased. As the

bending is increased the degree of channel wall bowing grows which produces

larger strain fluctuations on the strand, as seen below. The results presented above

also indicate a new strain characteristic that is experienced at higher amounts of

bending. This characteristic is an increase in the level of axial strain near the

torque arms (around -58 mm). The larger the bending strain the greater this

increase becomes.
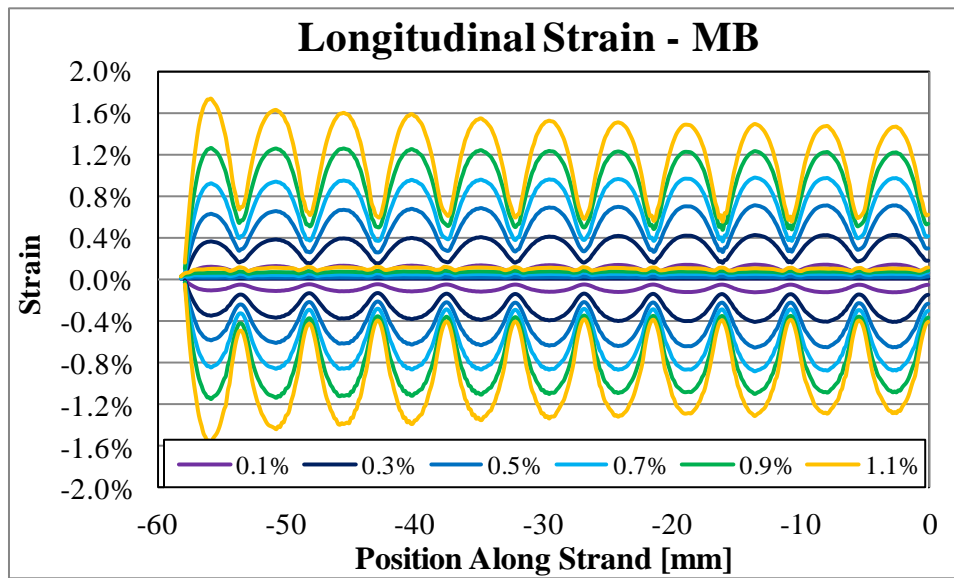
Figure 4.23 – Longitudinal strain for medium bending sample holder up to 1.1%.

This phenomenon is likely be caused by a deviation in the deformed shape of the

sample holder compared to a perfect circle. Figure 4.24 below is a plot of the

deformed shape of medium bending sample holder compared to that of a perfect

circle. The deformation results were taken at 0.2% strain increments up to the

maximum strain of 1.1%.

65
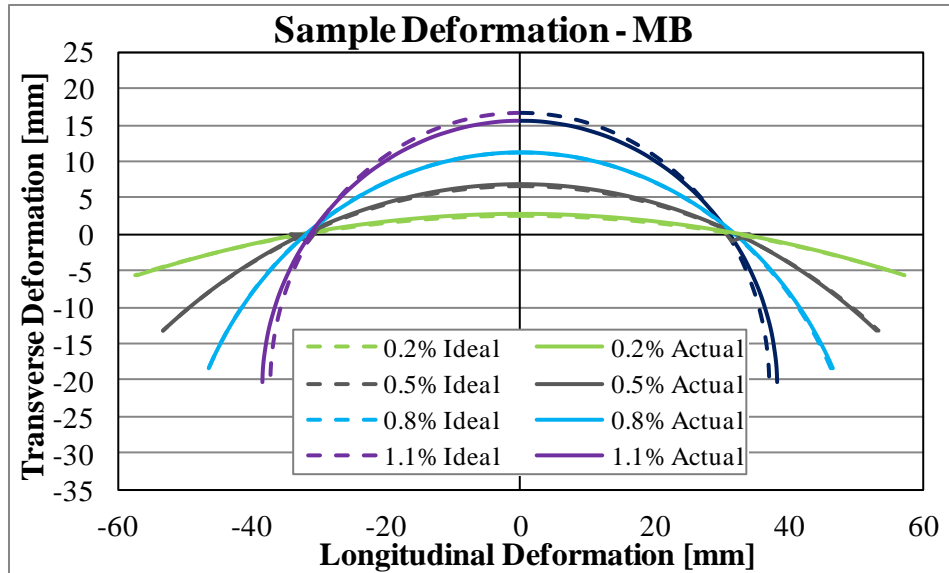
Figure 4.24 – Deformed shape of strand in the medium bending sample holder.

From the results shown above, a distinguishable difference between the shape of the sample holder and that of the perfect circle is seen for 1.1% bending strain. In the middle of the strand the sample holder experiences slightly less bending and consequently has slightly more bending at the ends. This increased bending near the torque arms correlates well to the increased strain experienced at the ends of the sample holder shown in Figure 4.23 above.

4.4.3 High Bending Sample Holder

At an applied bending of 0.6%, the longitudinal strain data for the high bending sample holder was recorded. The data was again collected at the radial locations through the strand's diameter. These results are presented in Figure 4.25 and indicated a much different strain distribution than was found for the low and medium bending sample holders. This difference was expected for the high bending sample holder, because it has no channel walls.
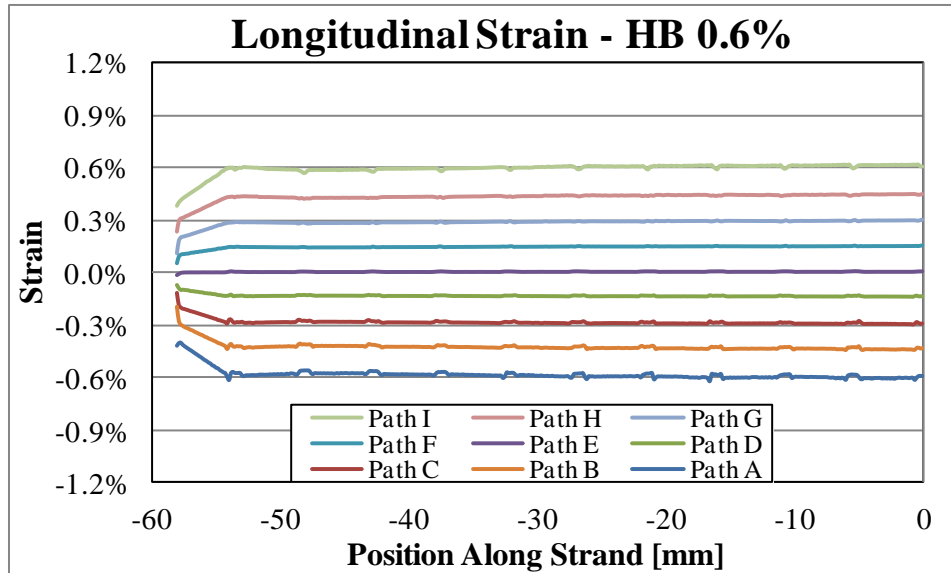
Figure 4.25 – Longitudinal strain in strand for high bending sample holder.

The overall strain behavior shown in the above results is a uniform strain along the sample, which is the ideal characteristic for pure bending. No major strain fluctuations were experienced because the high bending sample holders has no channel walls which were found to create the large strain fluctuations in the medium and low bending sample holders. The strain distribution does have small bumps at the location of each rib which indicates that the support ribs are affecting the strain in the sample but not in the same manner as found for the low and medium bending cases.

A contour plot of the axial strain along the strand is shown in Figure 4.26. This simulation image helps clearly show the uniformity of the longitudinal strain on the inner surface of the strand. This uniformity is indicated by the constant blue compressive strain that runs the entire length of the sample. This result is a much better characteristic than the oval regions of high compressive strain that were seen in Figure 4.17 for the low and medium bending cases.

67
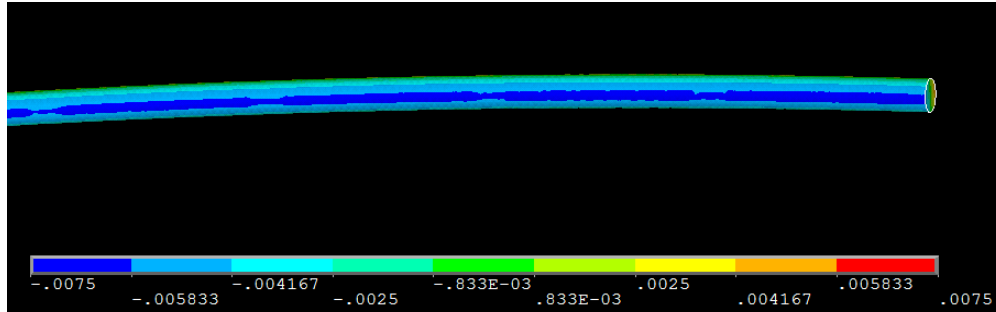
Figure 4.26 – Contour plot of longitudinal strain in strand for high bending sample holder

The high bending model was also simulated up to a setting strain of 1.4% bending which correlates to a rotation of 113.85°. This is the maximum bending strain that the high bending sample holder is designed to take before yielding. As done for the medium bending sample holder, the strain results are shown every 0.2% bending strain. These results are shown in Figure 4.27 which plots the strain on the outer surface, inner surface and center of the strand. The small bumps on the strain distribution are again noticed and appear to increase with the amount of applied bending. Other than the bumps the strain profiles are very uniform with exception to the increase in strain at the end of the sample (-58 mm).
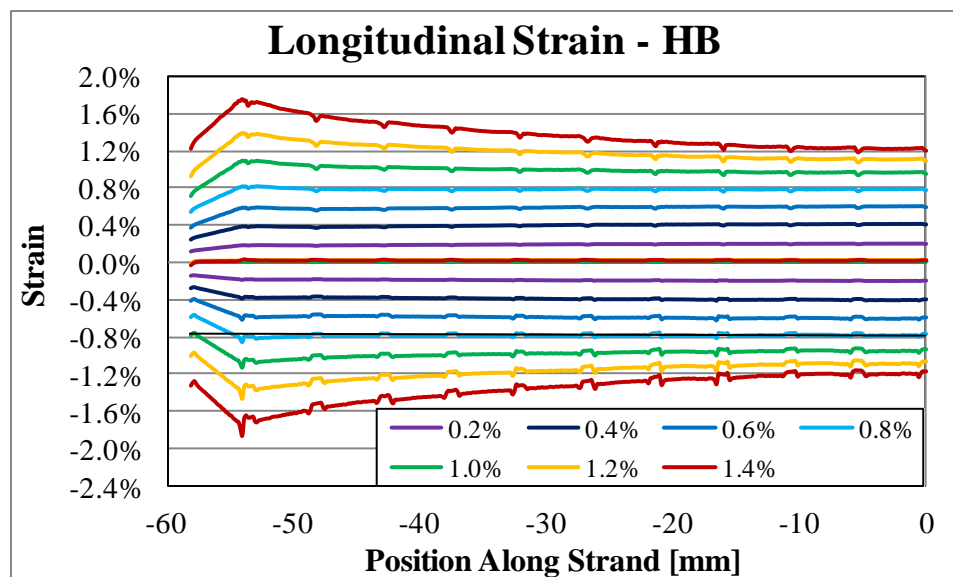
Figure 4.27 – Longitudinal strain of the high bending sample holder up to 1.4%.

The increase in strain near at the torque arms as was first identified in the medium bending sample holder results presented above. The uniformity of the strain makes it clear that the increase does not significantly begin until above 1.0% strain. At 1.4 % strain this increase is most severe. In addition to this, the strain at the middle of the sample holder (0 mm) for an applied setting strain of 1.4% is only 1.25%. Therefore, the strain in the sample at 1.4% experiences slightly lower strain in the middle of the sample and significantly more strain at the very ends.

As found in the medium bending case, the cause of this strain behavior can be directly attributed to the deviation of the deformed shape from that of a perfect circle. The deformed shape of the sample in the high bending case is present below in Figure 4.28. From the results in the figure it is clear the deviation from a perfect circle only becomes severe at bending strains greater than 1.0%.
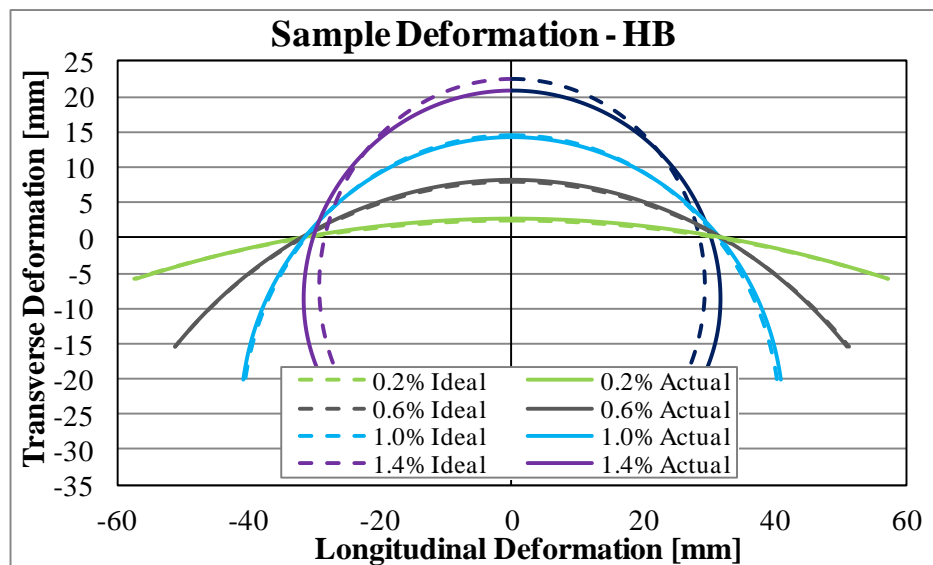
Figure 4.28 – Deformed shape of strand in the high bending sample holder.

At 1.4% strain the strand experiences less bending curvature in the middle of the sample and a higher bending curvature at the two ends. The lower curvature in the

69

middle is the reason for the slightly lower strain in that region. The higher

curvature at the ends causes the high strain behavior at the ends of the sample.

At 1.0% bending there is a small deviation. The strain results presented in Figure

4.27 indicated a fairly uniform strain level over the entire length of the sample.

This indicates that the small deviation in the deformed shape shown below does

not have a significant influence on the strain state of the sample.

4.4.4 Strand-in-Channel Summary

The interaction between the surface of the superconducting strand and the channel

walls of the sample holder has been successfully modeled. These models have

been used to determine the actual strain that is transmitted into the strand via the

three sample holders. The results for the strain state and deformed shape of the

sample under no Lorentz load have been provided in the previous three sections.

The two main findings from these results that will be discussed next are the large

strain fluctuations discovered in both the low and medium bending sample holder

and the non-perfect circle deformation of the sample holder that was experienced

at high bending.

The results for the longitudinal strain within the superconducting sample were

presented above for each sample holder at an applied bending of 0.6%. These

results clearly show that the low and medium bending sample holders are

experiencing very large strain fluctuations that penetrate all the way into the

strand and are even seen at the center of the strand. These large strain fluctuations

were determined to be caused by a bowing of the channel wall. As the walls bow

into the strand, they applied compressive contact pressure creating these regions of high and low strain along the sample. Because these fluctuations penetrate through the sample they may adversely influence the performance of the strand.

In contrast to this, the results for the high bending sample holder showed a very uniform strain distribution with only minor bumps in the strain at each rib. This is a very ideal strain behavior; however, the addition of the Lorentz load is expected to negatively influence this. The last thing that should be noted from the strain results is the difference in the neutral axis shift between the three sample holders. The low bending sample holder is the thickest of the three and experienced the largest neutral axis shift towards the tensile side. On the other side, the high bending sample holder is the thinnest and consequently experienced no appreciable neutral axis shift.

The deformation results for each sample holder were recorded at the center of the superconducting strand and were presented above. The results were compared to the corresponding shape of a perfect circle. In an ideal world, the deformed shape would match that of a perfect circle indicating a true pure bending condition. The deformed shape of each sample holder was characterized over its entire bending range. As indicated by the results presented in the prior sections, the deformed shape of the samples never exactly matched the shape of a perfect circle. This was an expected characteristic based on the mechanical limitations of the pure bending device. Although the deformations were not exactly the same shape as a perfect circle, the above results show that for all bending states up to 1.0% the deviation from a perfect circle was insignificant in all three sample holders.

After the bending increased above 1.0%, the deviation of the samples became substantial. At high bending, the deformed shape had slightly less bending curvature in the middle of the sample holder and slightly more bending curvature at the ends. This deformation caused there to be a slightly lower strain in the middle of the sample and a gradual increase to a slightly higher strain at the ends of the sample. This strain behavior was identified for both the medium and high bending sample holders above 1.0%.

4.5 Lorentz Load Models

Although the strand-in-channel models presented prior are useful in determining how the sample holder affects the strain in the strand they ignore the electromagnetic loading that is experienced during operation and testing. Therefore, it is important to develop models that include this electromagnetic Lorentz load so its effect on the strain in the strand can be determined. The Lorentz load will also be transmitted from the strand into the sample holder and therefore its overall affect will be investigated. The Lorentz load simulations presented below use the strand-in-channel models from above and add a uniform distributed load to the sample. The distributed load represents the electromagnetic Lorentz force that acts on the superconducting strand during testing and operation.

The high bending sample holder is the most vulnerable to deformation due to Lorentz loads because of its narrower width. For this reason it is unclear whether the high bending sample holder can adequately withstand the higher loads at low bending strains. In addition to this, the high bending sample holder has no channel

walls making the strand defenseless against deformation in between the support ribs while under loaded. For these reasons, simulating the high bending sample holder with an applied Lorentz load over the entire bending range up to 1.4 % setting strain was of interest. These simulations would therefore represent the worst case scenario for the Lorentz load effects.

At each bending state, the strand was loaded in 1 kN/m (68 lbs/ft) increments up to a max load of 5 kN/m (342 lbs/ft). This load is representative of the maximum load that could be experienced during testing based on the potential current in the sample and amount of background magnetic field. Results for applied bending strains of 1.4%, 0.6% and 0.0% (flat beam) under an inward Lorentz load of 1 kN/m, 3 kN/m and 5 kN/m are presented in the first three sections.

The current direction within the magnetic field determines the direction of the Lorentz load that the sample experiences. Consequently, the effect that current direction could have was also investigated and two sets of simulations were conducted; one with a radially inward pointing load and the other with a radially outward pointing load as indicated in Figure 4.29.
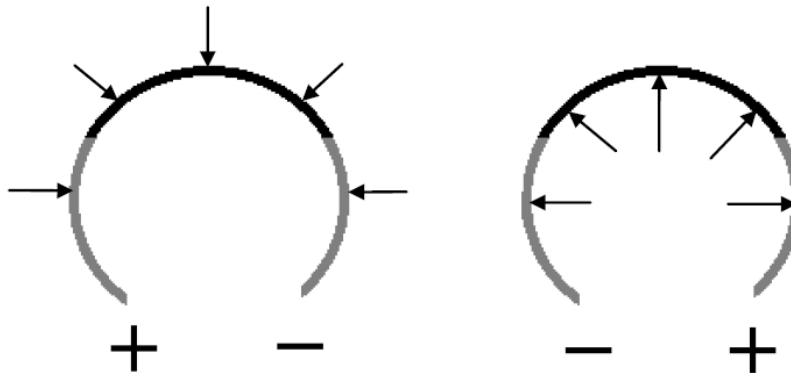
Figure 4.29 – Schematic of radially inward (left) and outward (right) Lorentz loads.

The normal current direction is indicated on the left and corresponds to an inward Lorentz load. The reversed current direction is presented on the right and corresponds to a radially outward Lorentz load.

4.5.1   Lorentz Load Effect At 1.4% Bending Strain

As mentioned above, the strand is likely to deform in between the support ribs while under loading. To determine the degree of deformation, the longitudinal strain in the sample was recorded and is presented below in Figure 4.30. The strain results in this plot are for inward Lorentz loads at a setting bending of 1.4% strain. The strain results were collected at the outer surface, inner surface and the center of the strand.
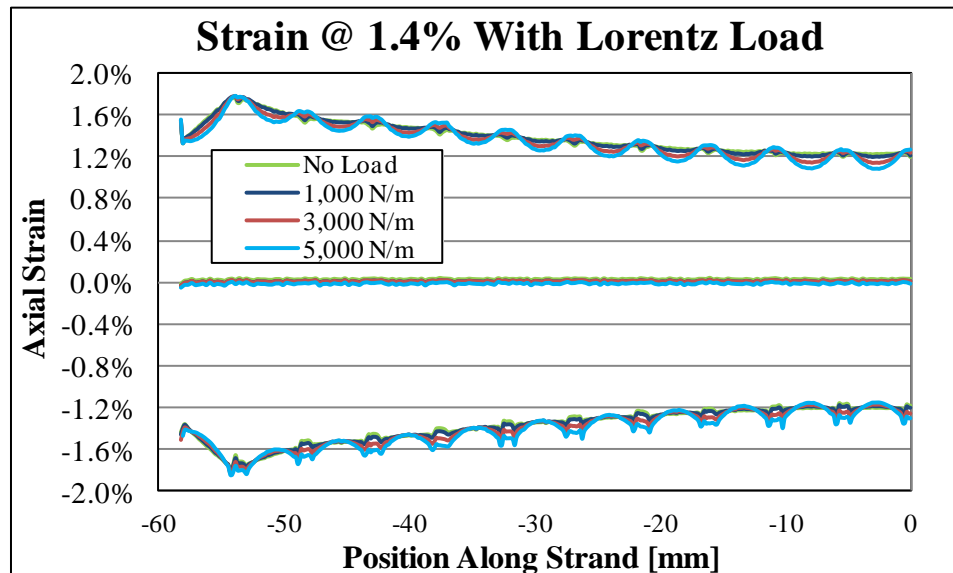
Figure 4.30 – Longitudinal strain under inward Lorentz load at 1.4% strain.

From the above results it is evident that the addition of the Lorentz load, no matter how large, creates strain fluctuations along the strand in the high bending sample holder. As the uniform distributed load is applied, in between the support ribs the

74

sample deflects in the direction of the load. This "localized" deflection or bending creates the strain fluctuations shown in Figure 4.30. The results also show that the magnitude of the fluctuations increases with the magnitude of the Lorentz load. In addition to this, the magnitude of the fluctuations is only about 0.2% at the maximum loading case which is still smaller than the fluctuations caused by the bowing of the channel walls.

The strain results under Lorentz load had the same general strain behavior over the length of the sample. Thus, the deformed shape of the sample holder is probably unaffected by the addition of the Lorentz loads. To validate this prediction the deformed shape of the sample holder at 1.4% bending under inward Lorentz loads is presented in Figure 4.31 below.
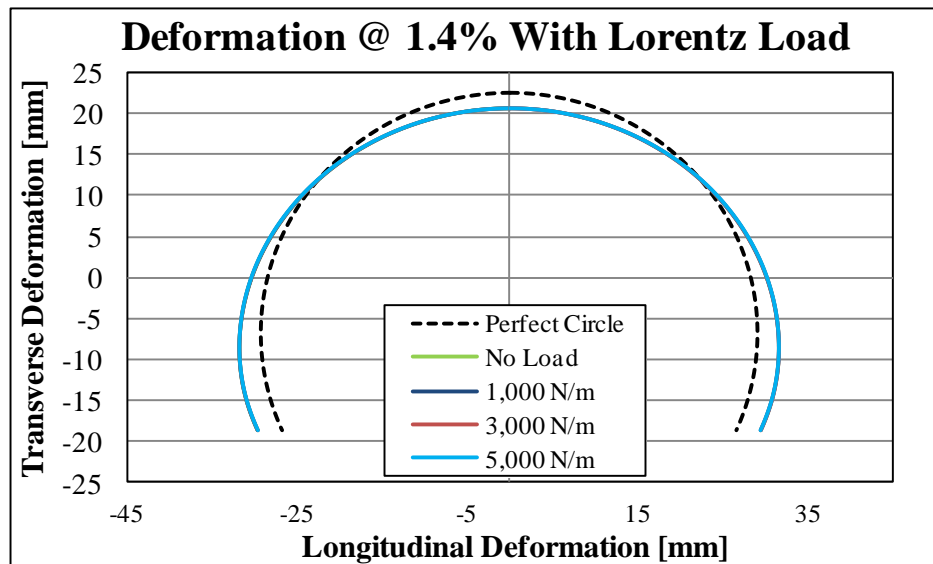
Figure 4.31 – Deformed shape under inward Lorentz load at 1.4% bending.

In the plot above, the loaded curves are shown in purple, red and blue. The no load curve is depicted in green. All of these curves are indistinguishable from each other and are indicated in the above plot by the light blue curve. This

75

indicates that the Lorentz load has minimal effect on the overall deformed shape of the strand at this amount of bending. The high curvature of the sample holder appears to help resist the loading in a similar fashion to archways and arch-dams.

4.5.2 Lorentz Load Effect At 0.6% Bending Strain

The strain results for the sample under loading at 0.6% bending are presented in Figure 4.32. From the results, the strain distribution appears to have the same fluctuating behavior that was found for the 1.4% bending case. The characteristics of the fluctuations are very similar and the magnitude is roughly identical to that found for the 1.4% strain case under the same loads. This similarity in results makes sense because the spacing between the ribs is the same and therefore the strand has the same amount of freedom to deform under loading.
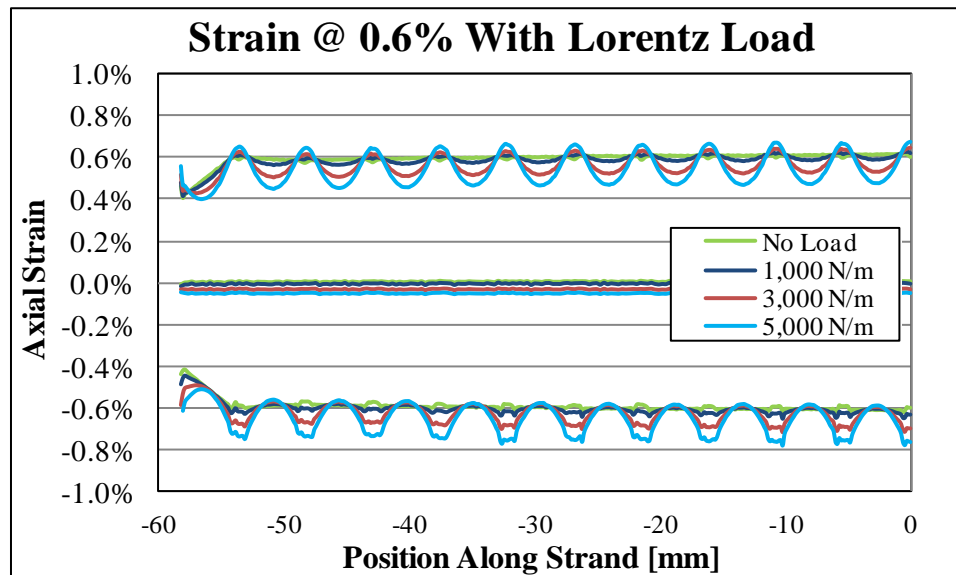
Figure 4.32 – Longitudinal strain under inward Lorentz load at 0.6% strain.

The overall strain trend under the applied Lorentz load again appears to follow the same trend as the no load results. This implies that the electromagnetic loading

does not affect the deformed shape of the sample holder at this amount of bending. To validate this, the deformed shape of the sample holder under loading is presented in Figure 4.33. The results are shown for 0.6% bending and are plotted along with the shape of a perfect circle. From the results, it appears that even under the maximum load the difference in the deformed shape from the no load scenario is not distinguishable and thus the Lorentz load effect is trivial under this bending curvature. Overall these results show that at 0.6% bending strain the curvature of the sample holder still adequately resists the Lorentz load.
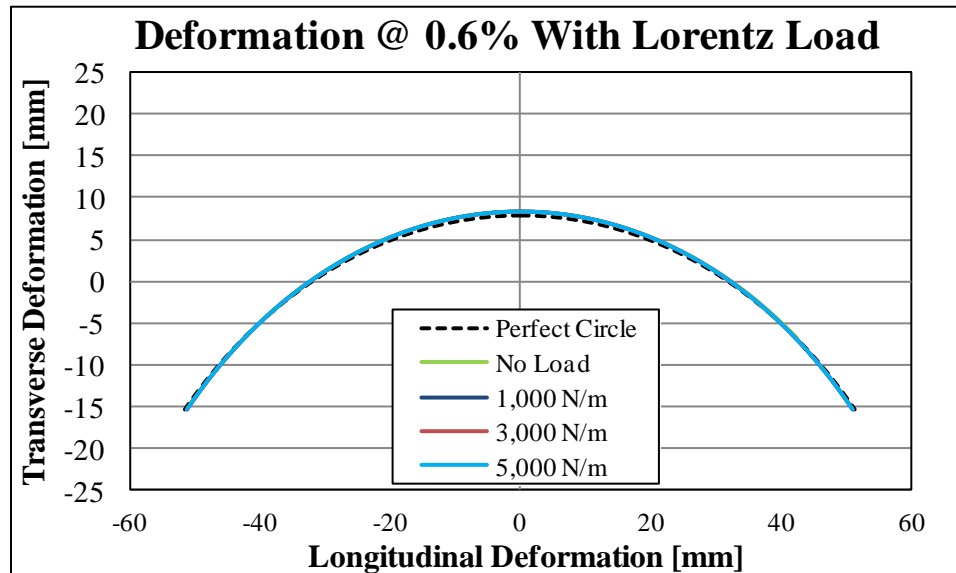
Figure 4.33 – Deformed shape under inward Lorentz load at 0.6% strain.

From the results presented above, it can be observed that the strain and deformation behavior at 0.6% bending is acceptable. In other words, the high bending sample holder performs adequately down to this low bending state. This bending state is below the designed bending range of the high bending sample holder prescribed by Mallon [16]. This confirms the high bending sample holder is suitable to cover a new bending range between 0.6% and 1.4% strain.

4.5.3 Lorentz Load Effect At 0.0% Bending Strain

At zero bending, the critical current of the superconducting samples is largest because there is no bending strain in the sample to degrade its performance. This maximum current in turn produces the maximum Lorentz load on the sample. In addition to this, the sample holder is in a flat configuration and therefore is in its most vulnerable state. Without any bending curvature the sample holder has a harder time resisting the Lorentz loads. For these reasons, the Lorentz load effect at zero bending is the most severe and thus is of most importance.

To quantify the extent of this effect at zero bending the deformation of the sample was initially considered. The deformed shapes of an initially flat sample holder under increasing inward Lorentz loads are presented in Figure 4.34.
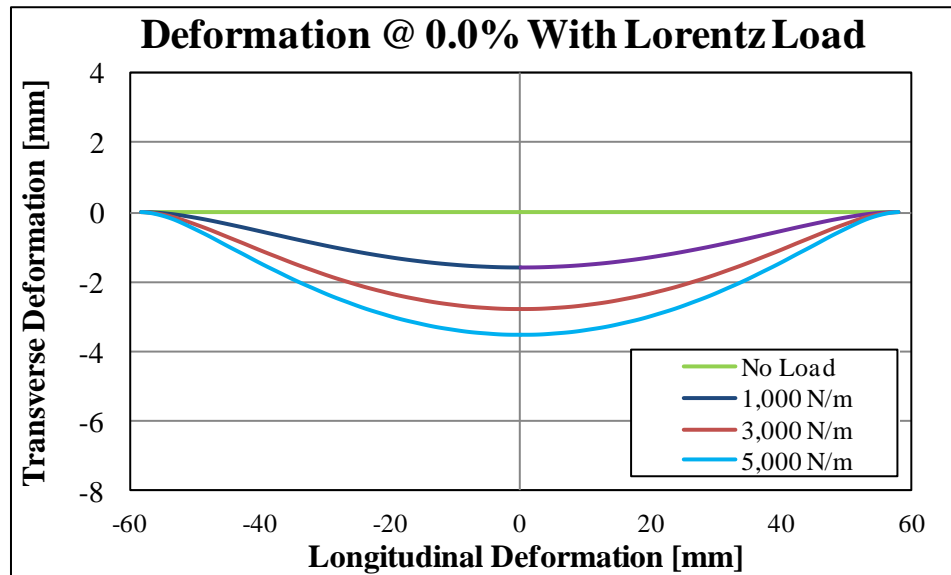
Figure 4.34 – Deformed shape under inward Lorentz load for zero bending.

The results presented above confirm our initial prediction and indicate that the middle of the sample holder bows in the direction of the loading. At the exact

middle, the sample experiences roughly 3.5 mm (0.138 inches) of deflection for a Lorentz load of 5 kN/m. This deformation of the sample will place it into tension and bending. This will apply strains to the sample degrading its current carrying ability. For this reason, the deflection at zero bending is an adverse characteristic.

This inward bowing or deflection seen in the middle of the sample (0 mm) is caused by the sample holder tilting or deforming in the direction of the load. This tilting effect is shown for a Lorentz load applied to the top strand in Figure 4.35. This figure displays 4 FEA images of a flat sample holder under zero bending with a Lorentz load applied horizontally to the left. The image on the left is for no load. The next image is for a 1 kN/m load, followed by a 3kN/m load and lastly a maximum load of 5 kN/m is shown in the image on the far right.
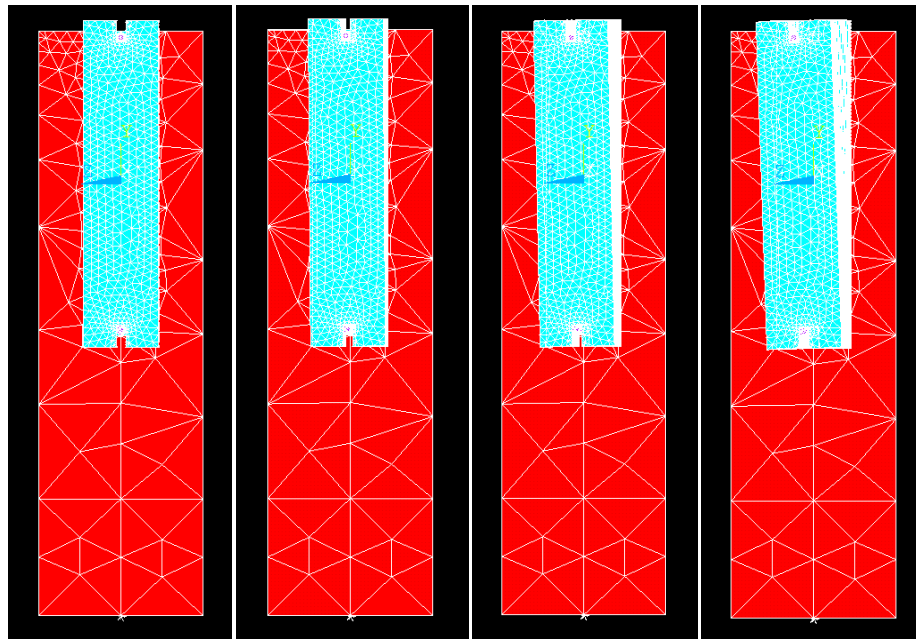
Figure 4.35 – Increasing Lorentz load on the top sample indicating a tilting affect.

From the FEA images above, it is clear that the top of the sample holder gets tilted in the same direction as the loading. It is also evident that the amount of

79

tilting or deformation grows as the load is increased. This tilting affect in the middle of the sample holder is what causes the bowing deformation of the sample shown in Figure 4.34. The deformation of the sample holder will inevitable influence the strain state of the sample. To determine this effect, the axial strain along the length of the same was plotted in Figure 4.36. The strain results are only shown only for a Lorentz load of 5 kN/m for clarity.

Strain @ 0.0% With Lorentz Load
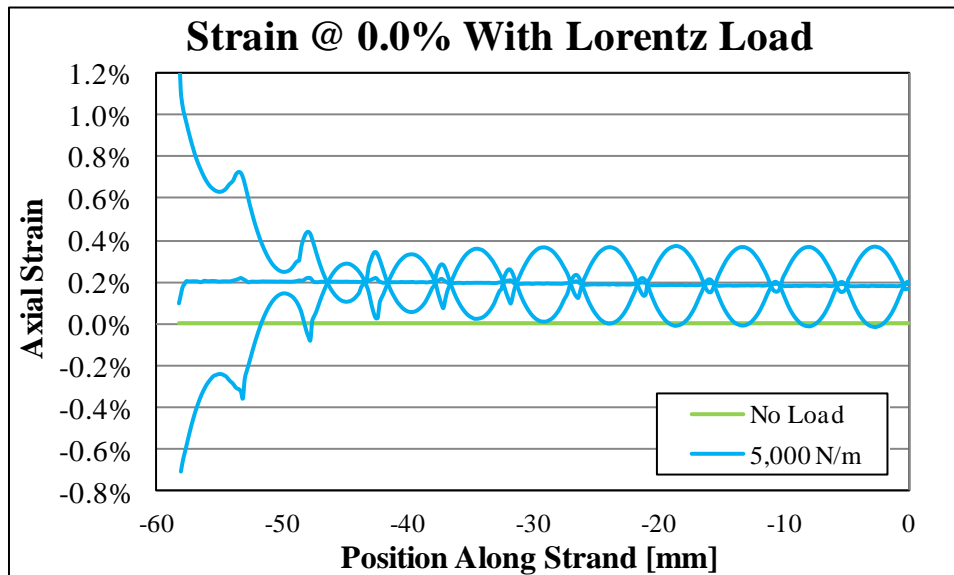
Figure 4.36 – Longitudinal strain under inward Lorentz load for zero bending.

From the above results, it is evident that the inward deformation under a Lorentz load directly influences the strain state of the sample. As the load increases the bowing of the sample worsens, which applies a growing tensile strain to the strand. This is shown best by the large tensile strain at the center of the strand. Another trend identified was the decrease in strain on the surface of the sample near the torque arms. This decrease is due to a double bending effect which was caused by the end of the sample holders being fixed from rotation. Both of these strain behaviors are undesirable because they decrease the accuracy of our critical

current results at zero bending. At zero bending there should be no external strain in the sample, therefore allowing it to carry its maximum current.

The strain and deformation results presented for the high bending sample holder indicated the worst case Lorentz load behavior because it is the narrowest sample holder. Therefore, to identify the Lorentz load effect on the widest sample holder (low bending) the deformations of the two sample holders were compared in Figure 4.37. Both sample holders were compared at zero bending under the maximum electromagnetic load of 5 kN/m.
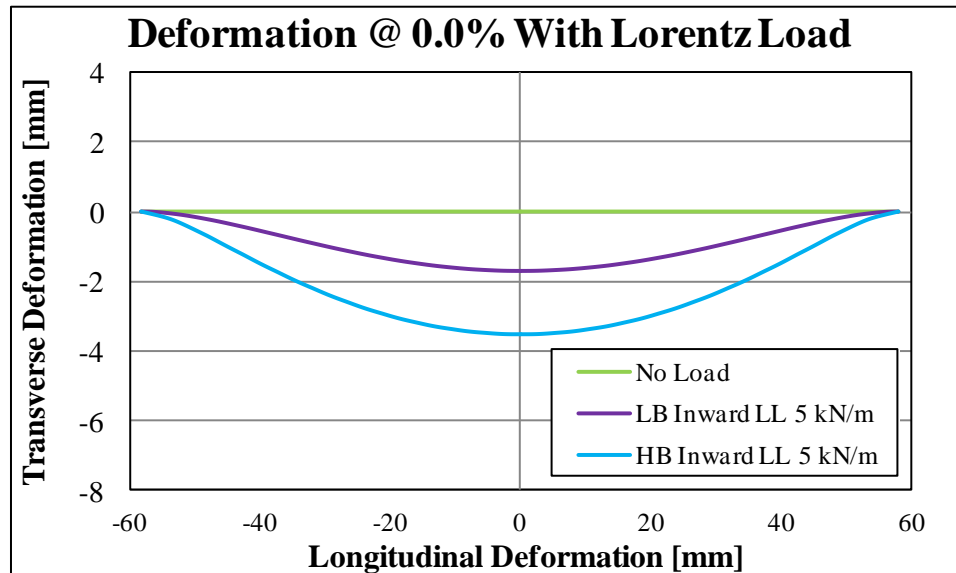
Figure 4.37 – Deformed shape comparison under Lorentz loading at zero bending.

These comparison results show that this large Lorentz load still bows the middle of the sample; however, the degree of deformation for the low bending sample holder was considerably smaller than for the narrower high bending sample. This exemplifies why the low bending sample holder was originally designed with a greater thickness; to help resist the higher Lorentz loads at low bending strains.

4.5.4 Reversed Current Effect

As mentioned previously, the current direction changes the radial direction of the Lorentz load and therefore may change the effect it has on the samples. To investigate this, reversed current simulations were run. The standard or normal current direction that is used in experiments produces a radially inward pointing load. A radially outward Lorentz load is generated by running the current through the sample in the reversed direction as indicated above in Figure 4.29.

To determine the difference the current direction has, the results for an inward and an outward Lorentz load are compared together in the following plots. The results for all succeeding plots are compared at the max loading condition of 5 kN/m. This load was chosen because it is the worst case scenario. A comparison of the axial strain at 1.4% applied bending strain is shown below in Figure 4.38.
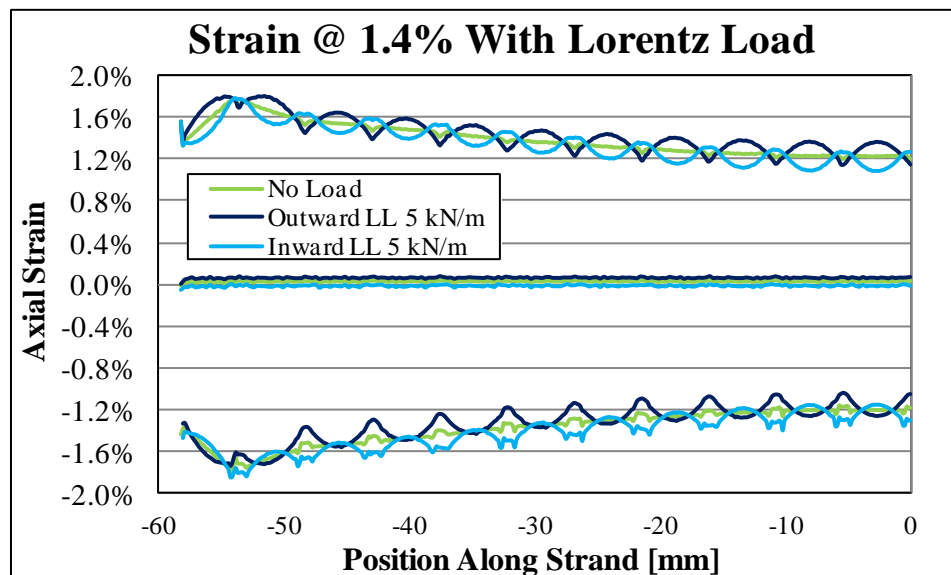
Figure 4.38 – Longitudinal strain comparison under reversed current at 1.4% bending.

The main difference between the strain fluctuations presented above is their

direction. For the outward loading case the magnitude of fluctuations is highest in between the support ribs and for the inward loading case the magnitude is lowest.

In addition to the fluctuation direction, their characteristics are also slightly different near the ribs on the inner surface. On the inner surface, as the curved strand bends over the rectangular rib it makes contact at the hard edges creating pressure points. For an inward Lorentz load these pressure points are increased and for an outward Lorentz load these pressure points are reduced.

The comparison of the strain results for an applied bending of 0.6% are presented in Figure 4.39 below. These results show the same characteristic differences as found in the 1.4% bending case shown above in Figure 4.38.
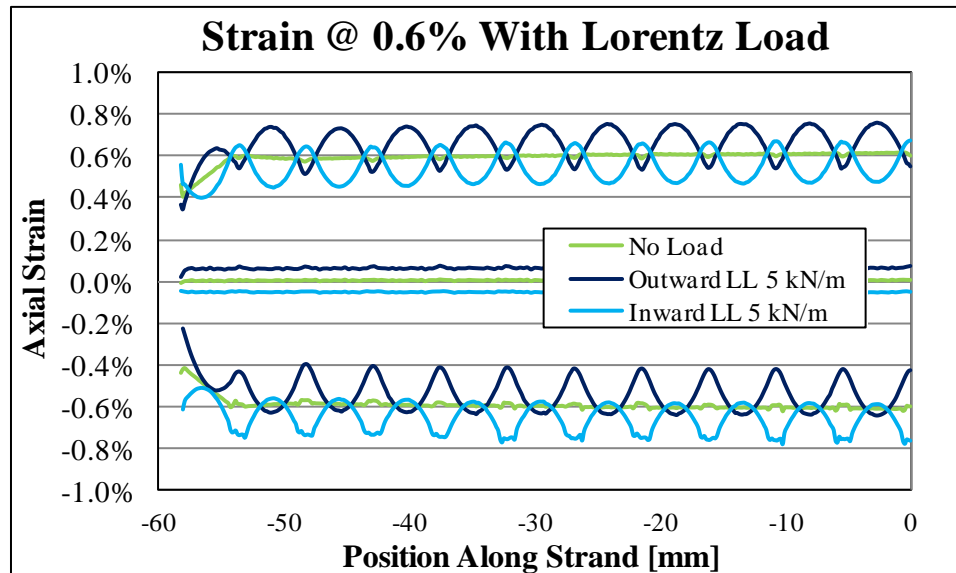
Figure 4.39 – Longitudinal strain comparison under reversed current at 0.6% bending.

At 1.4% and 0.6% the deformed shape of the high bending sample holder under an outward facing Lorentz load was found be indistinguishable from the deformed shape under no load. This was the same behavior that was experienced for the

83

inward pointing load which was presented above in Figure 4.31 and Figure 4.33. In conclusion, regardless of current direction the electromagnetic loading at these two bending states does not affect the sample holder shape. That being said, the outward Lorentz load does have an effect on the sample holder at zero bending.

At zero bending the outward Lorentz load has a similar but opposite effect on the deformation of the sample holder as seen in Figure 4.40. For this outward load, the middle of the sample holder bows outward in the direction of the load. The max deformation at the middle of the sample holder is approximately the same for both current directions. This is an expected characteristic for a flat beam. Because the two Lorentz loads produce equal deflections in opposite directions for an initial flat sample holder, the effect on the strain in the sample is the same. This effect can be seen in Figure 4.36 which indicates that the middle of the strand is being placed in added tension due to the deformation.
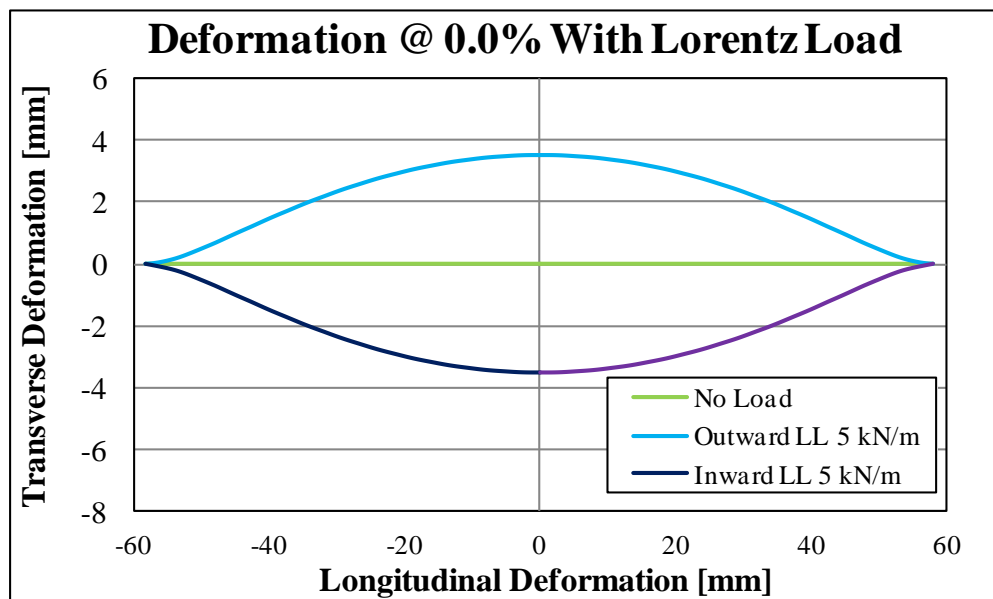
Figure 4.40 – Deformed shape comparison under reversed current at zero bending.

4.5.5 Lorentz Load Summary

Although Lorentz load results were only presented for three bending cases, simulations were run for all bending strains. The results between 0.6% and 1.4% bending strain all had the same strain magnitudes, fluctuations and characteristics. They also showed that the loading had no noticeable effect on the deformed shape of the sample holder over these bending strains.

In contrast to this, the results between 0.0% and 0.6% bending did show a change in behavior. The sample holder deformation was seen to continually worsen as the strain was decreased. Because the deformation becomes significant at low bending, the strain behavior in the sample also is influenced at low bending. The strain behavior over the length of the sample varies in accordance with the degree of deformation, while the strain fluctuations remain a consistent magnitude.

Overall, the most obvious finding was that the high bending sample holder was not sturdy enough to be used at zero bending. The narrow sample holder allowed far too much tilting and deformation while under loading. The thicker low bending sample holder provided more support and experienced less tilting.

Another important finding was that at a bending of 0.6% strain the high bending sample holder performed adequately. This bending level is 0.2% less than its design range and is now low enough to overlap the range of the low bending sample holder which covers up to 0.7% bending. Therefore, these results indicated that these two sample holders could cover the entire range, eliminating the need for the medium bending sample holder.

Another discovery was that the direction of the Lorentz load had minimal effect on the overall behavior of the sample. At low bending, below 0.6%, the effect of the Lorentz load direction was slightly different, in that an outward load created a slight tensile shift to the sample while an inward load produced a slight compressive shift. However, once back at zero strain where the Lorentz load deformation was worse, the strain in the sample was identical because the sample deformation only changed directions.

Lastly, the magnitudes of the strain fluctuations for a Lorentz load of 5 kN/m were consistently around 0.2% for the entire bending range. Although this is a much lower magnitude of fluctuation than found in the low and medium bending sample holders, it is still large enough to produce an unacceptable amount of error. Consequently, the sample holders should be redesigned to minimize this fluctuation error under the electromagnetic loading.

4.6 Deviation from Setting Strain

The applied bending strain is also referred to as the setting value of the device and corresponds to the ideal strain for the sample holder in a true state of pure bending. However, as mentioned above the deformed shape of the sample holder does not perfectly match the shape of a perfect circle at high bending due to mechanical limitations of the device. The FEA results have shown that this deviation in deformed shape of the sample holder produces a non-uniform strain state in the sample. For this reason, the actual strain that the sample experiences will not be slightly different from the setting strain of the device.

More specifically, the results presented prior showed that above a setting strain of 1.0%, the strain in the middle of the sample is slightly less than the setting value and the strain at the ends of the sample is larger than the setting value. Because the level of strain varies along the sample's length, it is advantageous to determining an average strain in the stand over the voltage tap region used in the experiments. This will allow us to determine the actual strain in the sample that produces the critical current results that were recorded.

The experimental results are taken from the short voltage taps whenever possible and therefore are of most interest. The short voltage taps span a 50 mm region in the middle of the sample. To quantify the actual average strain on the surface of the sample over this region, the strain data from paths A and I in Figure 4.15 were taken. This strain data for the outer and inner surface of the sample was averaged over the span of the short voltage taps in the middle of the sample. This average strain incorporates all effects including strain fluctuation and neutral axis shift by averaging the strain results from both compressive and tensile side.

This average actual strain on the surface of the sample for the short voltage tap region is plotted versus the setting value of the sample holder and is shown in Figure 4.41. In this plot the black curve represents the ideal relationship between setting strain and actual strain. The blue curve represents the real relationship between the setting strain of the device and the actual strain felt in the sample. This blue curve indicates that the actual strain over the short voltage tap region closely matches the ideal strain up to a setting value of 0.8%. Above a setting

87

value of 0.8%, the actual strain begins to significantly deviate from the ideal

strain case. This deviation was predicted based the limitations of the device.
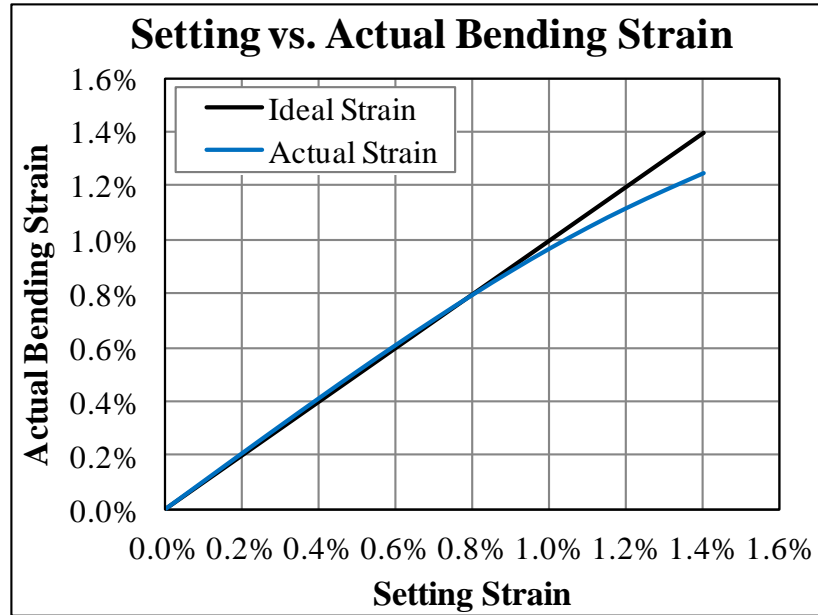
Figure 4.41 – Applied setting strain vs. actual strain in sample.

The results for the actual strain above a setting value of 0.8% are summarized in

Table 1. These values indicate that at 1.4% setting strain, which is the maximum

bending state of the device, the actual strain on the outer surfaces of the sample

over the short voltage tap region is only 1.25%. This correlates to an error of over

12% between the applied setting value and the actual strain in the sample.

Table 1 – Actual sample strain compared to setting strain.

Setting Bending Strain	Actual Strain in Sample	Percent Error
0.8	0.797	0.4
0.9	0.885	1.7
1	0.968	3.3
1.1	1.046	5.1
1.2	1.119	7.3
1.3	1.185	9.7
1.4	1.248	12.2

These actual strain values presented above were determined from the FEA strain results of the current high bending sample holder designed by Mallon. This same process was used to characterize the actual strain in the sample for the new sample holders which are described in the following section. Determining this actual strain was important to improving the accuracy of our experimental results by allowing us to plot the critical current values against the actual strain that in the sample. Therefore, from this point forward all experimental data will be plotted against the actual strain that the sample experiences instead of the setting strain of the device, as was done previously.

4.7 Summary of Findings

The strand-in-channel results from section 4.3 showed that the channel wall of the low and medium bending beam creating very large strain fluctuations by bowing into the strand and creating pressure points along its length. On top of that, these large fluctuations were found to increase upon the application of the electromagnetic Lorentz load. The smallest magnitude of the strain fluctuations felt on the outside of the superconducting strand for the two sample holders was 0.5%. This degree of fluctuations produces too much error and creates too much uncertainty in the validity of the experimental measurements. It is also the most likely cause of the sharper degradation of critical current experienced in these sample holders as found by King [2]. Therefore the channel wall bowing effect must be resolved or removed for future sample holder designs.

The effect of the Lorentz load presented in section 4.4 revealed that even though

the high bending sample holder only supported the superconducting strand intermittently at each support rib, the strain fluctuations produced under maximum loading were only 0.2%. This degree of fluctuation is less than half of what was seen in the low and medium bending sample holders and therefore produced much less error and uncertainty. The realization that no channel walls produced improved longitudinal strain results has made it the key feature for the development of the new sample holder designs. The extent of the fluctuations in this sample holder is still too large and penetrates into the Nb_3Sn layer of the strand. Therefore the new sample holder designs will have to focus on reducing the magnitude of fluctuations even further.

5.0 Sample Holder Optimization

The FEA modeling in the preceding section has showed that the channels walls of the low and medium bending sample holders bow into the channel pinching the strand. This pinching creates unusually high axial strain fluctuations that may be the cause of the steep critical current degradation found by King [2]. To allow for a more consistent and accurate critical current degradation over the entire bending range a new set of samples holders will be designed.

All the new sample holders will have no channel walls which will give each beam the same strain characteristics. In addition to making the strain characteristics uniform throughout all sample holders, the goal is to also minimize the axial strain fluctuations experienced in the strand under loading. If the magnitude of strain fluctuations can be decreased below a certain threshold, any error caused by the fluctuations can be proven negligible.

To be able to use the current testing infrastructure including torque arms, gear box and probe the current sample holder design cannot be changed drastically. The new sample holders must remain the same overall size and have the same copper terminals. The new sample holder must also remain the same material due to its matching coefficient of thermal expansion and excellent strength at cryogenics. Therefore, the new sample holders were developed by only modifying the current high bending sample holder design. The new sample holder designs optimized the width, thickness and spacing of the support ribs to minimize strain fluctuations.

5.1 Rib Optimization Using FEA

A schematic of the sample holder indicating the modifiable support rib parameters used for the design optimization is shown below in Figure 5.1. The three parameters that will be altered are the rib width (w), rib spacing or span (s) and the rib thickness (t). The yellow region in the schematic is referred to as the beam. The beam width (wb) cannot be modified because it is chosen based on the selected bending range for the sample holder.
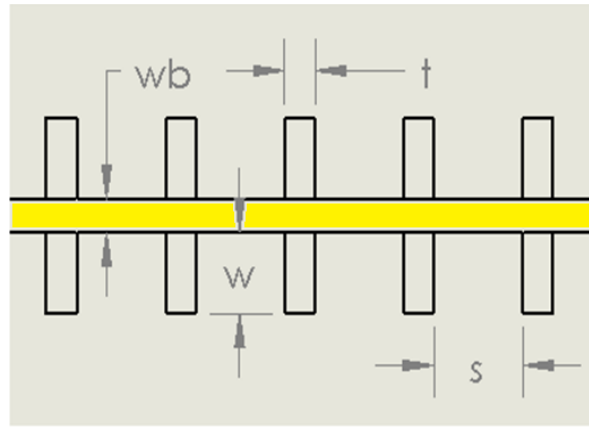
Figure 5.1 – Schematic of sample holder indicating rib design parameters.

The optimization of the sample holder rib design will be achieved through a parametric FEA study that will determine the influence of each rib parameter on the axial strain behavior. For the parametric study three sets of iterations will be conducted. Each set of iterations will only change one parameter to isolate that parameters effect on the strain characteristics of the strand. The first set will vary the rib spacing or span, the second set will vary the rib thickness and the last set will vary the rib width. The results of the parametric study will shed light on the influence that each parameter has on the strain characteristics which will facilitate an optimal sample holder design.

The results of the parametric study presented below are for an applied bending strain of 1.0%. This was chosen as a good characteristic bending state for the sample holder optimization because at this bending state the Lorenz load affect is isolated to creating strain fluctuations. It is also a good bending strain to represent medium and high bending because the strain characteristics over this range are very similar. This modeling only considers the electromagnetic load case of 5 kN/m (342 lbs/ft) because it represents the worst case condition that the sample holders will be designed for. Therefore the loading will correspond to the absolute largest strain fluctuations that the strand would ever experience in operation.

5.1.1 Rib Spacing (Set 1)

The rib spacing parameter governs the span in between support ribs. The larger the span the more freedom the strand has to deform. Therefore, this parameter is expected to have the largest influence on its axial strain characteristics. Three simulations will be run for this set and will include the following rib spacing; 6 mm (0.236 inches), 4 mm (0.157 inches) and 2 mm (0.0787 inches). These spacings are shown in Figure 5.2 and represent iterations 1, 2 and 3 respectively. These spans were chosen to characterize both extremes.
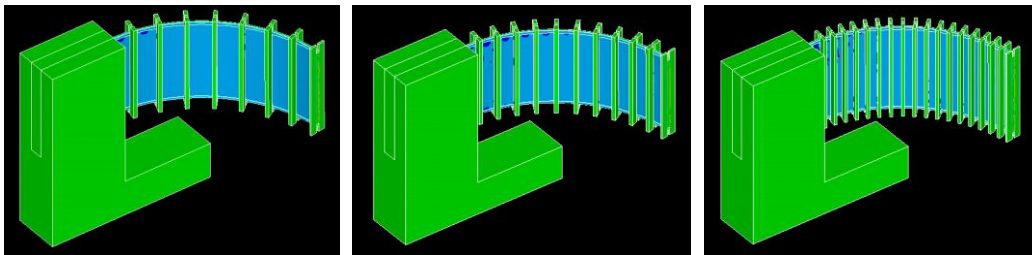
Figure 5.2 – FEA models with varying spacing between ribs (iterations 1, 2 & 3).

The ANSYS® simulation results shown in Figure 5.3 plot the axial strain that the

93

strand experiences on its outer surface (tensile side), inner surface (compressive side) and its center of strand (neutral axis). Iteration 1 (6 mm spacing) is shown by the light blue curve, iteration 2 (4 mm spacing) is shown by the grey curve and iteration 3 (2 mm spacing) is shown by the light green curve. By comparing these three curves it is evident that the 6 mm span has by far the largest magnitude of strain fluctuations. Based on these spacing results, the first set of iterations for the parametric study has shown that the smaller the spacing or span between the ribs the smaller the magnitude of axial strain fluctuations.
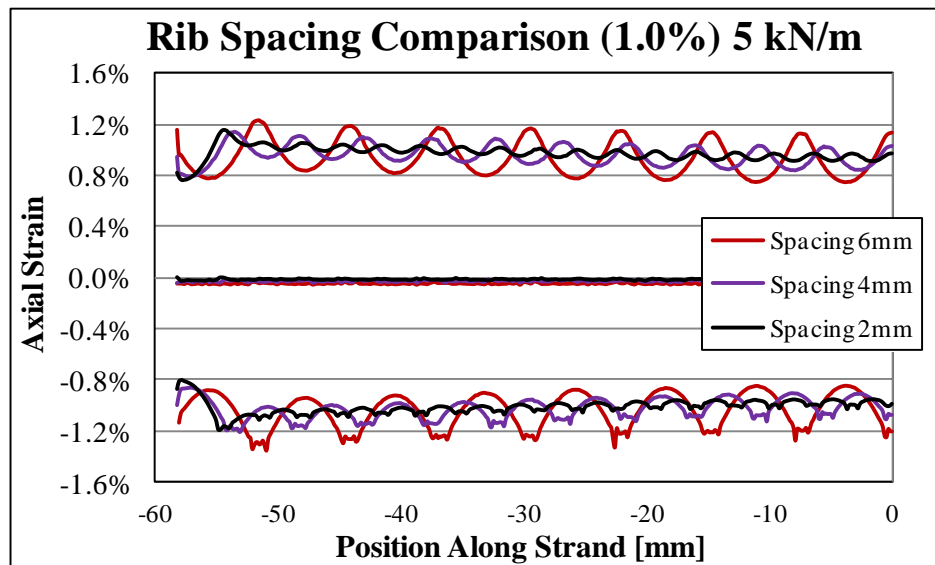
Figure 5.3 – Longitudinal strain comparison of rib spacing (iterations 1, 2 & 3).

5.1.2 Rib Thickness Results (Set 2)

The rib thickness parameter was also assumed to have a noticeable effect on the strain distribution with the strand. As the rib thickness is increased the strand will have a harder and harder time trying to curve over the rigid rectangular rib. This will most likely increase the pressure points caused by the corners contacting the strand. Set 2 also ran three FEA iterations for rib thicknesses of 3 mm (0.118

94

inches), 2 mm (0.0787 inches) and 1 mm (0.0394 inches). These thicknesses were chosen based on reasonable manufacturing sizes. The size of the thicknesses can be visualized in the FEA images of Figure 5.4.
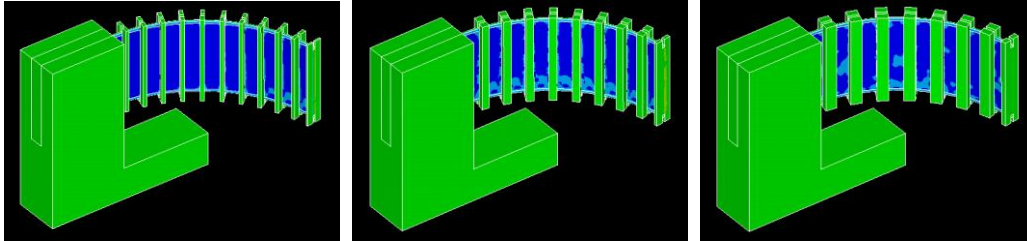
Figure 5.4 – FEA models with varying rib thickness (iterations 4, 5 & 6).

The results are presented in Figure 5.5 below which again plots the axial strain that the strand is experiencing. In the plot the light blue curve represents iteration 6 (3 mm thickness), the grey curve represents iteration 5 (2 mm thickness) and the light green curve represents iteration 4 (1 mm thickness).
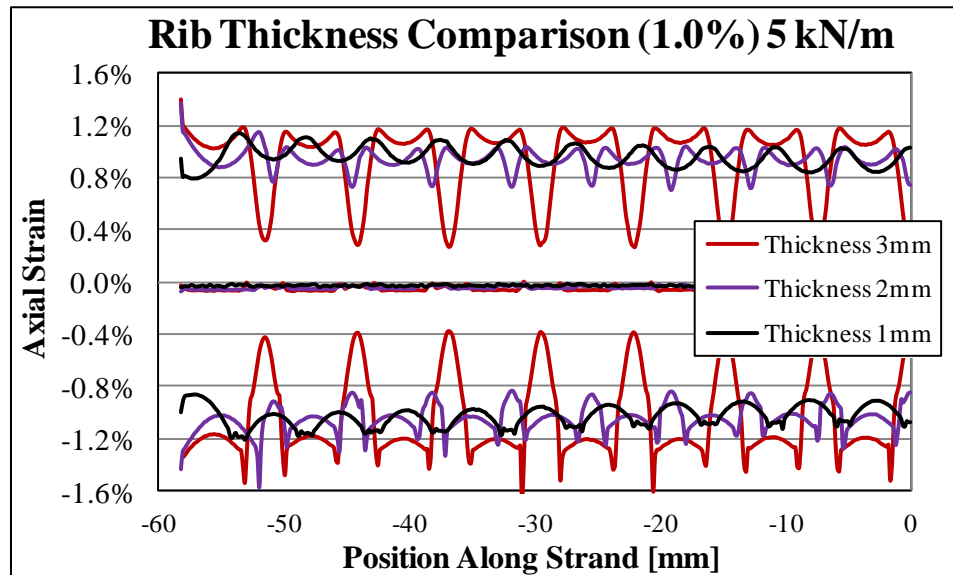
Figure 5.5 – Longitudinal strain comparison of rib thickness (iterations 4, 5 & 6).

From the results it is clear that the rib thickness can have a very large influence on the strain distribution. On the inner surface there can be seen two distinct pressure

points for the thicker rib models, as was initially predicted. These pressure points create a slight strain increase while in between these points over the length of the rib surface; the strand experiences the least amount of strain. Overall, this is an unfavorable characteristic that should be avoided. In summary, the second set of design iterations has shown that a rib thickness greater than approximately 1 mm (0.0394 inches) has an adverse affect on the sample's strain distribution.

5.1.3 Rib Width Results (Set 3)

The rib width parameter was expected to produce minimal effect on the strain distribution within the strand at this percent bending. At 1.0% bending strain the sample holder has a high curvature which naturally resists the Lorentz load without the additional need of wider ribs. The three simulations run for Set 3 used the following rib widths; 4 mm (0.157 inches), 3 mm (0.118 inches) and 2 mm (0.0787 inches). Models of these three simulations are shown in Figure 5.6.
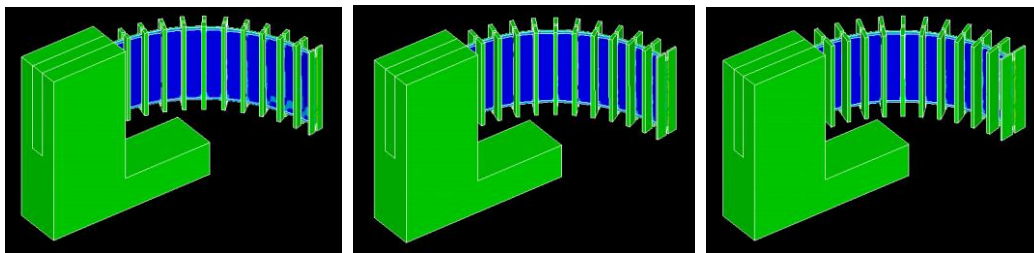
Figure 5.6 – FEA models with varying rib width (iterations 7, 8 & 9).

The axial strain results from the FEA simulations are presented in Figure 5.7. Iteration 9 (4 mm width) is shown by the light blue curve, iteration 8 (3 mm width) is shown by the grey curve and iteration 7 (2 mm width) is shown by the light green curve. The results show that all three simulations results have nearly identical strain distributions. The conclusions of the third set of design iterations

for the parametric study indicate that the rib width parameter does not have any significant influence on the axial strain distribution for a bending of 1.0%.
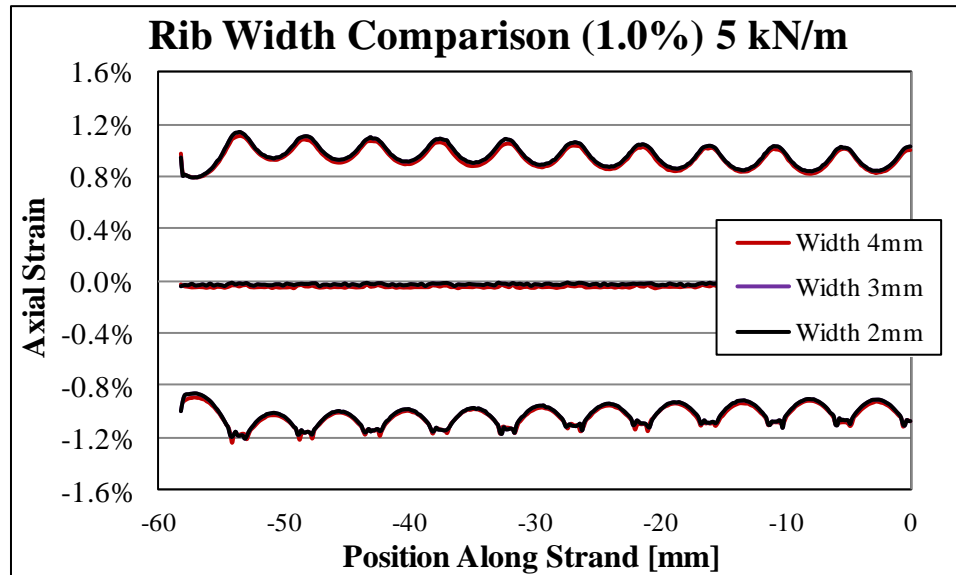
Figure 5.7 – Longitudinal strain comparison of rib width (iterations 7, 8 & 9).

One caveat to these results is that this parameter plays a major role at low bending strain and for the wider sample holders. The rib width will help mitigate the warping effect that is experienced in the thicker low bending sample holder. It will also give the sample holder more strength and rigidity which will help reduce the deformation in the sample holder at low or zero bending strain. For these reasons, the rib width parameter must be carefully considered in the designing of the new low bending sample holder.

5.2 New Sample Holder Design

Based on the conclusions of the parametric study the goal was to optimize the sample holder to have a rib thickness of 1 mm or less, spacing as small as possible and a rib width that depended on the bending range. Optimized sample holders

were developed based on these recommendations. The sample holders were also designed with cost and feasibility of fabrication in mind.

The new generation of sample holders covers the entire bending range using only two beams, a low bending (LB) beam and a high bending (HB) beam. The low bending beam will go from 0.0% to 0.7% applied bending strain and the high bending beam will cover from 0.6% to 1.4% applied bending strain.

5.2.1   General Design

Both new sample holders maintain the same overall length 116.38 mm (4.582 inches) as the previous generation allowing for the old sample mounting infrastructure to be used. The new sample holders have a slightly increased height of 27.94 mm (1.1 inches), which was chosen to eliminate complex sloping features in the copper terminals.

The width of the sample holders without ribs (beam width) remains the same as in the previous generation. The low bending beam width is 1.6764 mm (0.066 inches) and the high bending beam width is 0.80 mm (0.0315 inches). Recall that the low bending sample holder is thicker to resist the higher Lorentz loads while the high bending sample holder is thinner to avoid yielding at high strains.

5.2.2   Support Rib Design

The sample holders were designed to minimize axial strain fluctuations in the strand during loading. This was achieved by choosing the optimal design for the support ribs. As mentioned prior, the optimal support rib design includes an

appropriate rib spacing, rib thickness and rib width. Figure 5.8 and Figure 5.9

show dimensioned views of the new low and high bending sample holders. All

dimensions are shown in millimeters (mm).
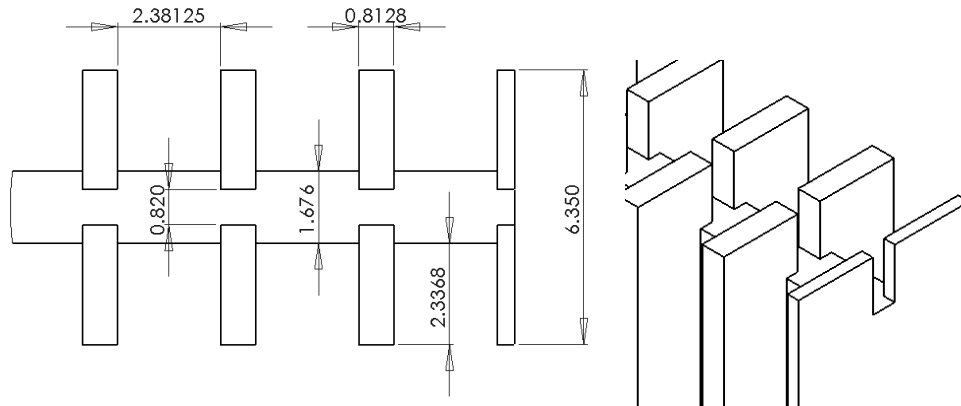
Figure 5.8 – New low bending sample holder design [mm].
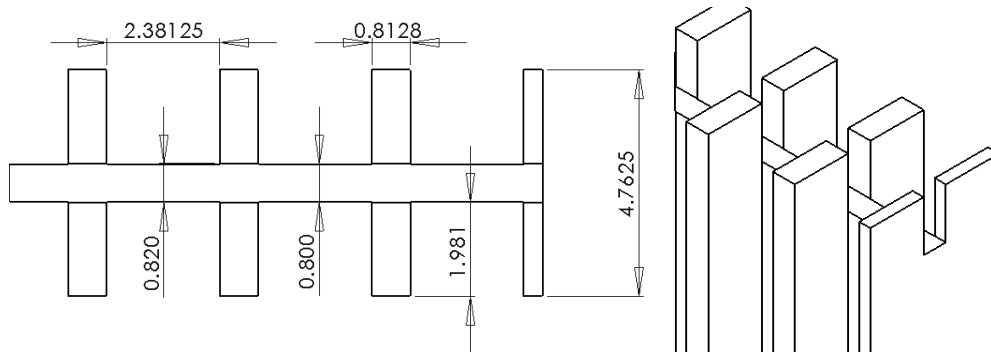
Figure 5.9 – New high bending sample holder design [mm].

Two different rib spacings were initially considered for the final design; 2.38 mm

(3/32 of an inch) and 1.588 mm (1/16 of an inch). These spacings were chosen

because they are standard sizes for end mills which are used to create the span in

between the ribs. The 1/16" tool is 30% weaker than the 3/32" tool. Therefore, to

keep machining cost to a minimum the 3/32" spacing was selected for the final

design. This chosen spacing of 2.38 mm is almost half of the original span of 4.34

mm used in the old sample holders.

The rib thickness was chosen to be as small as possible while still being large enough to support the electromagnetic loading. The rib thickness was also chosen to accommodate the desired number of ribs and spacing along the length of the sample holder. The final thickness chosen was 0.813 mm (0.032 inches) which is slightly smaller than the current design of 1.016 mm (0.04 inches).

The rib width was chosen based on the sample holder bending range. The new high bending sample holder was designed with a total width 3/16" (4.7625 mm) producing a rib width of 1.981 mm (0.78 inches). This is the same width as the original high bending sample holder which was found in previous experiments to have satisfactory performance against the Lorentz load at high bending states.

The new low bending sample holder was designed with a total width of 1/4" (6.35 mm). This is wider than the original low bending sample holder. This wider total width increases the width of the support ribs to 2.3368 mm (0.92 inches) from 1.543 mm (0.0607 inches) on the original design. This wider rib width was chosen to help reduce the greater amount of warping that is experienced on the thicker beam width. It was also chosen to help reduce the severity of the Lorentz load tilting effect which deforms the sample at low bending strains.

Both new sample holders feature 35 evenly spaced support ribs on each side of the beam. This is an increase from the original samples holders 21 support ribs. This increase greatly reduces the spacing between the ribs and should significantly reduce the magnitude of strain fluctuations seen in the strand. The change in the new sample holder design is best visualized in Figure 5.10 which

shows a CAD image of the old and new sample holder designs. The old design is

shown on the top and the new design on the bottom.
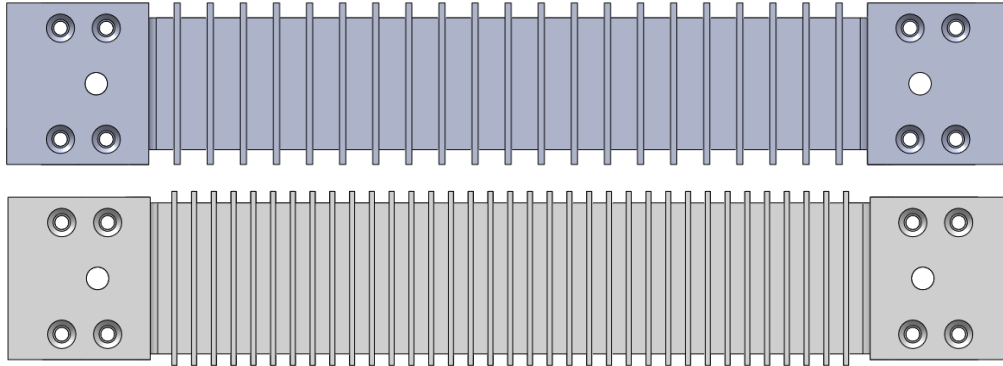
Figure 5.10 – Old (top) and new (bot) sample holder designs.

5.3 FEA Validation of New Design

The behavior and performance of the new sample holder designs were analyzed

using FEA simulations as was done previously. To verify the improvements of the

new designs, the axial strain results for the old and new high bending sample

holders were plotted together in Figure 5.11.
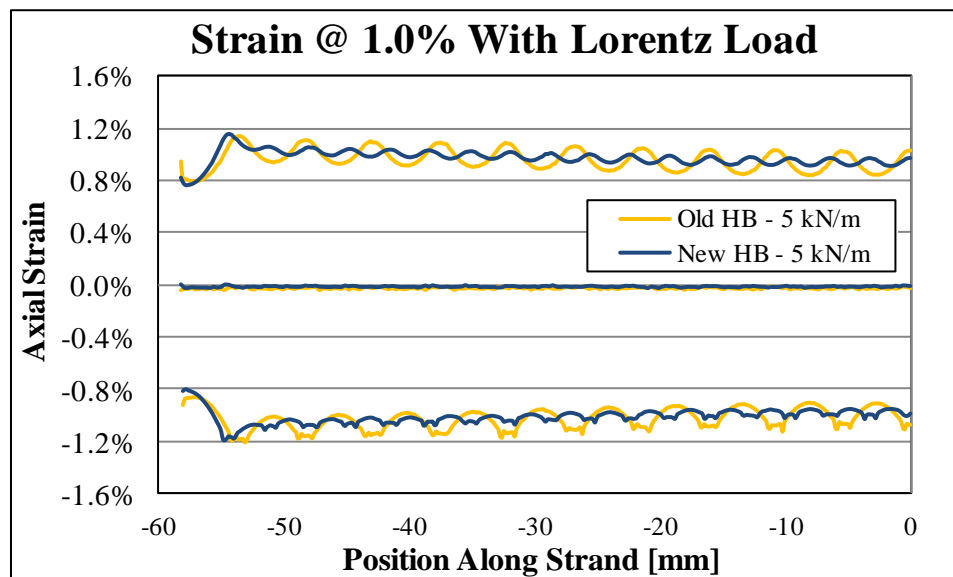
Figure 5.11 – Longitudinal strain improvement of new high bending sample holder.

The plotted results above were taken for a setting strain of 1.0% with an applied Lorentz load of 5 kN/m. The strain in the sample was taken at the outer surface, inner surface, and center. The dark blue curves represent the new sample holder design with optimized ribs and the orange curves represent the old high bending sample holder design.

The FEA simulation results presented above show a clear decrease in the magnitude of the strain fluctuations for the new sample holder design. Under closer inspection the magnitude of fluctuations has been decreased by approximately half, from 0.2% strain to 0.1% strain. The span of the new sample holder was also reduced by roughly half; which verifies that there is a direct relationship between the rib spacing and the magnitude of strain fluctuation. Because the magnitude of the fluctuations has been reduced on the surface of the sample, the depth that these fluctuations penetrate has also been reduced. Therefore, the filaments inside the copper stabilizing layer will be experiencing a uniform strain with minimal or no fluctuations.

This reduction in the magnitude of the strain fluctuations is even more significant for the new low bending sample holder. Figure 5.12 below shows the axial strain on the surface of the strand for both the new and old low bending design. These results are taken at 0.6% bending strain under a 5,000 N/m Lorentz load. The results show that the very large strain fluctuations in the old low bending sample holder, which were caused by the channel wall bowing effect, have been completely eliminated. The new low bending sample holder is found to have a

very similar strain distribution to the new high bending sample holder. This verifies our goal of creating uniform strain behavior in all sample holders.

Strain @ 0.6% With Lorentz Load
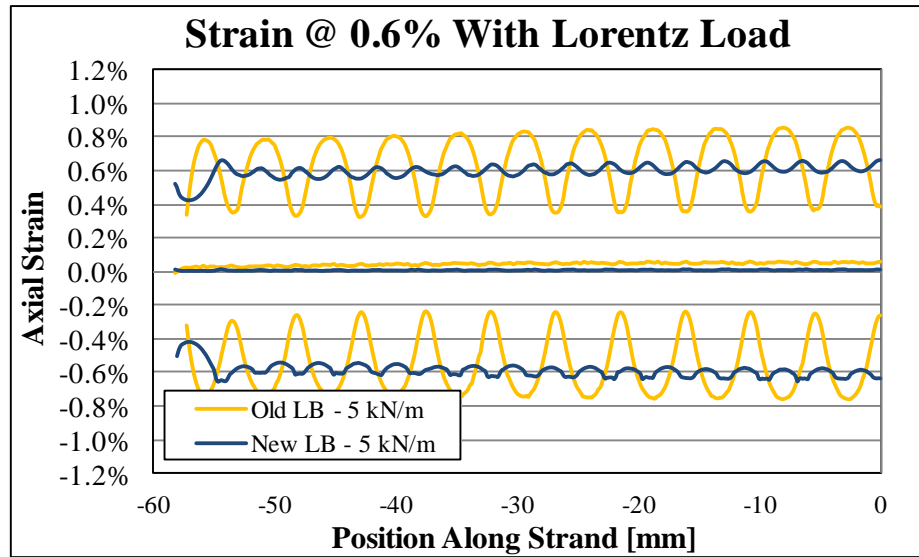
Figure 5.12 – Longitudinal strain improvement of new low bending sample holder.

The results shown above also indicated another important characteristic of the new low bending sample holder. That improvement was a reduction in the tensile strain experienced at the center of the sample. This indicates that the new sample holder reduces the neutral axis shift in the strand. The root cause of this shift was the reduction in warping which was accomplished through the greater rib width that was implemented in the new sample holder design.

In addition to minimizing the warping in the low bending sample holder when bent, the wider support ribs also helped lessen the Lorentz load tiling effect at zero bending. This is most clearly shown in Figure 5.13 which plots the deformed shape of both the new and old low bending sample holders. The deformations are for zero bending with an applied load of 5 kN/m. The max deformation seen at the middle of the sample holders shows a noticeable reduction in deformation for the

103

new sample holder design. This indicates that the additional width of the new low bending sample holder improves its strength and rigidity which minimizes the effect of the electromagnetic Lorentz load.
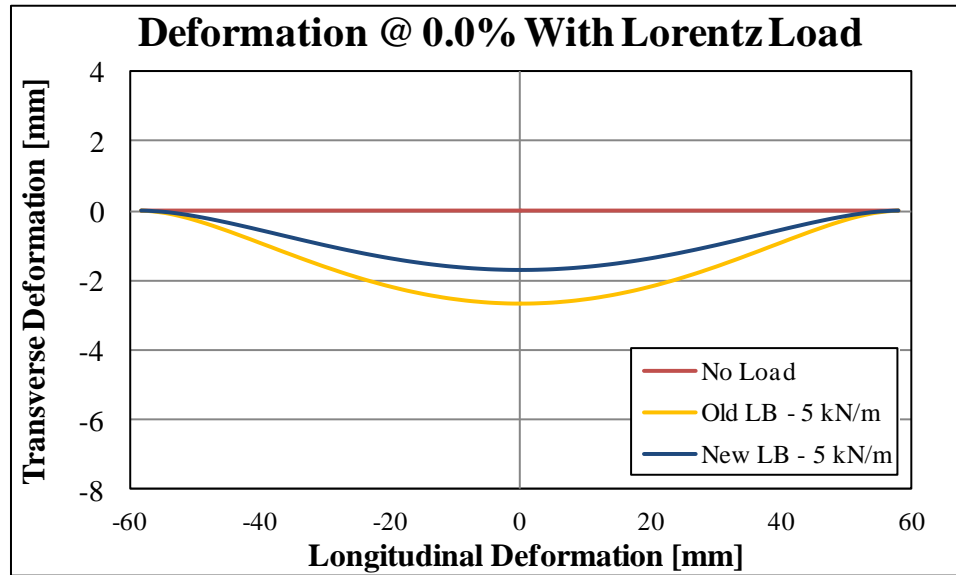
Figure 5.13 – Deformed shape improvement of new low bending sample holder.

To quantify the true effect of these strain fluctuations on the pure bending state of the superconducting strand, a root-mean-square error was calculated for the strain on the outer surfaces of the sample. This error was calculated independently for the outer and inner surfaces and then was averaged to combine the contribution of each surface. This root-mean-square error was calculated using the FEA simulation results over the 50 mm short voltage tap region in the middle of the strand. The deviation from the pure bending state was quantified for both the old and new designs and is presented in Figure 5.14.

These results are calculated for a radially inward Lorentz load only. Similar to the above plots, the orange curves represent the old sample holders while the dark

blue curves represent the new sample holders. The dashed curves indicate the low

bending sample holders and the solid lines indicate the high bending sample

holders. The red line represents an acceptable error threshold for the samples.
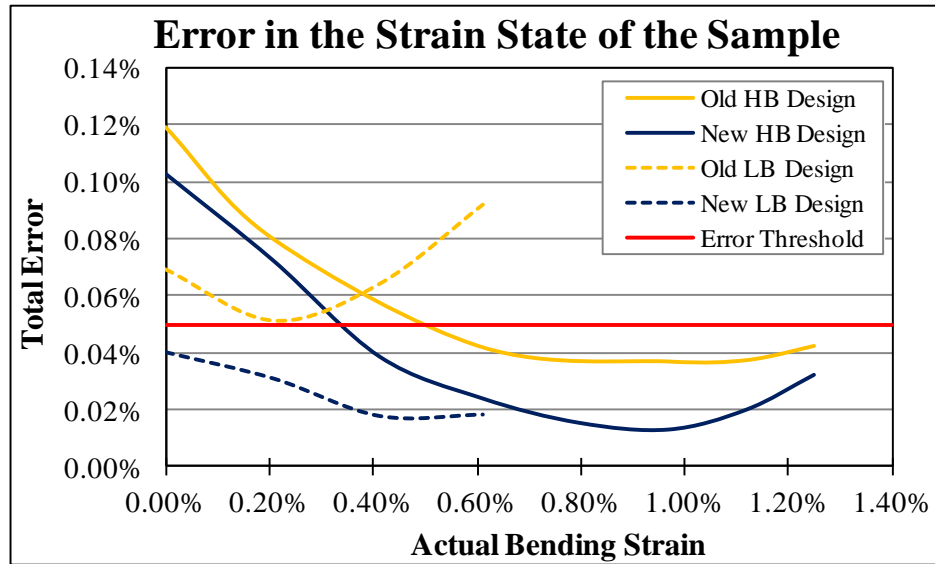
Figure 5.14 – Total error in the strain state of the sample.

The error or deviation plotted above is a combination of three different effects.

The first effect is the axial strain fluctuations that the strand experiences during

loading. These fluctuations cause a deviation from a uniform pure bending strain

distribution. The second effect is the Lorentz load tilting or deformation of the

sample holder at low bending. This tilting or deformation causes the strand to

shift putting it into additional compressive or tensile strain which adds error to the

pure bending state. The last effect that causes error is the deviation of the

deformed shape of the sample holder from that of a perfect circle.

The different effects mentioned above combine to create three distinct error

regimes over the entire bending range, as seen in Figure 5.14. The error from the

axial strain fluctuations is experienced throughout the entire bending range and is

the sole contributor to the error in second regime or bending strains between 0.5% and 0.9%. For the sample holders without channel walls, this error is relatively constant at all bending levels; however, for the old low bending sample holder with channel walls the error increases steeply with applied bending. This behavior can be seen clearly in the orange dashed line in Figure 5.14.

This fluctuation error is added to the Lorentz load tilting error at low bending creating the first error regime over the range of 0.0% to 0.5% strain. In this regime, the Lorentz load tilting effect continues to get worse as the bending strain is lowered, which causes the higher error at low bending. At very high bending, the fluctuation error gets combined with the deformed shape error creating regime 3 which covers the bending range of 0.9 to 1.25%. As identified previously the deviation of the deformed shape gets worse as bending is increased above 1.0% which leads to the increase in error over this regime.

The main findings from Figure 5.14 are that the new sample holder designs clearly reduce the error of the samples below the chosen threshold for their designed bending ranges. The new high bending sample holder with the optimized ribs showed an error improvement over the entire bending range and saw the most error reduction in the second regime. The new low bending sample holder clearly reduce the Lorentz load tilting error at very low bending strains and greatly reduced large the axial strain fluctuation error that the old low bending sample holder experienced at 0.6% strain.

6.0 Experimentation and Results

For this research, Nb_3Sn superconducting strands manufactured by the internal-tin and the bronze-route process were tested. The internal-tin type strands were supplied by Oxford Superconducting Technology. The bronze-route strands were manufactured by Hitachi Cable, Ltd. In the succeeding sections these samples will be referred to simply as Oxford (OST) and Hitachi (HIT). Manufacturer's specifications for these two wire types are presented below in Table 2.

Table 2 – Nb_3Sn wire manufacturer specifications

Wire		Hitachi	Oxford
Type		Bronze-route	Internal-tin
Diameter	(mm)	0.817 - 0.823	0.817 - 0.823
Cr plating	(µm)	2.0 (+0, -1)	2.0 (+0, -1)

Nb3Sn Filaments		Hitachi	Oxford
Number		11077	---
Diameter	(µm)	3.0 ± 0.2	5 ∼ 6
Twist Pitch	(mm)	15 ± 2	15 ± 2
Diffusive Barrier		Nb	Ta

Performance		Hitachi	Oxford
Ic @ 4.2 K & 12.0 T	(A)	220 - 250	275
N-value @ 12.0 T		35 - 45	28

Stabilizer		Hitachi	Oxford
Type		External	External
Material		OFC	OFC
Cu-Fraction	(%)	50 ± 5	52 ± 5
Cu-Ratio		1.0 ± 0.1	1.08 ± 0.1

The experiments were conducted at the National High Magnetic Field Laboratory in Tallahassee, Florida. The samples were tested in the 20 T 195 mm warm bore Bitter resistive magnet in cell 4 of this facility. The Nb_3Sn strands will be tested up to a maximum setting strain of 1.4% bending using the two new sample holder designs. The pure bending device will test 2 sample holders simultaneously. Each sample holder will contain 2 samples of each type wire, OST and HIT. Experimental preparation and testing procedures will be outlined in detail in the following sections. The critical current results from the experiments will be presented along with results of empirical modeling that was done.

6.1 Experimental Preparation

6.1.1 Sample Heat Treatment

As mentioned above, Nb_3Sn strands do not become superconductive until they have been heat treated to diffuse the individual constituents of the wire together. However, after heat treatment the Nb_3Sn filaments become very brittle and sensitive to strain. For this reason the Nb_3Sn strands must first be put into position on the sample holder before the heat treatment process, when the strands are more ductile and tolerant of handling. This will minimize any potential damage or degradation that may occur from handling the wire after it has been heat treated.

Before the strands can be mounted to the sample holder assembly, the current terminals must be attached to the ends of the sample holder. Figure 6.1 shows one current terminal designed by Mallon mounted to the end of the sample holder [16]. Once the current terminals are attached to the sample holder the un-reacted Nb_3Sn are strands placed into the sample holder channel and into the U-shaped current terminal groove.
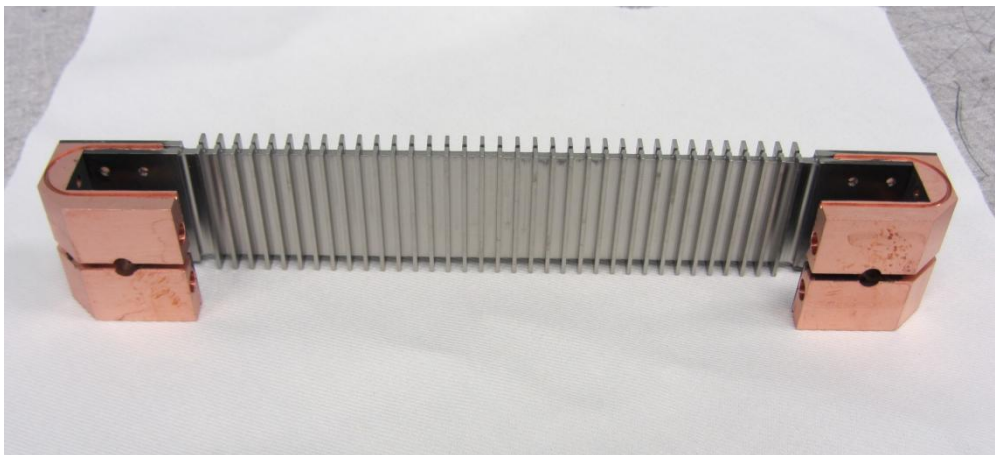
Figure 6.1 – Image of the sample holder and current terminals.

To promote consistent diffusion within the Nb_3Sn strands during the heat treatment and to minimize any tin leakage from the strand ends, one continuous length of wire is placed into both samples holders at once. The assembled wire and sample holders are shown in Figure 6.2 along with additional components used to hold the wire in place during the heat treatment. Once the heat treatment process was complete the wire was cut back to the ends of the current terminals creating individual Nb_3Sn samples.
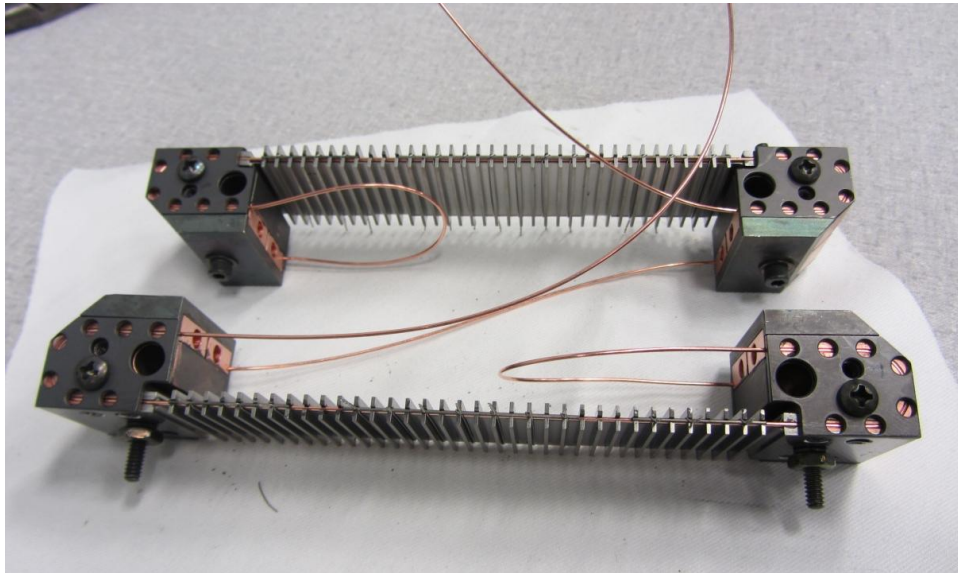
Figure 6.2 – Sample holder prior to heat treatment showing one continuous length of wire.

The Nb_3Sn wires were heat treated using the ITER recommended schedule which heats the wire in stages for nearly 500 hours. Figure 6.3 below depicts the entire heat treatment process indicating the temperature and length of time at each stage. The heat treatment was done using a high temperature programmable Argon gas furnace. The sample holders were bundled together and carefully positioned in the center of the furnace to help ensure uniform heating. This nearly month-long heat treatment was done shortly before departing for the NHMFL in Tallahassee, FL.
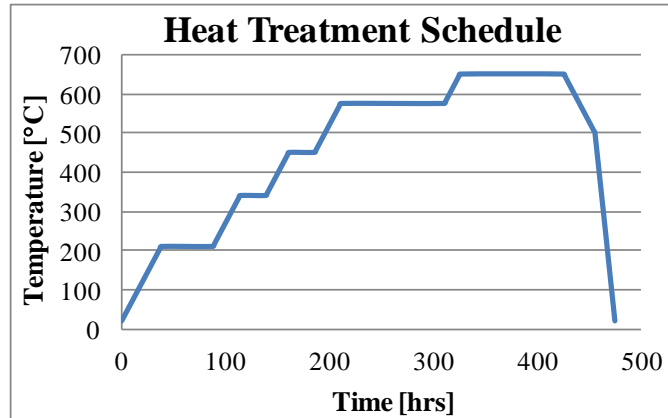
Figure 6.3 – ITER recommended heat treatment schedule for Nb$_3$Sn wire.

6.1.2 Sample Soldering and Voltage Taps

Post heat treatment the wires must be soldered to the current terminals. This creates a solid electrical connect between the current terminals and the sample allowing for good current transfer and current development within the strand. Before applying solder, flux must be used to clean all components being joined. After flux, the solder can be applied directly to the Nb$_3$Sn sample located in the U-shaped groove of the current terminal.

Two cartridge heaters were used to heat the current terminal. These heaters facilitate the melting and coverage of the solder allowing it to fill all voids creating a solid electrical contact. The cartridge heaters can be seen in Figure 6.4. Electricity is applied to the cartridge heaters via the wires at the top of the photo.

This process requires steady and skillful use of the soldering iron to ensure the sample remains in place while the soldering is occurring. Care must also be taken to not locally overheat the strand. This would essentially modify the heat treatment of the wire locally, which may change its superconducting behavior.

Figure 6.4 – Setup for soldering samples to current terminals.

After the samples have been secured to the current terminals, the current leads must be attached. The leads are soldered into the current terminals in a similar fashion as described above. While the soldering is taking place, the lead is moved in and out using a twisting motion to allow the solder to penetrate all the way into the hole. This method ensures a good electrical connection is made between the current lead and terminal.

The critical current of the strand is determined by measuring the voltage across the sample. This voltage is recorded through two sets of voltage taps; long and short. Figure 6.5 below shows the two sets of taps soldered to the top Nb_3Sn sample. The short voltage taps cover a 50 mm span in the exact middle of the sample and are indicated by the white and green wires. The long voltage taps cover the entire length of the sample and are shown as the orange and black wires. The short voltage taps are the primary set of taps because they cover the middle region of the sample. In the middle of the sample the current is fully developed within the superconducting filaments and the bending curvature is more uniform.

The long voltage taps are used as a secondary set of taps in case a primary voltage

tap is damaged or physically breaks free from the sample.
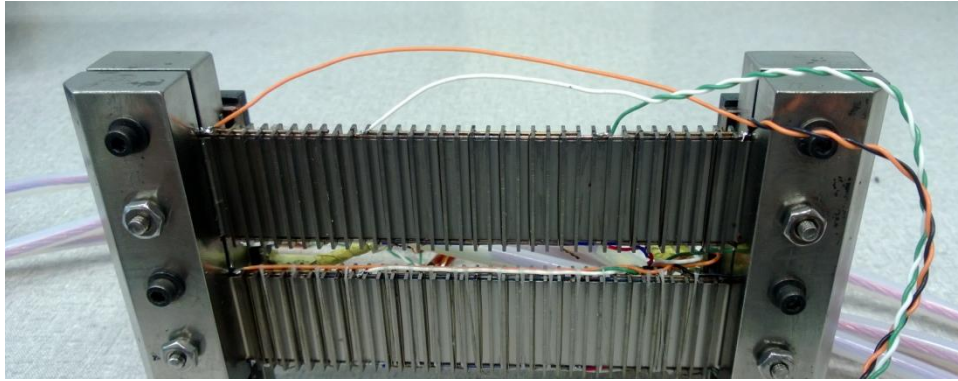
Figure 6.5 – Long and short voltage tap wires soldered to Nb₃Sn sample.

The voltage taps shown above are soldered directly to the surface of the Nb$_3$Sn

strands. The strand surface is first slightly roughened, which will facilitate a better

bond with the solder. Next the sample is locally heated using a soldering iron as

shown in Figure 6.6. This warms the sample enough to melt the solder. While the

solder is still liquid, the voltage taps are carefully joined onto the strand.
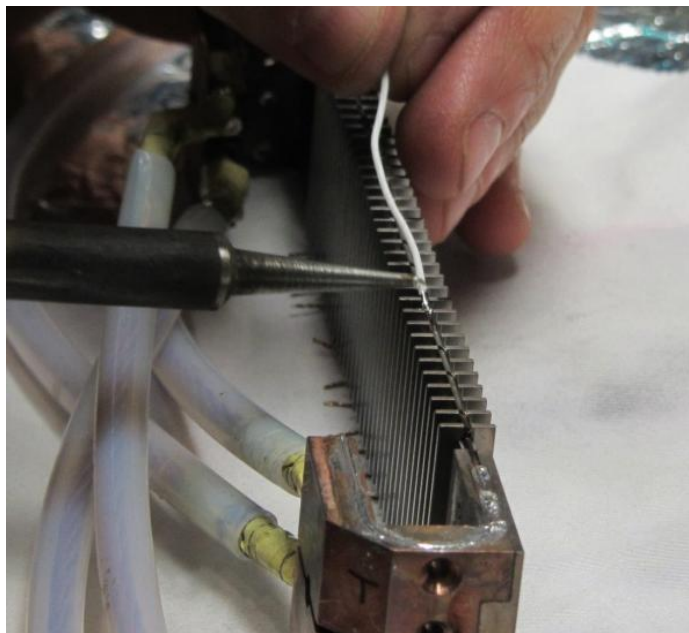
Figure 6.6 – Soldering of voltage taps on the superconducting strands.

Much care must be taken during this process to ensure both a good electrical connection and a strong physical connection between the voltage tap and the sample. Once all voltage taps have been soldered to the sample the tap wires are tied down to the sample holder and bundled together to prevent any accidental damage during experimentation.

6.1.3   Sample Mounting Assembly

With the sample holders already equipped with the current terminals, current leads, Nb_3Sn samples and the voltage taps; they are ready to be mounted to the bending device. Before mounting directly to the gear box, the sample mounting assembly must first be put together. The sample mounting assembly consists of 4 main components: the sample holders, the current terminators, the vertical supports and the torque arms.

First, both fully prepped sample holders are mounted onto the vertical supports. One vertical support is first placed on the backside of the sample holders and is slid into place in-between the U-shape current terminals. The other vertical support is placed on the front side of the sample holders. These vertical supports are then bolted together clamping the two sample holders in place. This same process is then done for the opposite side. The resulting sub-assembly is shown below in Figure 6.7. This figure shows the stacked orientation of the two sample holders. It also indicates the colorful bundle of voltage taps at the top left of the photo. Lastly, running horizontally at the bottom of the image are the current leads which supply power to the current terminals.
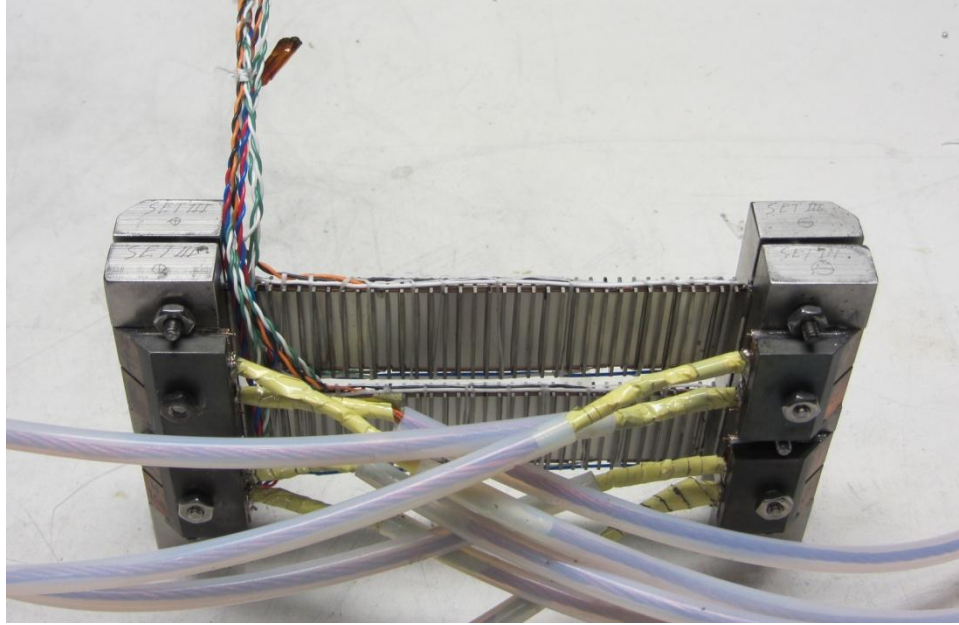
Figure 6.7 – Fully prepared sample holders mounted to the vertical supports.

This sub-assembly is then connected to the two torque arms. The torque arms are first mounted in the correct orientation on the torque shafts seen in Figure 6.8. The sample holder sub-assembly is mounted on the device by securing the vertical supports onto the torque arms using 8 pins. The entire bending mechanism fully assembled is shown in the image on the right of Figure 6.8.
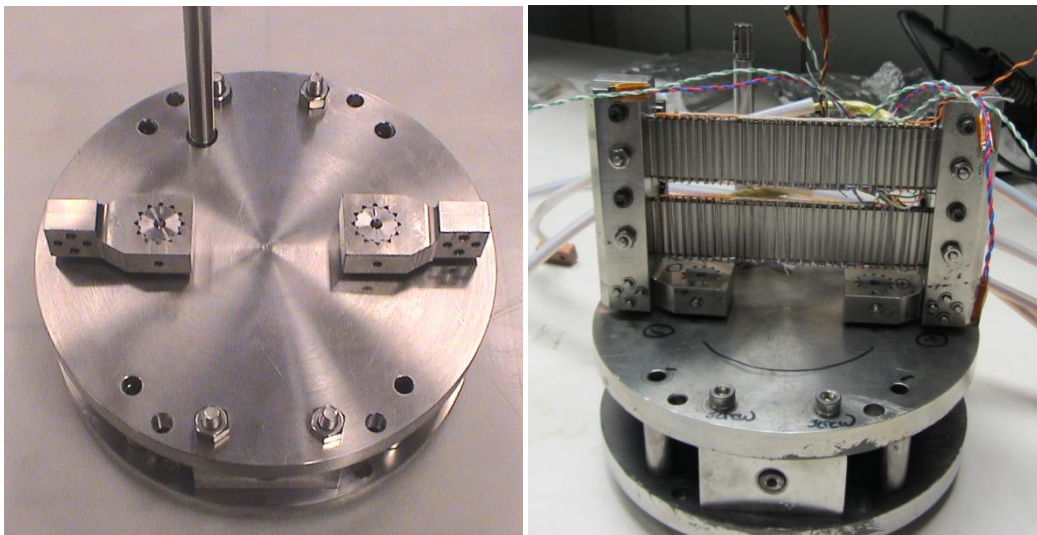
Figure 6.8 – Before and after images of sample mounting assembly attached to device.

114

6.1.4   Gear Box Preparation

Before the sample mounting assembly is attached to the gear box, the gear train

must first be prepped for the experiments. To prepare the gear train, all

components must first be disassembled and thoroughly cleaned as seen below in

Figure 6.9. The cleaned components were then coated with a thin film of graphite

which acts as a dry lubricant. This graphite coating is used to reduce the friction

and wear between moving components. This is an important step as galling has

occurred within the gear box in previous bending tests [16]. The coated gear train

components are then re-assembled into the gear box and are checked for

satisfactory rotating performance.
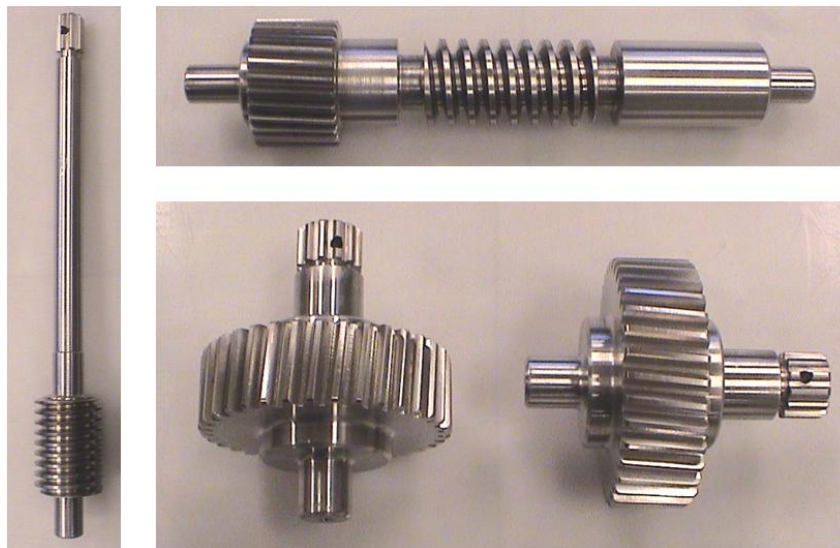
Figure 6.9 – Gear train components cleaned and separated before assembly.

6.1.5   Probe Preparation

The first step in preparing the probe was to attach the DC motor and encoder. This

motor and encoder system will be used to accurately control the rotation of the

input shaft which applies rotation to the bending device. The motor is mounted to

the stainless steel plate at the top of the probe and is then coupled to the input shaft that runs the length of the probe. The encoder was also mounted on this drive shaft. At this stage the DC motor and encoder were tested to ensure proper functionality. A picture of the DC motor mounted on a stainless steel plate at the top of the probe is shown below in Figure 6.10.
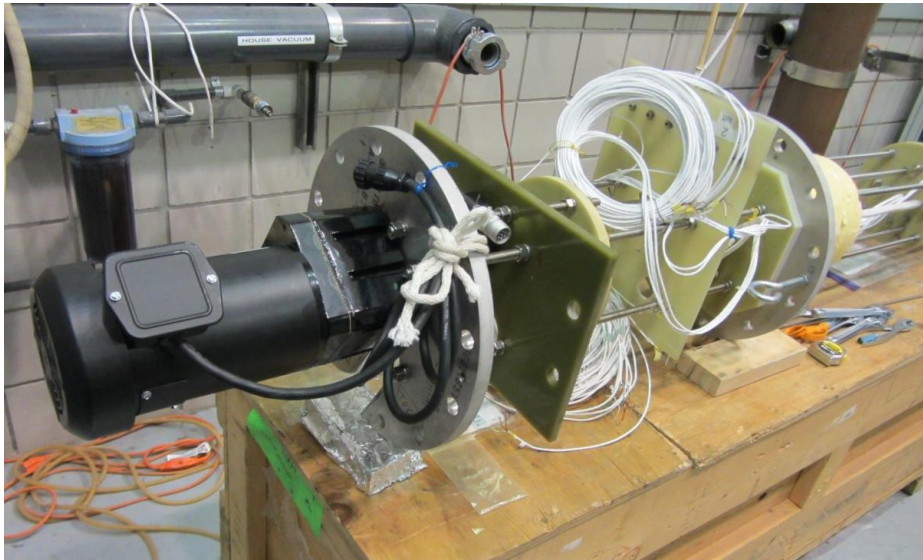
Figure 6.10 – DC motor mounted at the top of the probe.

With the motor mounted and coupled to the input shaft, the pure bending device is attached to the bottom of the probe. The pure bending device is held onto the probe using 4 threaded rods. The device is slid onto these rods and then is locked into place with a series of nuts. The threaded shafts are used to allow the bending device to be positioned at the appropriate vertical distance ensuring it will be in the middle of the magnet field during testing.

Once the device is mounted in the appropriate position the input shaft on the gear box is coupled to the input shaft on the probe. Therefore, the DC motor will rotate the input shaft at the top of the probe which will directly apply rotation to the gear

box. This in turn will rotate the torque arms applying bending to the sample.

In addition to mounting the bending device, the voltage taps and current leads must also be connected to the infrastructure on the probe. The probe has current leads and voltage tap wires that run from the bottom to the top of the probe, where they can be connected to the power source and nano-voltmeters. The voltage taps were connected using simple pin-type electrical connections. The copper leads were connected by bolting together small copper blocks that were soldered to the ends of the current leads on both the probe and the bending device. The pure bending device mounted and wired to the probe can be seen in Figure 6.11
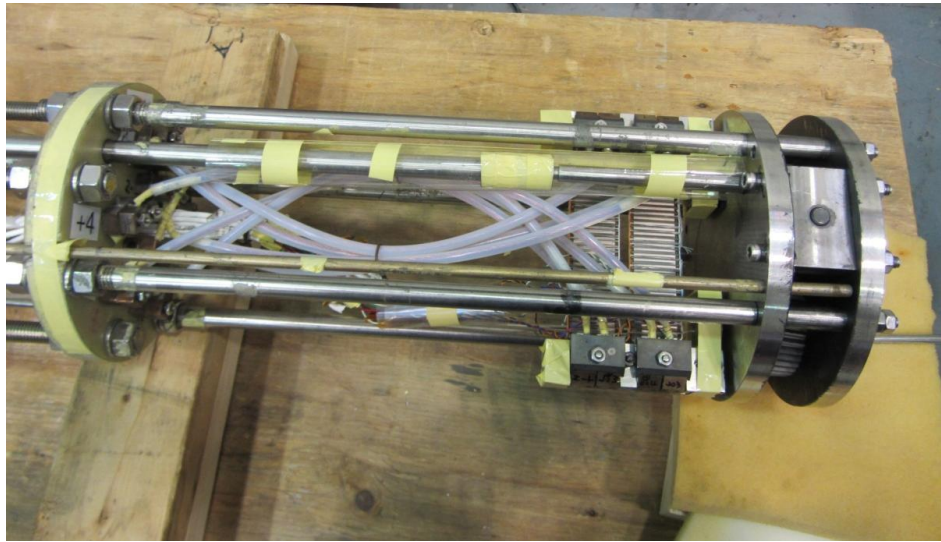
Figure 6.11 – Pure bending device mounted at the bottom of the probe.

Lastly, the probe was equipped with two liquid helium level sensors; a low and a high. These sensors allow the user to determine the height of the liquid helium within the cryostat. This will ensure a proper level of helium during testing so that the sample always remains at 4.2 K. Before the probe is put into the cryostat, the connectivity of all sensors is checked and then it is wrapped with Mylar sheets.

This cocoons all wires and equipment helping minimize damaged that may occur while the probe is being placed within the cryostat, and it also provides electric insulation between the sample and dewar.

6.1.6   Instrumentation Preparation

With the probe fully assembled and ready for experiments, the remaining testing equipment and measurement devices must be set up. First the current leads on the top of the probe are connected to individual terminals on the terminal board. A 1,500 amp DC current power supply, provided by the NHMFL, is then connected to the terminal board. Which terminals the current supply is connected to will determine which Nb_3Sn samples are being tested. This terminal board also allows for current reversal testing of the samples by switching the power supply leads.

Instrumentation wires for the helium level sensors and voltage taps were wired to a 32-pin connector board. This board organized all the instrumentation wires, making it quick and easy to connect to the appropriate leads for a certain sample. The NHMFL supplied us with three Keithley model 2182 A digital nano-voltmeters which were used to measure the voltages from the two sets of taps and the input current of the sample. The data from these voltmeters was then sent through the data acquisition system of the magnet cell's computer where it was displayed and recorded using a custom designed LabView program developed by the NHMFL.

The magnet cell's computer was also used to control the magnet field, ramping rate and field direction of the resistive magnet. The magnet is initially warmed up and tested by the facility operators before controls are given to the users of the cell.

Lastly the DC motor power supply and encoder were connected to a specially

designed motor controller. The controller is programmable and will automatically

turn on and off the motor for a specific inputted amount of rotations chosen by the

user. This allowed us to easily increase and decrease the bending strain incrementally.

The motor controller also records and displays the total number of rotations which

allows us to determine the amount of bending being applied to the sample holder.

6.2 Critical Current Experiments

6.2.1 Testing Setup

Before experimentation begins, the cryostat used for testing is lowered into the

magnet bore. This process is depicted in the two images shown in Figure 6.12.

The cryostat is designed to keep the test device at a constant cryogenic

temperature during experiments.

Figure 6.12 – Cryostat (right) being lowered into the magnet bore shown on the left.

The cryostat used at the NHMFL has a two chamber design, inner and outer, as

seen previously in Figure 2.1. The outer chamber is kept full of liquid nitrogen to

maintain the cryostat at 77 K which reduces the amount of liquid helium needed

to cool the probe and bending device to 4.2 K. It also minimizes the thermal

gradients within the cryostat which helps to eliminate the amount of liquid helium

boil off during the experiments. The inner cryostat chamber is filled with liquid

helium during the experiments to keep the test device at 4.2 K. The appropriate

amount of liquid helium is maintained using the liquid level sensors installed on

the probe. A picture of both cryogenic liquids being transferred to the cryostat is

shown in Figure 6.13. The smaller liquid nitrogen dewar is shown in the forefront

of the image and the larger liquid helium dewar is in the background.

Figure 6.13 – Cryostat being filled with liquid nitrogen and liquid helium.

For each experiment the entire probe assembly with the pure bending device is

raised by a crane and lowered into the cryostat. This process is shown in Figure

6.14 and requires caution to ensure no damage is done to the bending mechanism, probe or instrumentation. Once the probe is mounted within the cryostat and magnet bore, the instrumentation wires and current leads are connected, as described above.

Figure 6.14 – Lowering of the probe into the cryostat.

6.2.2 Critical Current Measurements

The pure bending device was designed for strain characterization tests of Nb_3Sn superconducting strands under bending loads. At the NHMFL two days of tests were conducted to characterize the Nb_3Sn strands covering the entire designed range of bending strains up to 1.4%. On the first day of testing the new low bending sample holder was used to recorded critical current results up to a maximum strain of 0.7%. On the second day of testing the new high bending sample holder was used to characterize the superconducting samples over the remaining bending strains up to 1.4%. The high bending sample holder was also used for critical current test below 0.6%. These tests at low bending strains were only conducted after the high bending range above 0.6% was covered, in case the

sample holder was damaged by the larger deformation that was expected at these low bending strains. In addition to simply characterizing the Nb_3Sn strands over the entire bending range, both sample holders were also used to conduct reversed current and cycling effect tests.

The critical current tests were conducted by slowly increasing the current in the one sample while recording the voltage across it using the two sets of voltage taps. The NHMFL LabView program was used to record and plot the voltage signals as a function of applied current in real-time, as seen in Figure 6.15. The red curve represents the short voltage tap and the blue curve represents the long voltage tap. During experiments this real-time plot is used to determine the transition of the superconducting strand into a normal resistive state.
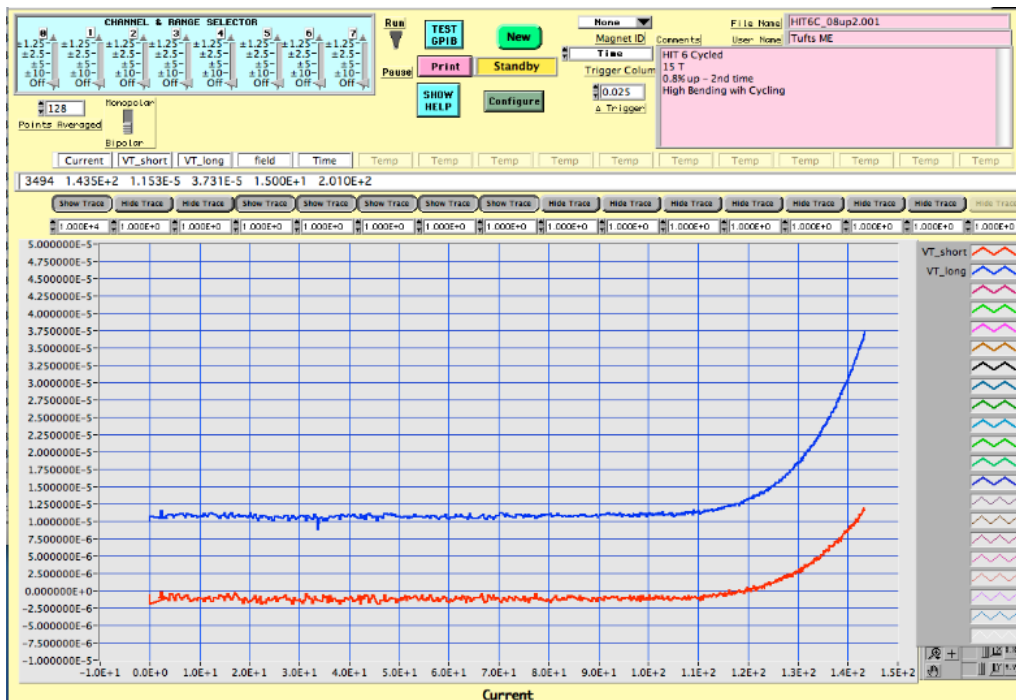
Figure 6.15 – Real-time plot of short (red) and long (blue) voltage tap data.

The results shown in Figure 6.15 clearly depict the general behavior of a

superconductor wire. The measured voltage across the sample initially remains unchanged as the current is increased until it begins to transition to a resistive state. At this point the measured voltage exponentially begins to increase. The uniform flat region nicely represents the superconductive state of the sample and the exponential increase at the end clearly indicates a transition of the sample.

Once enough data has been collected to characterize the transition, the current is removed from the sample before the wire quenches. A quench is when the superconductor suddenly and rapidly becomes resistive. Occasionally a superconductor will quench before experiencing its transition. In this case, no critical current data can be determined from the test.

The low bending sample holder positioned on top contained the Hitachi samples, referred to as HIT 1 and HIT 2. The bottom sample holder carried the Oxford samples, referred to as OST 1 and OST2. Similarly the Hitachi strands were mounted to the top sample holder for high bending while the Oxford samples were mounted on the bottom sample holder. These samples are referred to as HIT 3 and 4 and OST 3 and 4 respectively.

Each critical current test was conducted on only one sample at a time. For each test, the top most sample was tested first, followed by the remaining three. The strain in the following sections is the setting strain so that comparison with previous tests can be done in Section 6.3.4.

Day 1 (Low Bending Sample Holder)
The first thing done on each day of experiments is to characterize the field

dependence of the Nb_3Sn wires at zero bending strain. This establishes a baseline for the critical current performance of the samples. This is done because the performance of a superconducting strand is highly dependent on its heat treatment and handling and therefore it is important to benchmark its performance before the current degradation experiments are conducted. The magnetic field dependence of the Nb_3Sn samples was tested at 12, 13, 14 and 15 T. This range was chosen based on expected operating fields for the ITER project.

Once the field dependent critical current data was gathered between 12 T and 15 T, the critical current characterization under bending began. The motor controller was used to rotate the drive shaft 21.74 turns correlating to a strain of 0.1% on outer surface of the Nb_3Sn strands. The critical current results for each sample were then measured and recorded one sample at a time starting with HIT 1. This process continued at 0.1% intervals up to a bending strain of 0.5%. At this point the bending was reduced to 0.3% strain and then to a state of zero bending. This was done to determine any hysteresis effects. After testing again at zero bending, the sample was again bent to an applied strain of 0.5%. After this the strain was increased to 0.6%. The strain was then reduced again to 0.3% before being increased to its maximum bending strain of 0.7%.

After measuring the current at its maximum bending the strain was reduced back to zero, taking measurements at 0.6%, 0.5%, 0.3% and 0.0%. The reversed current effects were then tested at zero bending. Succeeding this, the sample was bent directly to a strain of 0.6% measured and then cycled back to zero bending.

Cycling tests were then conducted, which cycled the sample up to a strain of 0.5% and then back to zero 5 times in a row. On the last cycle the critical current results were recorded at 0.5% and then again at 0.0%. At this point more reversed current tests were conducted. Reversed current results were collected for the following bending states: 0.0%, 0.3%, 0.5%, 0.4%, 0.2% and lastly 0.1%. As always, the bending was returned to zero before removing the probe from the cryostat. All bending measurements described above are summarized in the Table 3.

Table 3 – Low bending test procedure (Day 1).

Test #	% Strain	Notes	Test #	% Strain	Notes	Test #	% Strain	Notes
1	0.0	---	10	0.6	-	19	0.0	–
2	0.1	-	11	0.3	–	20	0.5	Cycled 5x
3	0.2	-	12	0.7	-	21	0.0	Cycled 5x
4	0.3	-	13	0.6	–	22	0.0	Reverse
5	0.4	-	14	0.5	–	23	0.3	Reverse
6	0.5	-	15	0.3	–	24	0.5	Reverse
7	0.3	–	16	0.0	–	25	0.4	Reverse
8	0.0	–	17	0.0	Reverse	26	0.2	Reverse
9	0.5	-	18	0.6	-	27	0.1	Reverse

Day 2 (High Bending Sample Holder)

As done for the low bending sample holder, the field dependence of the Nb_3Sn wires was first characterized. Due to uncertainty about the strength of the high bending sample holder at zero bending, the field dependent data was recorded for 0.6% bending strain. Getting results for the samples within the sample holder's designed operating range of 0.6% to 1.4% was of primary importance, which is why we did not risk first getting field dependent results at zero bending.

Once the field dependent critical current data was gathered at 0.6% setting strain, the device was bent further to characterize the rest of its design range. Starting at

0.6%, the motor controller was used to rotate the drive shaft incrementally, increasing the bending strain by 0.1% every increment. Critical current results were recorded for each increment up to 1.0% setting strain. At this point the strain was then incremented by 0.2% up to the maximum bending strain of 1.4%. No mid-range cycling up and down was used due to magnet time limitations. From the maximum bending state, the strain was then incrementally decreased all the way back down to 0.0% strain. On the way, the critical current results were recorded in steps of 0.2% strain.

From the zero bending state the reversed current behavior of the wire was characterized. Reversed current tests were conducted up to a maximum strain of 1.4%. Reversed current results were taken at 0.2% increments. Following this, cycling tests were run starting from the maximum bending state. First, the strain was cycled down to zero bending and back up to 1.4% strain. Critical current results were then recorded for this first cycle.

Next the sample was cycled two times returning back to the maximum bending state. Critical current results were then recorded for this third cycle. The sample was then cycled down to zero and back up to 1.4% one more time. Critical current results were recorded at the maximum bending after the 4 cycle. The sample was then brought back down to zero bending in 0.2% increments, recording the critical current results along the way.

All previously mentioned tests were summarized together in Table 4. This table presents a detailed list of the measurements that were taken for day 2 of testing.

Table 4 – High bending test procedure (Day 2).

Test #	% Strain	Notes	Test #	% Strain	Notes	Test #	% Strain	Notes
1	0.6	---	12	0.4	-	23	1.4	---
2	0.7	-	13	0.2	-	24	1.4	Cycled 1X
3	0.8	-	14	0	-	25	1.4	Cycled 3X
4	0.9	-	15	0	Reverse	26	1.4	Cycled 4X
5	1.0	-	16	0.2	Reverse	27	1.2	Cycled 4X
6	1.2	-	17	0.4	Reverse	28	1.0	Cycled 4X
7	1.4	-	18	0.6	Reverse	29	0.8	Cycled 4X
8	1.2	-	19	0.8	Reverse	30	0.6	Cycled 4X
9	1.0	-	20	1.0	Reverse	31	0.4	Cycled 4X
10	0.8	-	21	1.2	Reverse	32	0.2	Cycled 4X
11	0.6	-	22	1.4	Reverse	33	0.0	Cycled 4X

6.2.3 Sample Characterization

The goal of this research has been to characterize the critical current behavior of Nb_3Sn strands under pure bending loads. The critical current is characterized by the superconducting strand's transition back to a normal resistive state. As the current is increased in the experiments, the transition is denoted when the voltage in the sample begins to exponentially increase from a previously constant state. Since the transition of the superconductor happens over a range of currents, the critical current value is determined from a standardized criterion. This criterion is referred to as the critical electric field value (E_c), which is equal to the voltage across the sample divided by the distance between the taps. The current that corresponds to this value is the critical current, I_c. The ITER electric field criterion for critical current tests is 10 µV/m, however for shorter samples a larger criterion like 100 µV/m and 200 µV/m may be necessary to use due to the voltage resolution limitation caused by the high noise to signal ratio.

In addition to determining the critical current, the characterization tests can be

used to find the n-value of the sample. The n-value is an exponential parameter that relates the electric field (E) in the sample to its current density (J). The exponential relationship is: $E/E_c = (J/J_c)^n$. The n-value will therefore describe the exponential transition of the strand from the superconducting state to the normal resistive state. A large n-value indicates a rapid transition that occurs over a small current range and a small n-value signifies a slower transition over a wider range of current. The n-vale is a function of the testing conditions, the design of the test sample, and the heat treatment used.

6.3 Critical Current Results

6.3.1 Data Analysis

As mentioned above, voltage tap data was recorded for both voltage tap lengths, short and long. For both days of testing the short voltage tap was undamaged during the experiments. Therefore, the short voltage tap results were used exclusively for the critical current analysis that followed. The short voltage taps were the primary voltage taps due to the current distribution within the sample and uniformity of sample holder deformation.

For both days of testing the voltage tap signals had minimal noise for the most part. This made it relatively easy to determine the approximate critical current value directly from the real-time data. Although the voltage tap signals were fairly clean, for a more detailed analysis of the critical current results, the recorded voltage tap data would have to be cleaned up. First, a five point running average

technique was applied to the data to reduce the overall effect of noise. Next, the data was shifted the appropriate amount to eliminate the voltage offset in the results. The offset refers to the offset of the voltage from zero while the sample is in a superconducting state. Figure 6.16 below shows an example of voltage tap data that has been averaged and shifted and is ready for analysis.

The horizontal dashed lines mark the three electric field criteria used to determine critical current of a superconducting strand; 10 µV/m, 100 µV/m and 200 µV/m respectively. The criteria represent the electric field in the sample being tested; therefore, it needs to be converted into a voltage by multiplying it by the length of the voltage tap. The nominal length of the short voltage tap is 50 mm (1.969 inches) which results in the following criteria; 0.5 µV, 5 µV, and 10 µV. These nominal criteria were used to quickly approximate critical currents during experiments; however, the actual voltage tap length was used to determine the exact criteria for the analysis.
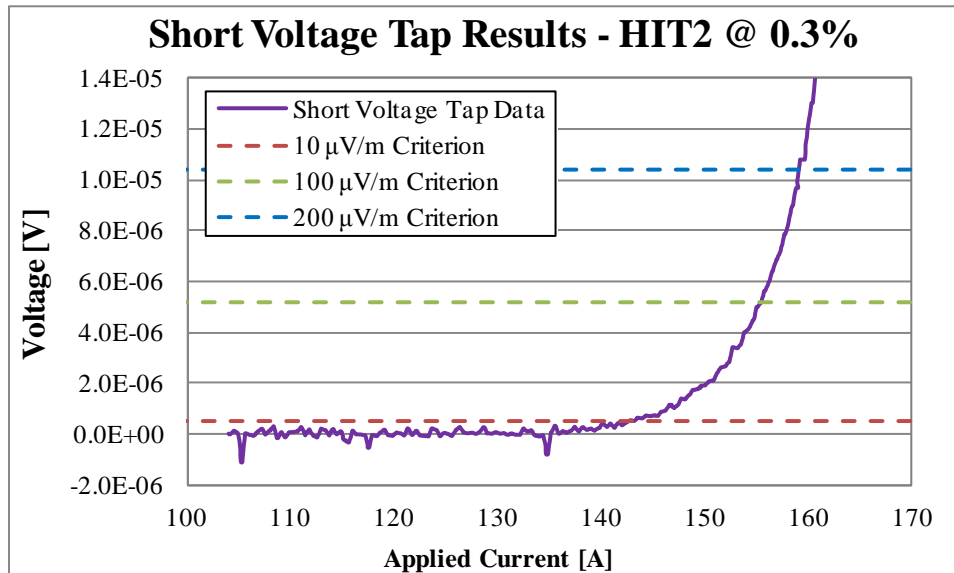
Figure 6.16 – Example of short voltage tap data after being conditioned and shifted.

129

To determine the exact critical current and n-value for the sample, the conditioned voltage tap data was converted to a log-log plot. On a logarithmic plot the voltage results can be fit by a linear function. The slope of the best linear fit is equal to the n-value. The n-value describes the sharpness of the transition from the superconducting state to the resistive state. The critical current can then be found using the equation for the best linear fit. Whenever possible the ITER recommended 10 µV/m criterion was used to determine the critical current. The voltage tap data presented in Figure 6.16 is shown on a log-log plot in Figure 6.17. The figure shows the best linear fit to the data and its corresponding equation as well as the three electric field criteria. In this example of data, all three criteria were acceptable to use.

Short Voltage Tap Results - HIT2 @ 0.3%

Legend:
— Short Voltage Tap Data
– – 10 µV/m Criterion
– – 100 µV/m Criterion
– – 200 µV/m Criterion
— Linear (Short Voltage Tap Data)

$y = 28.667x - 156.8$
$R^2 = 0.9951$

Y-axis: **Log (Voltage)**
X-axis: **Log (Current)**
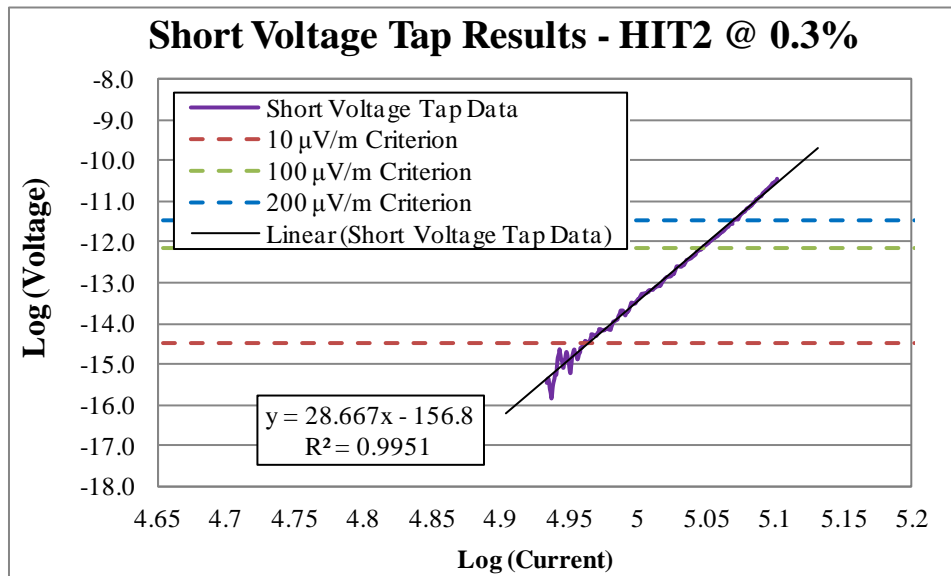
Figure 6.17 – Log-log plot of the short voltage tap data presented in Figure 6.16.

The critical current at every applied bending was determined by completing this analysis for all sets of voltage tap data. No data was analyzed for samples that quenched before beginning to transition. After the analysis was achieved for all

130

data, the critical currents results were normalized by their initial critical current determined at zero bending strain. The normalized data allows for a more direct comparison of results between the different sample types, different sample holders and different experiments. Both the critical current and n-value results are presenting in the following section.

6.3.2   Critical Current Results

For the critical current tests of Nb_3Sn strands under bending load, clean data from all of the short voltage taps was obtained. Because this clean data was obtained over all bending strains, the most data possible was collected for characterizing the samples under bending loads. The clean data also facilitated more accurate calculations of critical current in the sample. The best linear fit, which was used to identify the critical current and n-value, had a correlation of greater than 0.90 for all data sets.

The critical current results for the pure bending characterization experiments are presented in the two figures on the following page. The results presented are for tests run at 15 T and 4.2 K and for data characterized using the 100 µV/m criterion. Results for all three criteria have been found and are presented in tabular form in Appendix I. Figure 6.18 plots the critical current results for both the Hitachi and Oxford samples over the entire bending range of 0.0 to 1.25% actual strain. It should be noted that Figure 6.18 plots all collected data for each sample including the reversed current tests and cycling tests. The individual effect of these will be isolated and investigated later on.
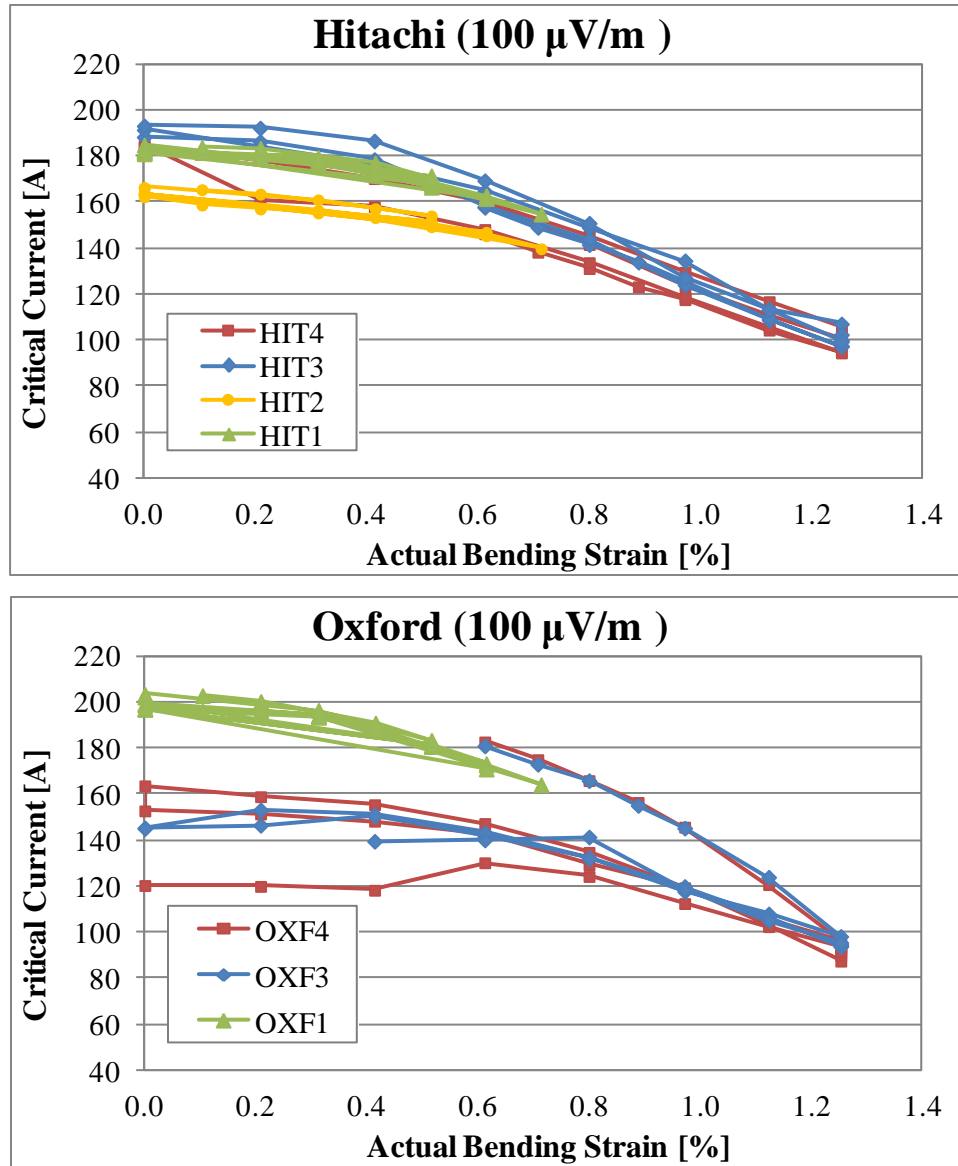
Figure 6.18 – Critical current results for Hitachi (top) and Oxford (bot).

The overall electrical behavior for both samples shows a decreasing critical current trend as bending strain is increased. The Hitachi samples showed no appreciable permanent degradation, meaning that after the bending load was removed the critical current returned to previous levels. The Oxford samples were more prone to damage and did show significant permanent degradation when the bending load was removed from its maximum strain. In addition to this, the

Oxford samples were more prone to quenching, which reduced the amount of collected data. The OST 2 sample quenched with no transition at every bending state and therefore no acceptable data was collected for that sample. The OST 1 sample also quenched frequently after the onset of the transition so some data was still recorded.

The most important finding from results presented above is the uniformity of the critical current degradation over the entire bending range. This is especially obvious for the Hitachi samples, which shows a smooth transition of critical current from the low bending sample holder to the high bending sample holder. No jump in critical current or change in slope of the degradation is seen as it was seen in King's experimental results [2]. There is a slight critical current increase between the low and high bending results for the Oxford samples, however the difference is small and the slope of the degradation is very similar. This indicates that the difference could be solely based on variations between the samples and not the strain state of the sample.

Figure 6.19 displays the normalized critical current for both wires over the full range of bending strain. The normalized results are important because they show the behavior of the current reduction as bending is increased. This provides a direct sense of the critical current degradation in the sample, which allows the behavior of the two wire types to be compared. The normalized results also make it easier to identify an exact percent reduction in critical current under bending. The behavior and degradation of both type samples is displayed in Figure 6.19.
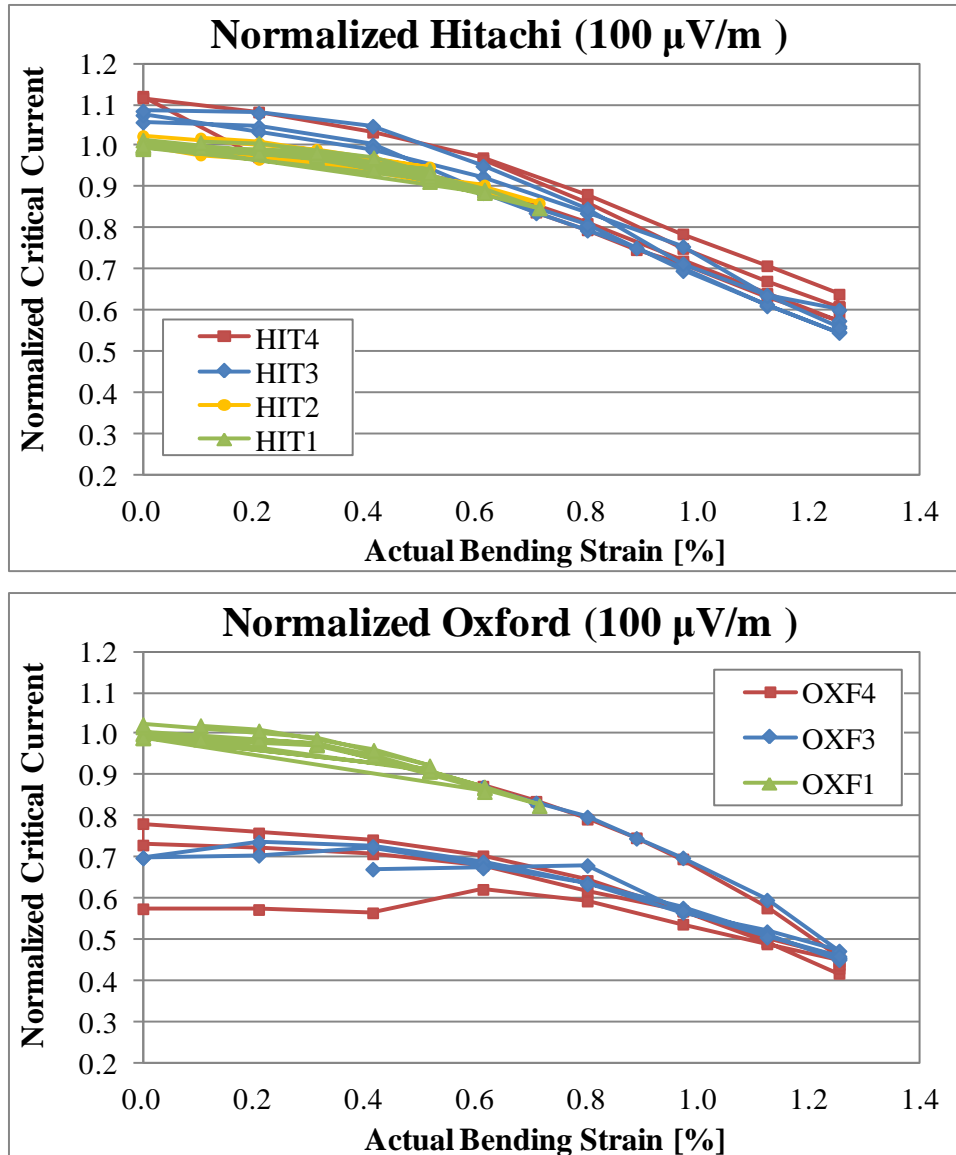
Figure 6.19 – Normalized critical current results for Hitachi (top) and Oxford (bot).

The results show that the Hitachi samples experienced a critical current reduction of between 40 and 50 percent at 1.4% bending strain, while the Oxford samples experienced slightly more reduction of between 50 and 60 percent at the same bending state. The difference between the two is that the critical current of the Hitachi samples was completely recoverable, while the Oxford samples critical current only recovered to about 80% after bending to the maximum strain. Close

inspection shows that the high bending Hitachi samples actually experienced an increase in critical current of almost 10% after being loaded up to the maximum bending. This characteristic will be discussed more in the following sections.

Overall the normalized results again show that the critical current degradation trend in the two sample holders is very similar. The normalized data makes it even more clear that for a bending strain of 0.6% and 0.7% the critical current reduction is the same for both the low and high bending sample holders. In conclusion, this uniformity in critical current behavior verifies that the design improvements made to the new sample holders have paid off. The improvements have been shown to eliminate all critical current discrepancies between the old sample holders that were discovered previously.

Low Bending Results

The critical current results from the four samples tested in the new low bending sample holder are presented in more detail below. The second Oxford sample, OST2, is not presented below because no appreciable results were recorded for this sample due to quenching. The critical current results for all low bending samples are presented in Figure 6.20. On the top is a standard plot of the calculated critical currents and on the bottom is a normalized plot of that same data. All samples were normalized to their initial zero bending critical current. The critical current results in these plots cover between 0.0 and 0.7% actual strain.

All three samples shown below have very comparable and consistent critical current behavior. Each sample has a gradual degradation in current as the bending

is increased. The critical current magnitudes for each sample are different but their degradation is similar. The similarity in the current behavior can be more clearly seen in the normalized results shown in the bottom plot. Both Hitachi samples saw around 15% reduction in critical current at 0.7% strain while the Oxford sample experienced just slightly more reduction. For both wire types the critical current was recoverable and showed no permanent degradation.
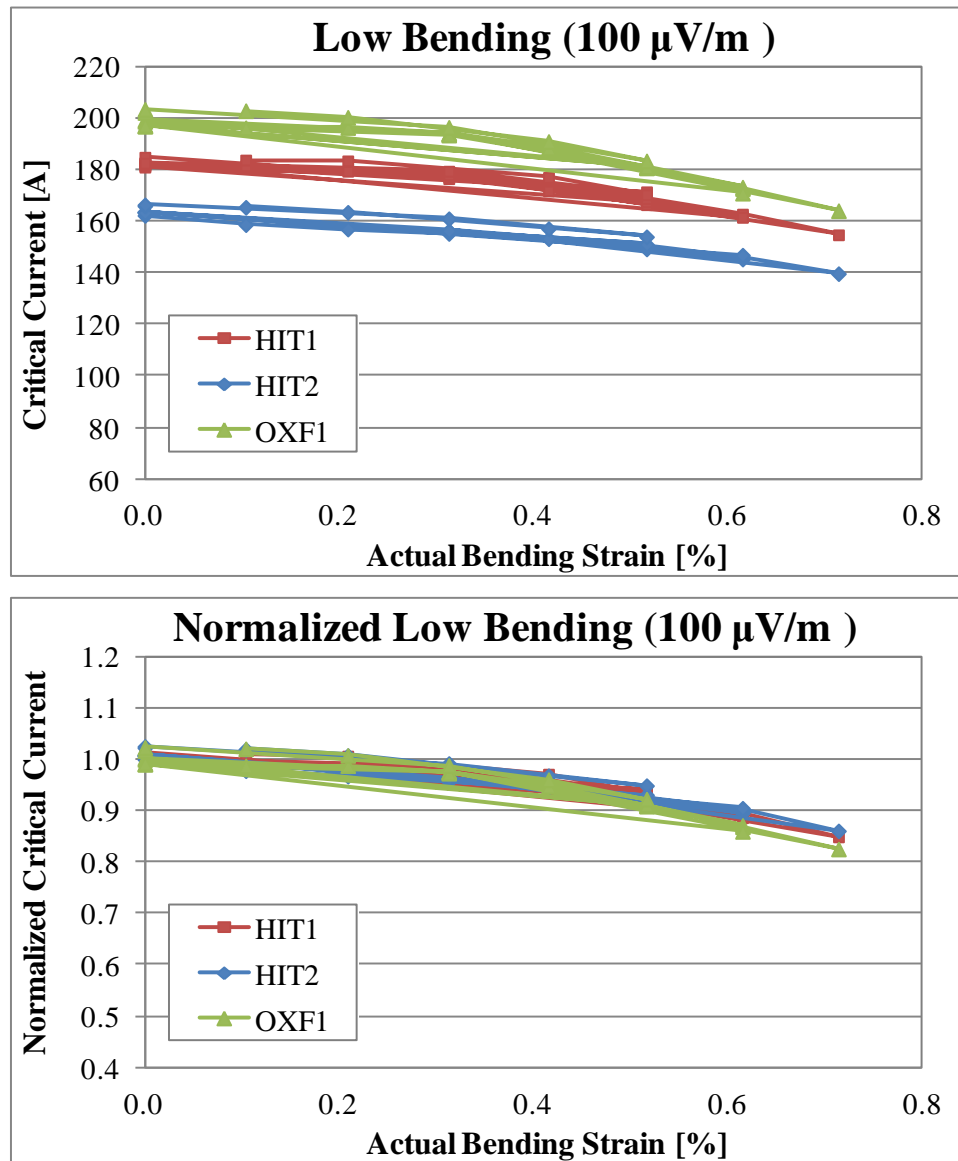
Figure 6.20 – Critical current results for low bending samples.

One key feature of the results that should be noted is the significant difference in the magnitude of the critical currents for the HIT1 and HIT2 samples. Both these samples were from the same spool of Nb_3Sn wire and were put through the same heat treatment. Therefore, it is intriguing to find almost a 20 A difference between the samples. This difference is within the manufacturer's specified range for the wire, however considering preparations were exactly the same this difference is unexpected. There might have been some damage caused to the wire during mounting and soldering but that is unknown.

In addition to critical current characterization over the entire bending range, additional tests have been run to gain an increased understanding of the overall performance of the Nb_3Sn strands and the sample holder. Reversed current tests over a range of bending strains were conducted first. The typical current direction is so that the Lorentz forces act radially inward toward the center of curvature when the samples are deformed. Therefore, the reversed current tests apply a radially outward load on the strand. The tests were done to identify any effect the load direction might have on the performance of the samples. Reversed current results for the HIT1 and OXF1 samples are shown in Figure 6.21.

From the plots it is clear that the reversed current follows the same behavior as the typical current direction. The data from the additional reversed current tests lie on top of the curves of the normal current tests with an inward facing Lorentz load. Upon closer inspection it appears the reversed current results tend to have a slightly larger critical current. This difference is only one or two amperes, thus the

Lorentz load direction does not have a major influence on the critical current results at low bending strains. This was the expected result based on the FEA simulations for the new low bending sample holder. These two samples were used to represent the behavior found for all of the low bending samples.
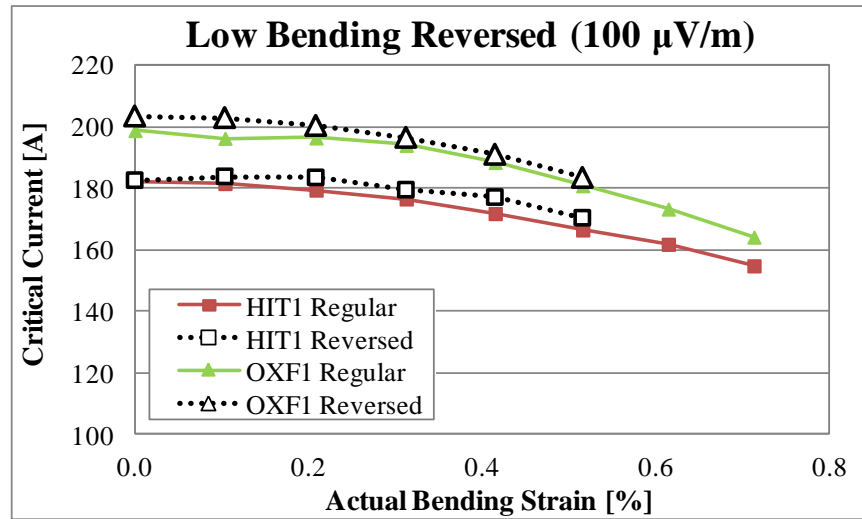
Figure 6.21 – Reversed current comparison for two low bending samples.

The effect of cycling the bending strain up and then down was investigated next. Additional tests were conducted that cycled the strain on the sample up to 0.5% and then back down to zero five times in a row. On the last cycle the critical current results were recorded at 0.5% and then 0.0%. These results are shown in Figure 6.22 plotted along with the original critical current results.

The results clearly indicate that the two critical current values after cycling lie directly on top of the original data. This means that the cycling tests conducted did not degrade the performance of the sample. This is due to the fact that the number of cycles tested was low considering the number of cycles a sample will experience during its lifetime in a magnet application. In addition to this the strain

was only cycled up to 0.5% strain, a strain level that was shown earlier to be fully

recoverable, meaning no damage was done to the filaments. The results shown are

for the HIT1 and OXF1 samples only but the same behavior was experienced in

all low bending samples.
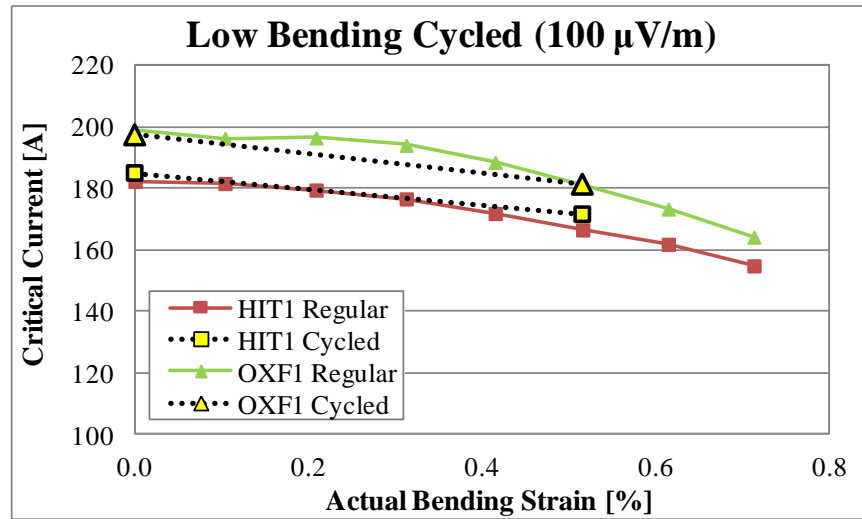
Figure 6.22 – Cycling effect on the critical current of two low bending samples.

High Bending Results

The critical current results for the high bending samples over the entire bending

range are presented in Figure 6.23. These results were from the test carried out on

the new high bending sample holder. Testing began at an initial setting strain of

0.6% and then was tested up to the maximum bending and back down. This was

done to initially characterize the samples within their design range only.

Following this the high bending sample holder was tested below 0.6% strain. No

mid range cycling up and down was done for due to time limitations.

The critical current of the HIT4 sample, as the bending was being decreased from

the maximum strain, was lower than the original current, which is a sign of

139

noticeable permanent degradation. However, once back to zero bending the critical current recovered and went back to its original value, showing that there was no permanent degradation. All tests after this followed the original loading curve therefore showing complete recoverable critical current for the HIT3 sample. Consequently this lower current effect found as the sample was being unloaded was caused by a hysteresis effect which may have been eliminated if mid range cycling was used. Besides this, both Hitachi samples had very similar critical current degradation trends and were found to have no permanent reduction in performance after bending was removed.
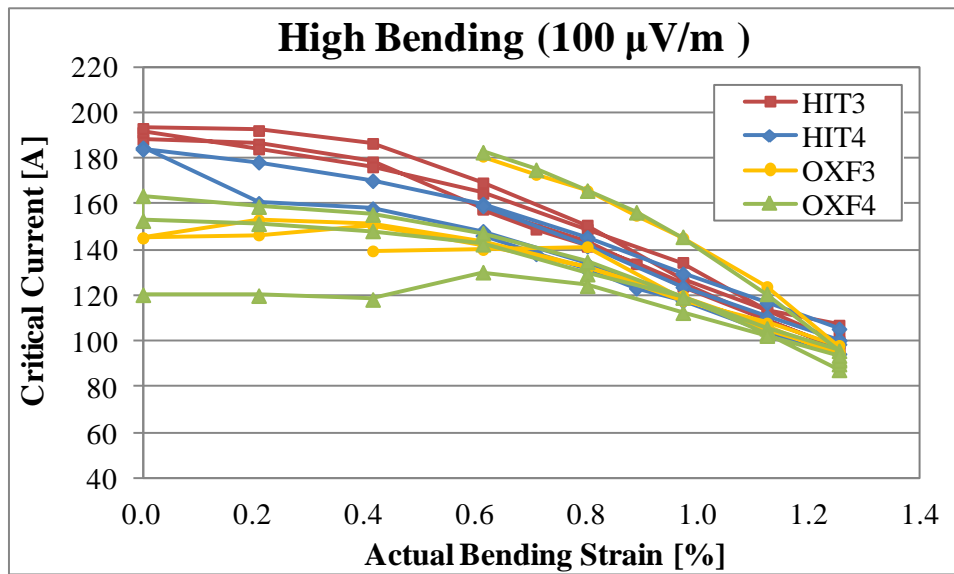
Figure 6.23 – Critical current results for high bending samples.

The critical current of both Oxford samples was different from that of the Hitachi samples. The Oxford samples were found to have significant degradation after being unloaded from the maximum bending strain. This showed that the Oxford type Nb_3Sn samples were more sensitive to high bending strain which most likely fractured some of the Nb_3Sn filaments permanently degrading its electrical

140

performance. The Oxford samples tested were also prone to quenching. Both samples quenched many times during the testing, which may have also lead to some of the permanent damage that was done to the samples. Although the samples showed permanent degradation at low bending, all additional tests showed that the critical current followed this same trend and did not degrade further as the bending was increased again.

The normalized critical current results for the data showed in Figure 6.23 are presented in Figure 6.24 below. Because the samples were first tested at 0.6% strain they have been normalized to their projected critical currents at zero bending based on the percent degradation found in the low bending samples at 0.6%. The plot of the normalized results for all samples shows some interesting trends and differences between the two sample types.
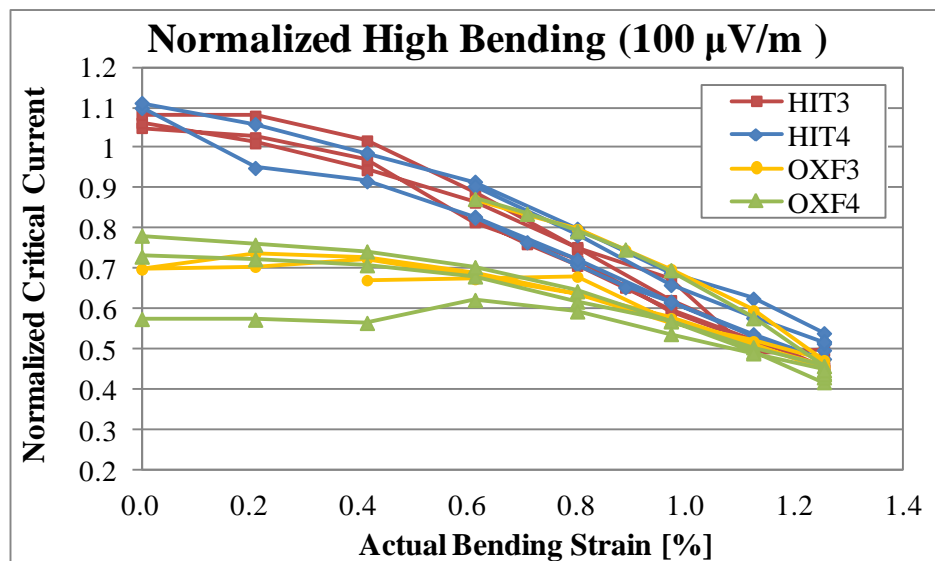
Figure 6.24 – Normalized critical current results for high bending samples.

First off, the critical current for the Hitachi and Oxford samples is almost identical between 0.6% and 1.0% actual strain. This indicates that both type samples are

141

being degraded roughly the same amount. After 1.0% strain the Oxford samples have noticeably more critical current reduction. At the maximum strain of 1.25% the Oxford samples experienced around 45% reduction in current while the Hitachi samples only experienced about 55% reduction.

Although the Oxford samples had permanent degradation and only returned to between 70% and 80% of their original critical current at zero bending, they maintained this same critical current level as they were bent back up to 1.25% strain. Thus, after the initial permanent degradation the critical current was fairly recoverable with only an additional few percent lost at low bending. The Hitachi samples were found to show some hysteresis or a slight spread in critical current results, but the results were always recoverable and followed the same trend.

As done for the low bending sample holder, additional tests were run to further characterize the sample performance. The reversed current results for HIT3 and OXF4 are shown in Figure 6.25. These two samples were chosen to characterize the behavior of all four samples. Similar trends to those found in the low bending sample holder are seen in the plots.

For the most part the reversed current data points follow the same trend as the regular current results. There are some slight differences between the results but nothing major enough to denote a significant effect from the Lorentz load direction. Therefore, the Lorentz load direction was again proven to have a minimal effect on the critical current results, even for the thinner high bending sample holder.
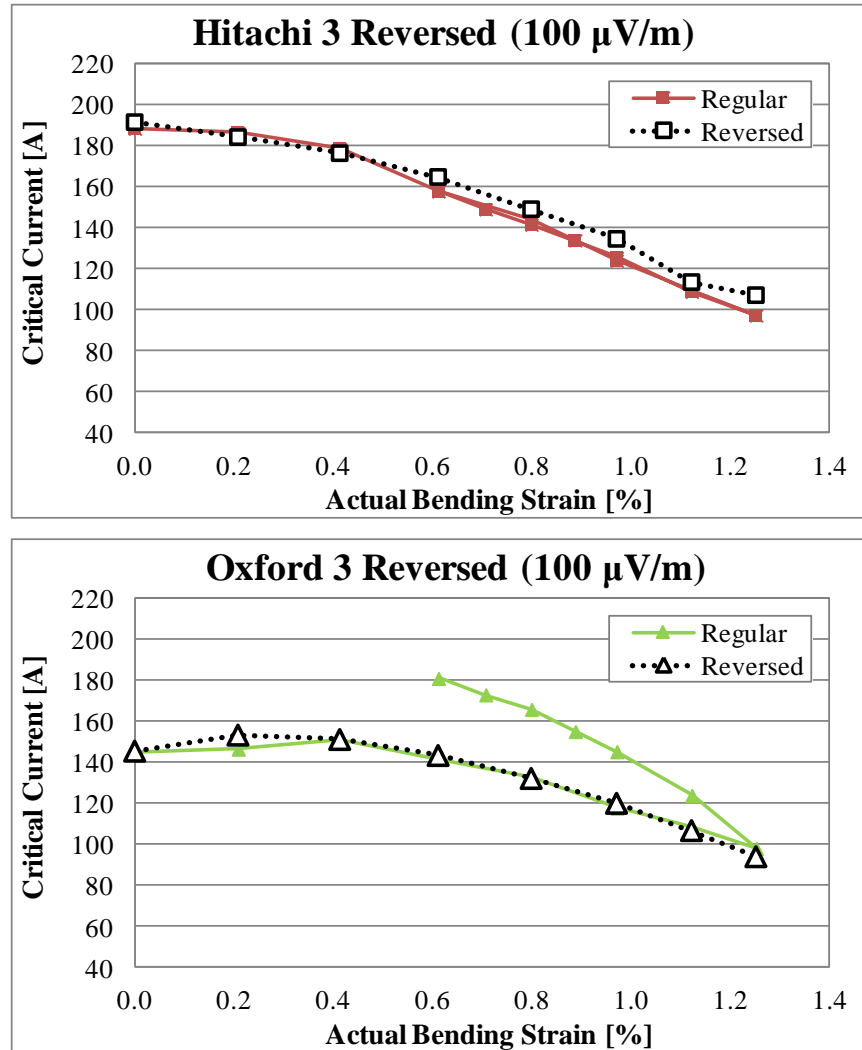
Figure 6.25 – Reversed current results for two high bending samples.

The effects of cycling the strain up and back are were also tested for the high

bending sample holder. From its maximum bending strain of 1.25% the sample

was cycled down and back up 4 times in a row. After the last cycle the strain was

then recorded at 1.4% setting strain and at every 0.2% as the bending was

decreased back to zero. The results from these tests are shown in Figure 6.26

which plots the results from the HIT3 and OXF4 samples. These two samples had

the most data and are used to represent the behavior of the other two samples

from the same manufacturer.
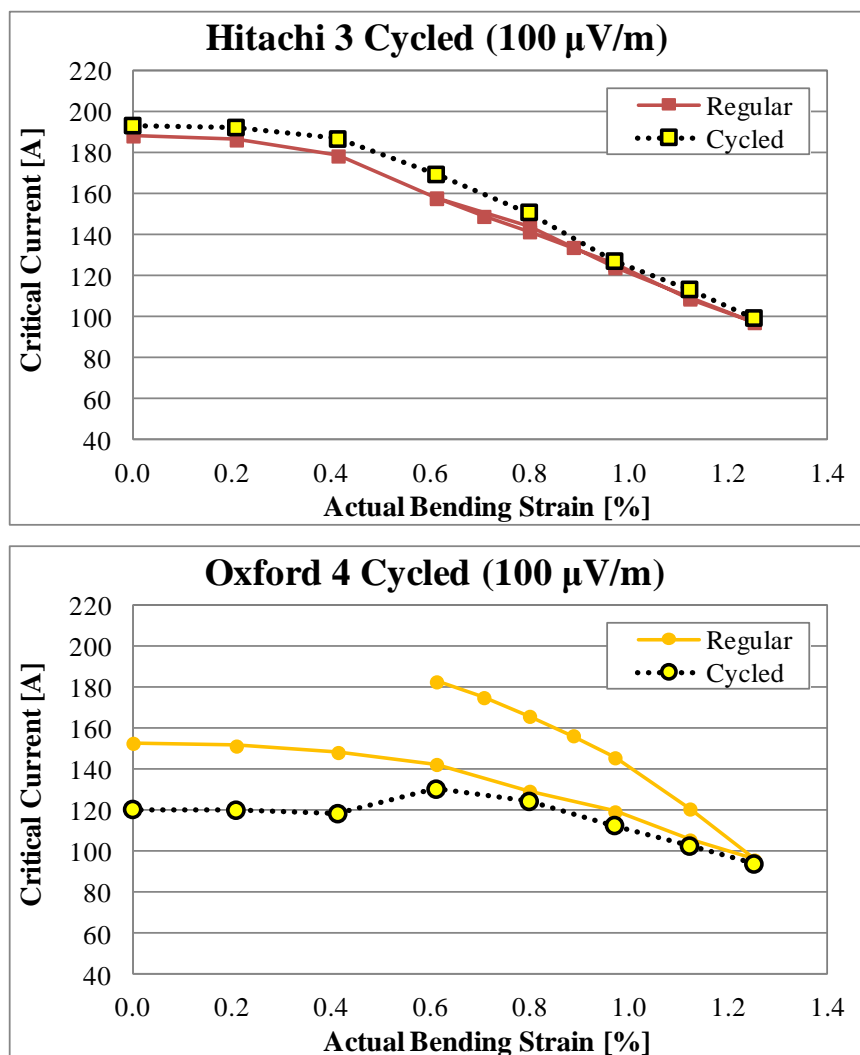
Figure 6.26 – Cycling effect on the critical current of two high bending samples.

The results of the HIT3 sample after it was cycled show no noticeable decrease in performance and might even show a slight increase. The data follows the same trend as the original results and therefore confirms the findings from the low bending Hitachi sample after cycling. In contrast to this, a different behavior was seen for the internal-tin type Oxford sample presented above.

The OST4 sample showed a noticeable degradation in critical current after cycling. As the bending strain of the OXF4 sample was decreased the critical

current stopped being recoverable around 0.6%. Below this strain level the sample showed significant permanent reduction in critical current. The critical current was over 30 A lower than the already degraded critical current at zero bending.

This demonstrates that after the bending strain was cycled the Oxford samples experienced more permanent damage causing a drop in electrical performance. The cycling was done up to the maximum bending of 1.25% strain, which was a bending state that was already shown to cause damage to the filaments. Therefore, multiple cycles at this strain level would potentially cause more damage to the already fractured filaments leading to the performance drop that was experienced.

6.3.3 N-value Results

As previously mentioned, another characteristic of superconductors is the n-value that describes the sharpness of the transition from a superconductive state to a resistive state. A larger n-value will have a steeper more rapid transition while a lower n-value will have a slower more gradual transition. These n-value results presented below show some interesting characteristics over the bending range.

The n-values for the low bending samples are plotted in Figure 6.28. For the low bending Hitachi samples the n-value seemed to degrade very linearly as bending was increased. N-values for these samples range from about 35 to 45 at zero bending and from 15 to 20 at 0.7% bending strain. The HIT2 sample seemed to have a slightly steeper slope than the HIT1 sample. The low bending Oxford sample had very different behavior. The n-value for the OXF1 sample remained approximately flat

over the entire bending range. The n-values for this sample ranged from about 20 to 30 over the entire bending range.
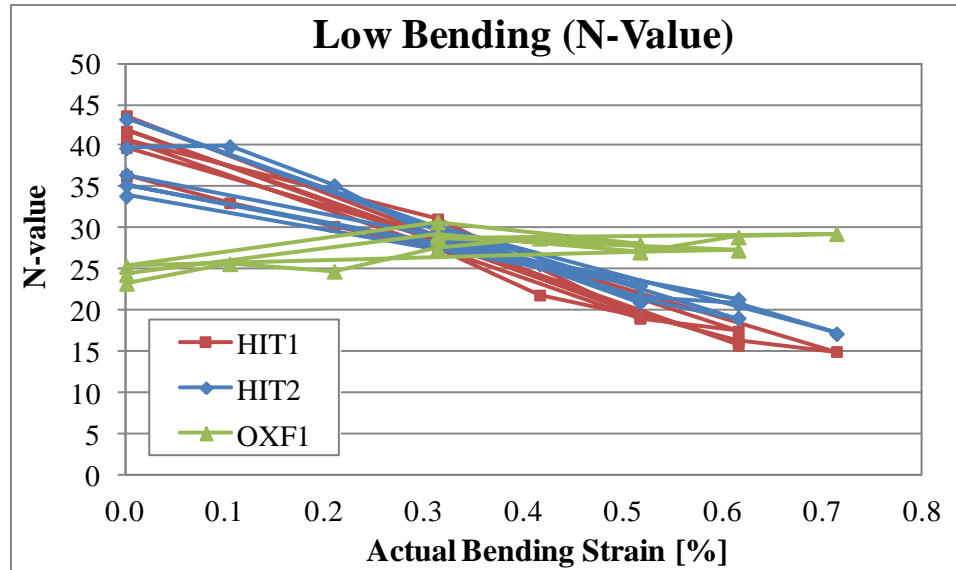
Figure 6.27 – N-values of the low bending samples.

The behavior of the samples for the high bending case are similar to those in the low bending case but also show some unique characteristics. The n-values for the samples in the high bending sample holder are presented in Figure 6.28.

The n-value of the Oxford samples started around 30 at 0.6% bending and decreased linearly to a value of 10 at the maximum strain of 1.25%. After this the n-values of the Oxford samples experienced no real change besides small fluctuations between about 8 and 12 over the bending range. This flat n-value behavior is the same as was seen in the Oxford strand in the low bending sample holder. The Hitachi samples experienced a slightly concave trend over the full bending range. As the bending strain was increased the n-value in the samples decreased. The n-value was also recoverable and followed the same trend as bending was decreased. This decreasing n-value with increasing strain is similar to the trend found for the Hitachi sample in

146

the low bending sample holder. The difference was that in the low bending case the trend was more linear, while in the high bending case the trend is more curved.
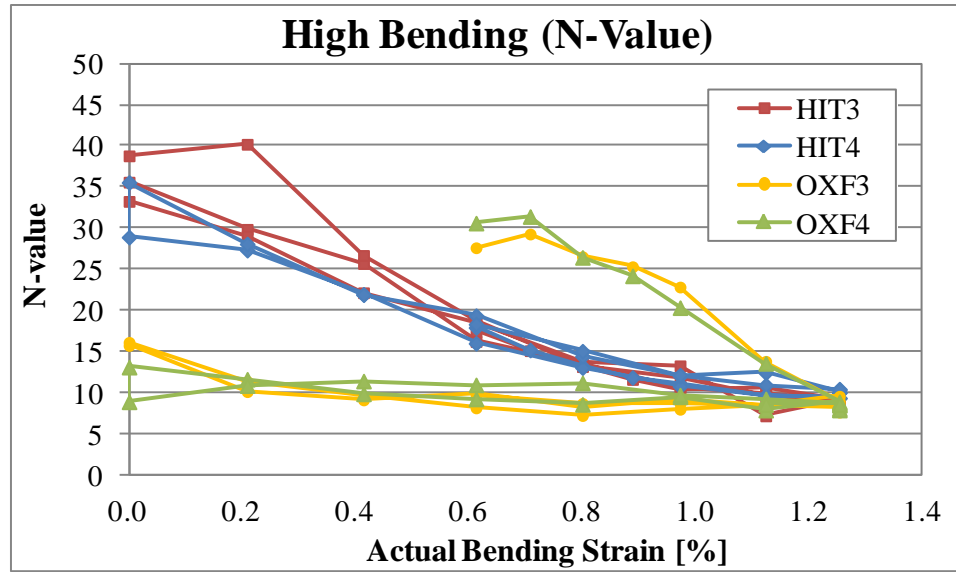
Figure 6.28 – N-values of the high bending samples.

6.3.4 Comparison to Prior Experiments

The experiments conducted in 2010 by Mallon focused on internal-tin type Nb_3Sn strands [16], while the experiments done by King in 2011 focused on bronze-route samples [2]. The experiments presented in this thesis tested both type Nb_3Sn wires. For consistency of results, the same Oxford Superconducting Technology (OST) wire that was tested by Mallon was chosen for the internal-tin samples and the Hitachi (HIT) wire used in King's experiments was selected for the bronze-route samples.

The new samples from both manufacturers were taken off of the same spool of wire used by the predecessors. This ensures that the Nb_3Sn samples are not only of the same type and from the same manufacturer but are also from the same

147

original length of wire. This is very beneficial because different spools of superconducting wire may have slightly different performance solely based on the manufacturing variability for the wire. To keep things even more uniform, the new samples were put through the same heat treatment as done prior. The uniformity and equivalence of the old and new samples allowed for a direct comparison of the experimental results.

The critical current results from the OST samples in the new experiments were compared alongside the critical current results from the previous experiments conducted by Mallon. These critical currents were normalized and plotted together in Figure 6.29. Only the initial loading and unloading curves for the selected samples are plotted. Recall that Mallon's experiments used a low bending (LB), medium bending (MB) and high bending (HB) sample holder. The current tests used only two sample holders; high and low bending. Due to quenching and galling of the gear box little data was collected for the 2010 (MB) sample.
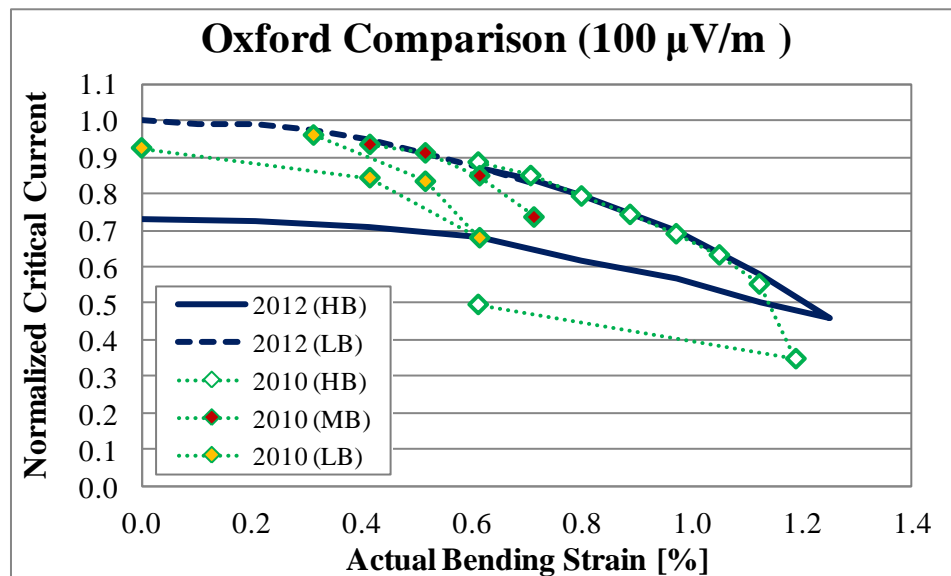
Figure 6.29 – Normalized critical current results of Oxford samples (2010 and 2012) [16].

The results presented in Figure 6.29 clearly indicate that the high bending sample holder from Mallon's 2010 experiments had very similar critical current results to those found for the new high bending sample holder. The 2010 HB sample holder results do show a much lower critical current than the new design at the maximum bending strain of 1.25%. For that same reason, the recovery curve for the 2010 HB sample holder experienced more permanent degradation than in the new design. That being said, overall the old high bending results were very comparable to the new high bending results. This is an expected result because both sample holders have similar designs including no channel walls.

The 2010 results for the old low and medium bending sample holders did not show the same behavior as the new low bending sample holder. Instead, these samples experience a sharp decrease in critical current as bending is increased. The new low bending design, which has no channel walls, does not experience this sharp degradation. For that reason, this lower critical current found in the old sample holder designs is proven to be caused by the channel wall bowing effect described in section 4.

The normalized Hitachi results from the old and new experiments are compared in Figure 6.30. Overall, these results show very similar behavior as found in the Oxford samples. The old high bending data from 2011 appears to almost exactly match the new data for bending strains 0.8% and 1.25%. This indicates that both high bending sample holders, old and new, apply similar bending strain to the sample which produces the similar critical current behavior that is shown.

The medium bending results clearly shows the distinct critical current discrepancy that brought about this current research. The critical current in this sample holder is much lower than the critical current in the old high bending sample holder for the same bending strains. This indicates that the performance of the medium bending sample holder gets degraded quicker than in the high bending sample holder. Similar behavior is also seen in the low bending sample holder at its highest bending strains. This increased degradation of critical current has been explained to be caused by the large strain fluctuations that the strand experiences due to the channel walls bowing. The new low bending sample holder has no channel walls and therefore experiences no sharp degradation. The results instead match nicely with the critical current from the new high bending sample holder.
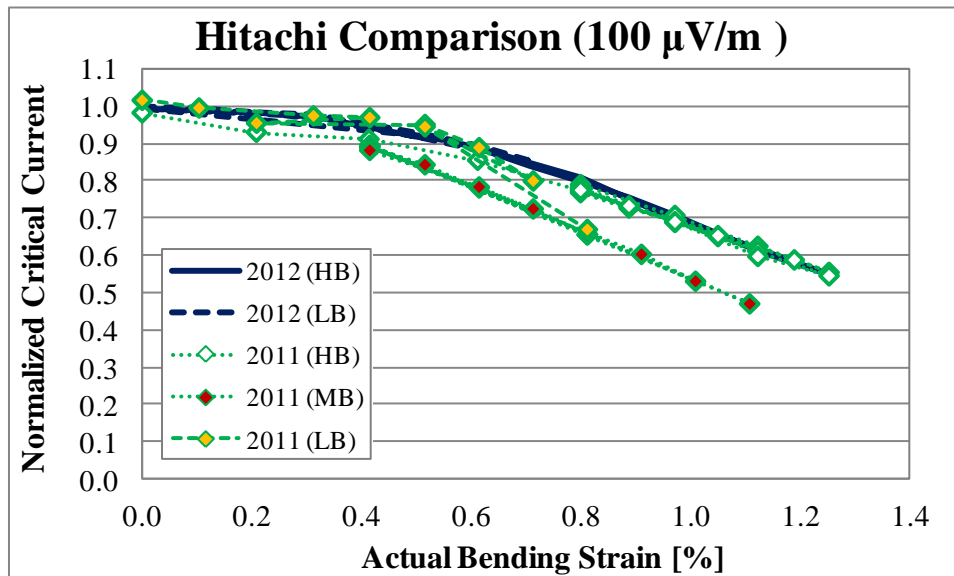
Figure 6.30 – Normalized critical current results of Hitachi samples (2011 and 2012) [2].

In conclusion, the figures presented above illustrate that the samples from each manufacturer have similar overall critical current trends. In addition to this, the initial critical current for the old and new sample holders had comparable

150

magnitudes before the sharp degradation was experienced in the old experiments. The samples in the old high bending sample holder showed almost identical critical current behavior to the sample in the new high bending sample holder. The results from the new low bending sample holder also match nicely to the results from the new and old high bending sample holders, which confirms the improved performance of the new sample holder designs.

6.4 Empirical Modeling

The critical current behavior of the Nb_3Sn strands under pure bending can be better understood using empirical models. The experimental data from all tested samples was evaluated using a new integrated model developed by Takayasu [21]. The new model accounts for effects from neutral axis shift, current transfer length, mechanical filament breakage and uniaxial strain release. The original model developed by Ekin, that considered the critical current distributions in a strand under bending due to uniaxial strain geometry, only took into account the current transfer length effects [13]. The new integrated model will enable us to better characterize the critical current behavior using the influences from each of these four parameters.

6.4.1 Integrated Model Parameters

The integrated model considers two extreme cases; perfect current transfer and no current transfer. These two cases represent the two extremes for current transfer and therefore will encompass the real life experimental results. The perfect

current transfer case means that current is shared freely between superconducting filaments with minimal resistance. For the no current transfer case, current is shared minimally between filaments due to a high transfer resistance. The behavior of the analytical model in between these two extremes is governed by the four parameters mentioned above. These four parameters are the neutral axis shift, current transfer length, filament breakage and uniaxial strain release.

The neutral axis shift parameter refers to a natural shift of the neutral axis while the strand is in bending. This shift is mostly caused by uneven yielding of the copper matrix while under bending. This parameter creates a local change in the critical current of the model depending on its value at different bending states.

The current transfer length parameter relates to the length over which current is shared between twisted filaments. The severity of its effect is directly dependent on the twist pitch length of the filaments within a strand. The parameter governs the behavior of the analytical model by controlling its position between the two extreme current transfer curves described above.

The filament breakage parameter refers to the mechanical fracturing of Nb_3Sn filaments on the tensile side of the strand. The severity of the breaking generally increases as bending increased. This filament fracturing effect helps model the irreversible permanent degradation some samples experience after high bending strains have been applied.

The uniaxial strain release parameter describes the thermally induced pre-compressive strain in the Nb_3Sn strand after cool-down from its heat treatment

152

process. This parameter affects the overall level of critical current in the model based on the amount of pre-compressive strain in the sample.

The magnitude of these parameters varies with the amount of applied bending; however, there is no specific literature which defines what these parameters should be for each type of Nb_3Sn wire. Instead, the parameters are iteratively adjusted and modified for each specific application. For this reason, the general behavior and magnitudes of these parameters was based on the prior modeling done by Takayasu [21]. The iterative process used, helped to identify each parameters influence on the analytical model and on each other. The chosen trends for the parameters were selected to achieve the best fit to the experimental critical current data. The best fit refers to adjusting the curve of the analytical model until its shape closely matches the experimental data.

Figure 6.33 and Figure 6.36 show the shapes of the chosen parameter curves used to fit the experimental results from all Hitachi and all Oxford samples respectively. In the figures, the orange parameter curve is used to fit the experimental loading data and the dashed curves are used to fit the recovery data. The dashed recovery curves begin at the max peak strain that was reached during testing; 0.89% for high bending and 0.50% for low bending.

6.4.2 Hitachi Wire Modeling

The fitting results from the integrated modeling of Hitachi samples are shown in Figure 6.31 and Figure 6.32. Figure 6.31 is a plot of the low bending critical current results for the HIT1 sample. Figure 6.32 is a plot of the HIT3 results for

the high bending sample holder. These two samples were chosen to characterize the trend of all Hitachi samples under low and high bending cases. The critical current results in these figures are plotted against the peak strain. The peak strain refers to the maximum strain that the filaments within the strand experience. These strains will be slightly smaller than the actual strain on the surface of the sample which was used prior.

In the following two plots, the orange circles represent loading data: critical current values that were recorded as the sample was loaded for the first time. The red cross-marks represent the recovery data: critical current values from the initial unloading of the sample. The blue dashed line represents the perfect current transfer case while the green dashed line represents the no current transfer case. The black lines refer to the best fit generated by the analytical model. The solid line indicates the best fit of the loading data, while the dashed line indicates the best fit for the recovery data.
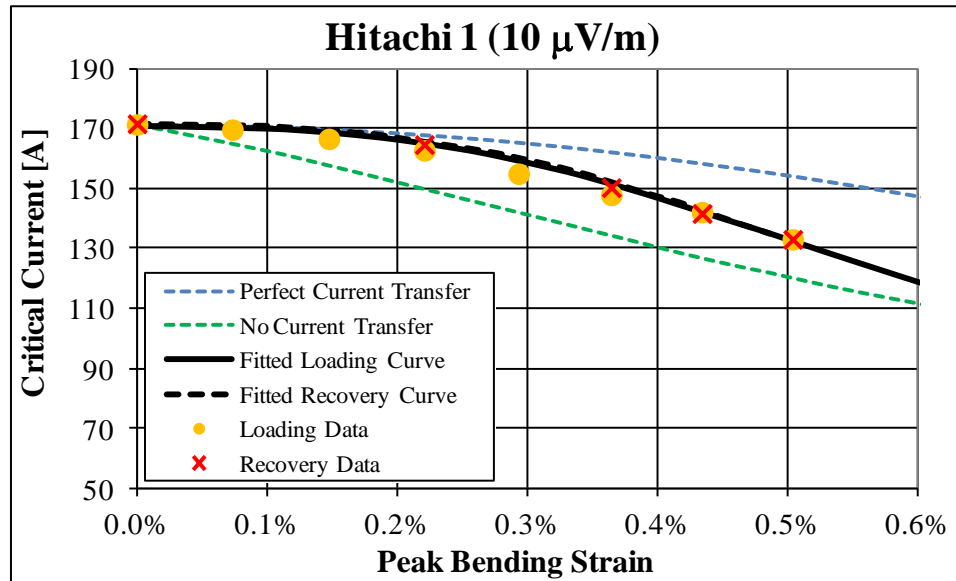
Figure 6.31 – Integrated model fit to experimental low bending data for Hitachi samples.

154
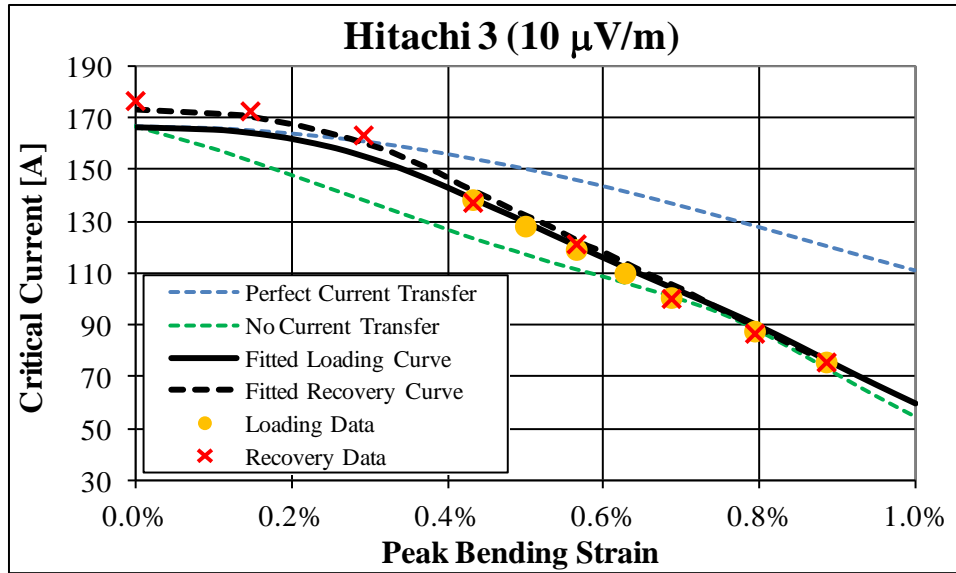
Figure 6.32 – Integrated model fit to experimental high bending data for Hitachi samples.

The first thing to note about the previous two figures is how closely the analytical fits (black lines) match the experimental data. This indicates that the four parameters used in the analytical model were able to nicely approximate this experimental behavior. The parameter trends that were used to achieve this fit will be discussed, but the general behavior and characteristics of these results will be described first.

One clear characteristic of the behavior shown in the above two plots is that the perfect current transfer curve is a good fit for the experimental data at small bending; while the no current transfer curve becomes a good fit at high bending. For both Hitachi samples, the transition from the perfect current transfer case to the no current transfer case began at a peak strain of around 0.2%. The transition ended at a peak strain of about 0.7% when the experimental data matched the no current transfer case. The shape and behavior of this transition is an important characteristic of the overall critical current behavior of the samples.

155

Another interesting finding in the high bending results shown in Figure 6.32 is a noticeable increase in the critical current recovery data at low bending. This higher critical current was experienced below a peak strain of 0.3%. This is a very unique characteristic, in the sense that most critical current behaviors tend to decrease or stay the same as loading is removed. That being said, this is an important behavior that was identified for only the high bending samples and was not seen in the low bending results shown in Figure 6.31.

The last main characteristic of the Hitachi results seen in both plots above is the recoverable nature of the critical current. In other words, the samples show no permanent degradation in critical current upon unloading. This indicates that the samples have not been permanently damaged. This behavior for a bronze-route wire has also been seen previously and is likely caused by the very uniform cross-sections that are generated by this manufacturing technique.

The best analytical fits (black curves) generated from the integrated model were produced from the four parameters curves presented in Figure 6.33. In the figure below, the orange lines represent the parameter curve used to fit the loading results. The dashed lines refer to the curves used to fit the recovery or unloading results. The loading parameter curves (orange line) for the low and high bending data were exactly the same; however, the recovery parameter curves (dashed lines) were at times different for the two cases. The high bending recovery curve (red dashed line) and low bending recovery curve (blue dashed line) begin from the max peak strain reached during their respective tests.
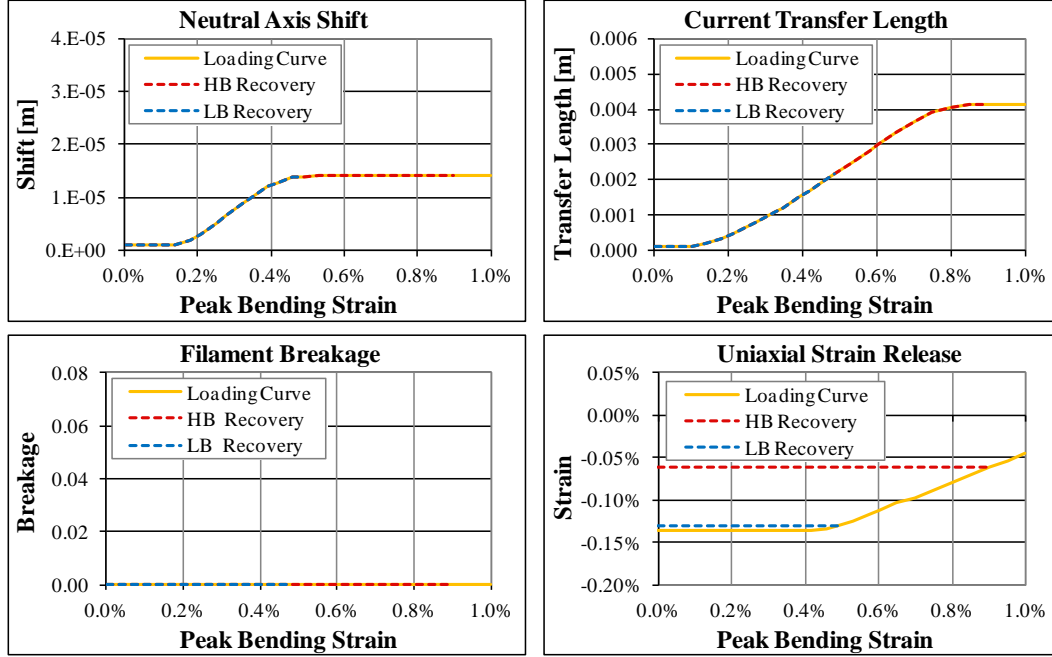
Figure 6.33 – Parameter curves used in the integrated model for the Hitachi samples.

These parameters curves can be used to rationalize the critical current behavior that was previously identified. One characteristic of this behavior that was mentioned above was the completely recoverable nature of the critical current in the Hitachi samples. This recoverable trend can be reproduced by setting the filament breakage parameter to zero, as shown in Figure 6.33. Zero filament breakage indicates that no damage or fracturing of the filaments has occurred during bending, allowing the sample to carry the same amount of current.

Another main characteristic of the critical current behavior described above was the transition from a perfect current transfer case to a no current transfer case. The transition of the analytical fit can be modified to match the transition of the experimental data using the current transfer length parameter. The shape of this parameter curve, as shown above in Figure 6.33, directly controls when the

transition begins, how steep the transition is and when the transition ends. The loading parameter curve (orange line) begins flat, increases linearly from 0.1% to 0.8% peak strain and then end flat. The small parameter value at the low bending, keeps the analytical model close to the perfect current transfer case. The large parameter value at the high bending keeps the analytical fit close to the no current transfer case. The shape of the parameter curve in between is used to match the trend of the experimental data. Based on the recoverable unloading data, the recovery parameter curves (dashed lines) follow the same trend as loading.

The most interesting characteristic of the high bending Hitachi behavior that was mentioned above was the noticeable increase in the critical current at low bending strain upon recovery. This increase in critical current can be explained using the uniaxial strain release parameter. The uniaxial strain release parameter is a measure of the thermal pre-compressive strain within the sample. The loading parameter curve (orange line) in Figure 6.33 shows that after a peak strain of 0.5% the pre-compressive strain in the sample begins to be relieved by the tensile effects of the applied bending strain. This alleviation in pre-compression is irreversible and therefore cannot be recovered.

Consequently, the high bending uniaxial strain release curve for recovery (red dashed line) is held constant at the alleviated strain value at a peak strain of 0.89%. This parameter curve is depicted in Figure 6.33, which clearly shows that the parameter recovery curve (red dashed line) has a much smaller compressive strain at low bending than the parameter loading curve (orange line). This lower

158

value of thermal pre-compressive strain allows the sample to carry a greater amount of current which produces the higher critical current found at low bending. Similarly, the low bending recovery parameter (blue dashed lines) was recovered from the slightly alleviated strain at a peak strain of 0.5%. The only slightly alleviated strain does not produce any appreciable increase in current.

The neutral axis shift loading and recovery curves are shown in Figure 6.33 and were used to generate the analytical fittings. However, it was determined that this parameter had minimal overall influence on the behavior of the fit. This same result was found for the Oxford samples presented next.

6.4.3 Oxford Wire Modeling

As done for the Hitachi results above, the integrated model was also used to fit the experimental data from the Oxford samples. The low bending behavior of the Oxford wire was represented by the OST1 sample and the high bending behavior was characterized using the OST4 sample. The modeling results for the OST1 low bending sample are presented in Figure 6.34 and results for the OST4 high bending sample are shown in Figure 6.35.

In the figures, the analytical fits (black lines) are plotted along with the experimental critical current results. Again, the experimental loading data is shown as orange circles and the experimental recovery data is shown as red crosses. The two extreme current transfer cases are once more depicted by dashed blue and green lines. Similar to above, the analytical fits (black lines) in the plots

closely follow the experimental loading and recovery results. This indicates that the four parameters were able to produce an acceptable fit to the data.
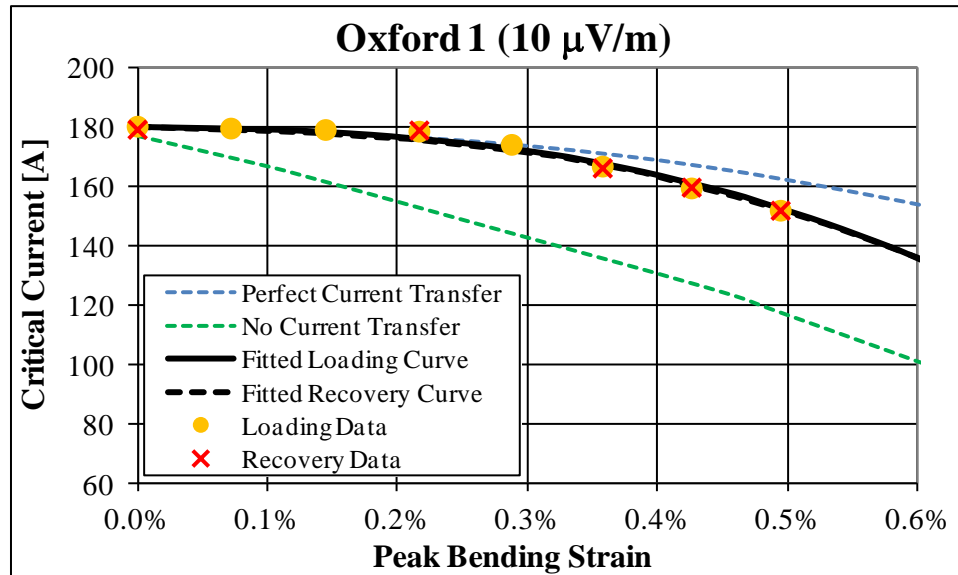
Figure 6.34 – Integrated model fit to experimental low bending data for Oxford samples.
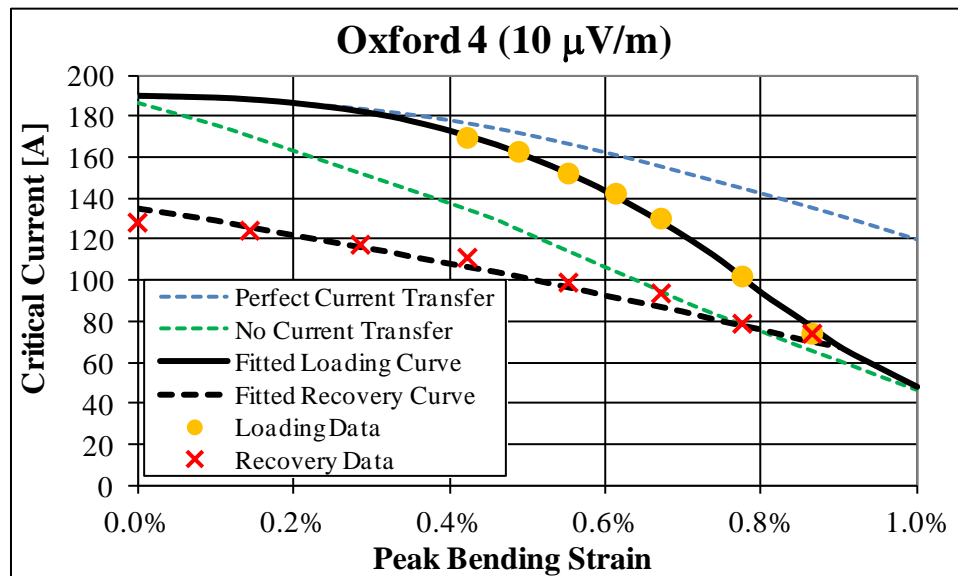
Figure 6.35 – Integrated model fit to experimental high bending data for Oxford samples.

The behavior of the critical current results presented in the above two plots are similar to the Hitachi results in some ways and very different in other ways. One characteristic of the Oxford behavior is the transition of the critical current data

160

from a perfect current transfer case to a no current transfer case. This is the same trend that was seen for the Hitachi samples; however, it is clear from the above plot that the shape and behavior of the transition is not the same. For the Oxford samples the transition begins later at a peak strain of around 0.3%. The transition also ends later and converges with the no current transfer case at around 0.9% peak strain. The more curved and gradual trend of the transition is also a unique behavior of the Oxford samples.

The most unique behavior of the Oxford samples that is different from the Hitachi samples is the severe amount of permanent degradation that was experienced in the OST4 sample shown in Figure 6.35. The plot indicates that the sample experienced significant damage while being initially loaded up to high peak strains. This damage permanently reduced the electrical capabilities of the sample upon unloading. The OST1 sample did not experience any permanent degradation which indicates no damage is done to the sample at a peak strain of 0.5%.

The parameter curves shown in Figure 6.36 were used to create the analytical fits (black lines) of the loading and recovery data in the previous two plots. Because the analytical fits are created using the four parameters below, they can be used to explain the critical current behavior that characteristics described above. In the following figure, the orange lines again indicate the loading parameter curve, while the dashed red lines indicate the recovery parameter curves. The recovery parameter curves are differentiated by blue dashes for low bending and red dashes for high bending. As done previously, the recovery parameter curves begin at

their respective max peak strain that was applied during the testing. Thus, the low

bending recovery begins at 0.5% and the high bending recovery starts at 0.89%.
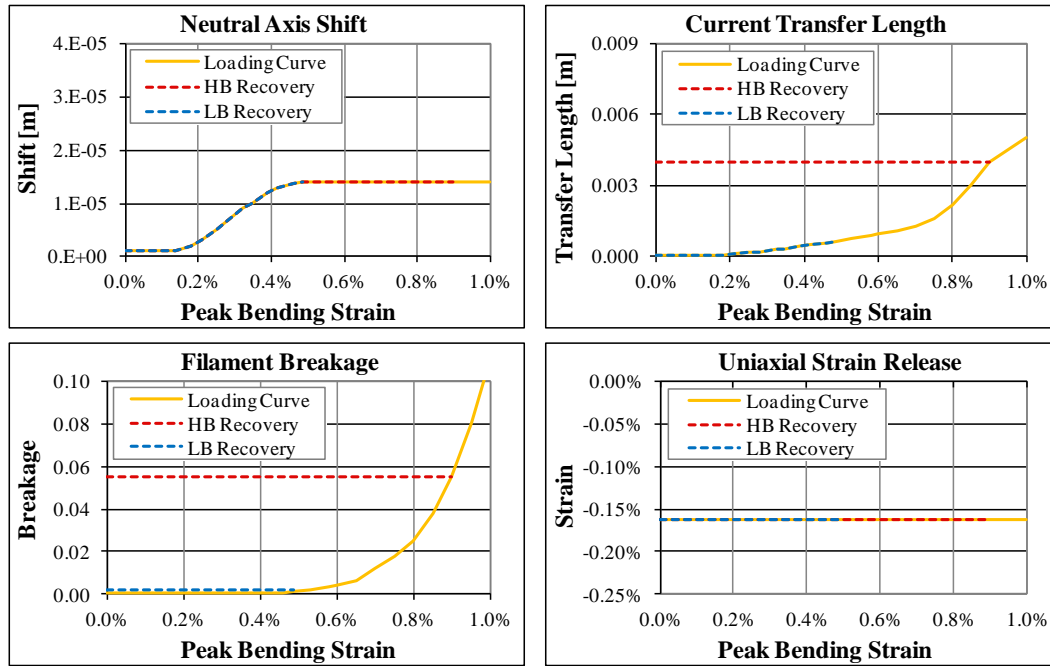
Figure 6.36 – Parameter curves used in the integrated model for the Oxford samples.

As mentioned above the four parameter curves in Figure 6.36 were chosen to

generate the best analytical fit for the experimental data. Therefore, these four

parameters can explain the critical current behavior presented in Figure 6.34 and

Figure 6.35. The most distinct behavior of the high bending OST4 sample was the

large permanent degradation that was experienced after max bending was applied.

This irreversible degradation can be directly described using the filament

breakage parameter. The filament breakage refers the amount of filaments that

have fractured within the sample. At very high tensile strain the amount of

fracturing can be high for this internal-tin wire.

The filament breakage loading curve shown in Figure 6.36 can be used to clearly

162

explain this phenomenon. For the loading curve, up to a peak strain of 0.5% there is no filament breakage. This is done to produce no damage in the low bending OST1 sample over its entire bending range. Therefore, the low bending parameter recovery curve will be zero as shown in Figure 6.36 which explains its recoverable critical current behavior.

To create the severity of the permanent degradation that was experienced in the sample, the filament breakage loading curve was sharply increased after 0.5% peak strain as indicated in the above figure. At the max peak strain of 0.89% for the high bending sample, a significant amount of filament breakage has been experienced. Because this filament breakage is an irreversible permanent effect, the filament breakage recovery curve is held constant at this level as the bending is removed. This trend of this parameter recovery curve is shown in Figure 6.36, which clearly indicates the high filament breakage upon unloading. This high filament breakage indicates many filaments have fractured which reduces the amount of current the sample can carry leading to the permanent degradation in critical current that was seen in the results.

The permanent reduction in critical current is also characterized in part by the irreversibility of the current transfer length parameter. The filament fracturing at high bending also caused a permanent degradation in the n-values of the samples as seen earlier in Figure 6.28. A permanent change in the n-value leads to non-recoverable current transfer length behavior. This behavior is clearly shown in the recovery current transfer length curve (red dashed line) in Figure 6.36. The

current transfer length is held constant at the value corresponding to the max peak strain of 0.89%. This higher current transfer length at low bending adds to the permanent reduction in critical current that is experienced while unloading. The initial shape of the current transfer length loading curve (orange line) was chosen based on the transition of the experimental results from the perfect current transfer to the no current transfer, as was described in more detail for the Hitachi sample.

Because no increase in critical current was experience for these samples during unloading, the uniaxial strain release parameter was held constant over the entire bending range. Because no pre-compressive strain alleviated the recovery curve exactly matched the constant loading curve. This trend indicates that the high bending of this sample type did not relieve the pre-compression in the strand. This behavior may have been caused by the fracturing of the Nb_3Sn filaments.

Lastly, the neutral axis shift parameter was again found to have minimal influence and therefore the same parameter curves used in the Hitachi samples were again used for the Oxford samples. As for the Hitachi samples, this parameter was recoverable and followed the loading trend for the recovery curve. Considering the two wire types have similar Cu/non-Cu ratios and wire diameters, a similar neutral axis shift behavior in both samples is a reasonable assumption.

7.0 Conclusion

Superconductors are important technological materials for developing high field magnets. Nb_3Sn is a particularly common and advantageous material for this application however; it is very sensitive to strain which can cause operational degradations. Unexpected degradations of large ITER model superconducting magnet coils have driven attention to characterizing the performance of Nb_3Sn strands under different operational loads. The work presented in this thesis has been focused on characterizing these strands under pure bending loads.

The research presented here has been the culmination of pure bending research that started in 2005. Harris began the research by developing a variable strain bending device to characterize the critical current of superconducting strands under a pure bending loads [1]. Allegritti then continued this research and developed an innovative sample holder for the pure bending device [15]. The research continued on with Mallon who modified Allegritti's sample holder to cover a wider range of bending up to an applied nominal strain of 1.4% [16]. King collaborated with Mallon and continued his testing [2]. Discrepancies found by King in the experimental critical current results lead to the motivation behind this present work.

To identify a cause for the discrepancy in-depth finite element analysis (FEA) was conducted on the sample holders designed by Mallon. This FEA modeling was the first to include a strand mounted within the sample holder and was also the

first to include the real life effect of electromagnetic loading on the strand. Incorporating a strand into the model was an essential step to determine the influence of the sample holder and the Lorentz load on the distribution of axial strain within the strand. This detailed modeling of the strand revealed that the channel walls had an unexpected influence on the strain distribution within the strand. It was found that as the sample holder bent the channel walls bowed into the strand causing pressure points which created large longitudinal strain fluctuations along the strand.

From these findings two new sample holders were designed for the bending mechanism. The sample holders were designed similar so that they would both have the same influence on the strand eliminating the potential for a critical current discrepancy. They were also designed using a parametric study to minimize error from that of a pure bending state.

These new sample holders were then experimented using both bronze-route (Hitachi) and internal-tin (Oxford) type Nb_3Sn superconducting strands. The experimental results showed a consistent and smooth critical current trend in both sample holders with no major discrepancies. Samples from both manufacturers were found to exhibit a critical current degradation of between 40 and 60% at the maximum bending strain. The Oxford samples experienced around 30% permanent degradation while the Hitachi samples were completely recoverable.

The experimental critical current results were also evaluated using a new integrated model. This modeling has proven that the experimental data was able

166

to be fit with an integrated model, which explained the critical current behavior of the results using the four model parameters. This helped to validate, verify and understand the characteristics of the experimental results.

Future work for this pure bending research will include conducting additional experiments using the newly design sample holders. These additional experiments will be used to characterize more types of Nb_3Sn wires under pure bending. These experiments will also be used to build a more comprehensive set of pure bending characterization results, which can then be used to develop more accurate scaling laws. These more accurate scaling laws will better predict the full scale performance of a Nb_3Sn cable-in-conduit conductor which will allow more advanced magnets to be developed for ITER and other high field magnet technologies.

8.0 Appendix I: Critical Current Data

8.1 Low Bending Results (Day 1)

8.1.1 Hitachi 1

Percent Strain			Best Linear Fit				Critical Current (A)		
Setting	Actual		n-value	Intercept	R^2-value		Ic - 10 µV	Ic - 100 µV	Ic - 200 µV
0.0	0.000		36.342	-201.34	0.9798		171.058	182.246	185.756
0.1	0.104		33.093	-184.3	0.9908		169.342	181.544	185.386
0.2	0.209		30.218	-168.99	0.9761		166.256	179.419	183.583
0.3	0.313		27.620	-155.06	0.9865		162.418	176.539	181.025
0.4	0.415		21.871	-124.72	0.9853		154.616	171.782	177.314
0.5	0.516		19.118	-109.95	0.9827		147.566	166.454	172.599
0.3	0.313		31.136	-173.36	0.9862		164.533	177.162	181.151
0.0	0.000		40.681	-223.65	0.9706		171.053	181.014	184.124
0.5	0.516		19.034	-109.65	0.9797		148.496	167.591	173.807
0.6	0.615		17.493	-101.14	0.9703		141.824	161.776	168.315
0.3	0.313		29.427	-164.72	0.9866		164.988	178.417	182.669
0.7	0.714		15.002	-87.806	0.9607		132.748	154.770	162.088
0.6	0.615		16.314	-95.246	0.9656		141.368	162.797	169.863
0.5	0.516		19.449	-111.92	0.9831		149.990	168.841	174.967
0.3	0.313		28.806	-161.44	0.9897		164.364	178.041	182.377
0.0	0.000		39.816	-219.26	0.9681		171.301	181.500	184.687
0.0	0.000		35.510	-196.92	0.9822		170.376	181.789	185.373
0.6	0.615		15.761	-92.309	0.9761		139.595	161.554	168.817
0.0	0.000		41.814	-229.94	0.9642		172.962	182.754	185.808
0.5	0.516		19.399	-111.96	0.9875		152.253	171.441	177.678
0.0	0.000		43.692	-240.22	0.9578		175.364	184.853	187.809
0.0	0.000		31.455	-175.95	0.9600		169.644	182.528	186.595
0.3	0.313		20.928	-120.78	0.9635		160.746	179.441	185.484
0.5	0.516		15.583	-92.226	0.9844		146.912	170.306	178.052
0.4	0.415		21.742	-124.71	0.9754		159.237	177.027	182.762
0.2	0.209		29.044	-163.54	0.9783		169.453	183.434	187.865
0.1	0.104		22.645	-130.23	0.9225		165.997	183.764	189.476
Field Data: 15T			36.841	-203.81	0.9422		170.613	181.617	185.066
Field Data: 14T			38.077	-216.98	0.9954		204.067	216.788	220.771
Field Data: 13T			38.272	-224.66	0.9867		242.747	257.800	262.511
Field Data: 12T			42.14	-253.02	0.9859		287.409	303.550	308.584

8.1.2 Hitachi 2

	Percent Strain			Best Linear Fit				Critical Current (A)		
	Setting	Actual		n-value	Intercept	R^2-value		Ic - 10 µV	Ic - 100 µV	Ic - 200 µV
	0.0	0.000		39.762	-214.53	0.9774		153.155	162.286	165.140
	0.1	0.104		39.939	-214.54	0.9907		149.815	158.706	161.485
	0.2	0.209		35.195	-190.12	0.9927		147.051	156.994	160.116
	0.3	0.313		28.667	-156.8	0.9951		143.303	155.288	159.089
	0.4	0.415		25.63	-141.14	0.9852		140.089	153.257	157.458
	0.5	0.516		20.974	-117.16	0.9817		133.766	149.287	154.303
	0.3	0.313		29.769	-162.46	0.991		144.214	155.811	159.482
	0.0	0.000		43.266	-232.7	0.9721		155.078	163.555	166.196
	0.5	0.516		21.369	-119.23	0.9728		134.620	149.936	154.879
	0.6	0.615		19.072	-107.13	0.951		128.826	145.357	150.737
	0.3	0.313		30.301	-165.23	0.9915		144.811	156.245	159.860
	0.7	0.714		17.166	-96.959	0.9673		122.169	139.706	145.463
	0.6	0.615		20.791	-115.8	0.958		130.813	146.133	151.087
	0.5	0.516		21.609	-120.47	0.9558		135.015	150.197	155.093
	0.3	0.313		29.111	-159.23	0.992		144.418	156.305	160.071
	0.0	0.000		36.503	-198.27	0.9864		153.733	163.743	166.882
R	0.0	0.000		37.939	-206.1	0.9753		156.181	165.954	169.014
	0.6	0.615		21.355	-118.72	0.9642		131.866	146.879	151.725
	0.0	0.000		35.231	-191.74	0.978		153.188	163.534	166.783
C5	0.5	0.516		23.035	-127.75	0.9837		136.696	151.066	155.681
C5	0.0	0.000		33.924	-185.05	0.9723		152.676	163.398	166.771
R	0.0	0.000		39.582	-214.6	0.9722		156.977	166.380	169.319
R	0.3	0.313		29.406	-161.59	0.9714		148.871	160.997	164.837
R	0.5	0.516		23.896	-132.53	0.9707		139.854	154.001	158.533
R	0.4	0.415		23.158	-129.28	0.9619		142.267	157.140	161.914
R	0.2	0.209		31.748	-173.98	0.9824		152.059	163.498	167.106
R	0.1	0.104		37.189	-202.15	0.9711		155.504	165.436	168.548
	Field Data: 15T			39.755	-214.73	0.993		154.064	163.251	166.122
	Field Data: 14T			42.289	-235.12	0.9891		184.506	194.831	198.050
	Field Data: 13T			45.573	-260.09	0.9965		219.117	230.473	234.005
	Field Data: 12T			46.198	-270.92	0.9923		257.525	270.686	274.778

8.1.3 Oxford 1

	Percent Strain			Best Linear Fit			Critical Current (A)		
	Setting	Actual		n-value	Intercept	R^2-value		Ic - 10 µV	Ic - 100 µV	Ic - 200 µV
	0.0	0.000		23.287	-135.40	0.9326		180.061	198.775	**201.872**
	0.1	0.104		25.673	-147.70	0.9627		179.423	196.259	**200.318**
	0.2	0.209		24.757	-142.88	0.9800		178.944	196.385	**201.867**
	0.3	0.313		27.465	-156.84	0.9818		178.380	193.980	198.938
	0.4	0.415		28.784	-162.95	0.9768		173.928	188.413	193.005
	0.5	0.516		28.051	-157.96	0.9831		166.593	180.844	185.369
	0.3	0.313		30.763	-174.23	0.9827		180.090	194.087	198.510
	0.0	0.000		25.347	-146.37	0.9006		182.003	199.310	**203.013**
	0.5	0.516		27.090	-153.00	0.9720		166.322	181.078	185.771
	0.6	0.615		27.301	-152.89	0.9723		159.234	173.247	177.701
	0.3	0.313		28.824	-163.98	0.9714		178.970	193.853	198.571
	0.7	0.714		29.326	-161.74	0.9588		151.720	164.113	168.038
	0.6	0.615		28.924	-161.17	0.9587		159.514	172.732	176.921
	0.5	0.516		27.112	-153.06	0.9748		166.001	180.715	185.395
	0.3	0.313		29.187	-165.83	0.9471		178.768	193.442	198.091
	0.0	0.000		24.358	-140.84	0.9632		179.162	196.924	202.608
R	0.0	0.000		28.904	-165.62	0.7968		186.718	**202.931**	
	0.6	0.615		20.888	-119.55	0.9632		153.077	170.917	176.684
	0.0	0.000		23.091	-134.15	0.9765		178.260	196.953	202.954
C5	0.5	0.516		25.242	-143.41	0.9780		165.406	181.204	186.249
C5	0.0	0.000		25.041	-144.49	0.9876		179.924	197.253	202.790
R	0.0	0.000		29.374	-168.29	0.8605		188.071	**202.978**	
R	0.3	0.313		29.276	-166.75	0.9688		181.589	196.448	201.154
R	0.5	0.516		32.014	-179.01	0.9597		170.686	183.414	187.429
R	0.4	0.415		26.603	-151.88	0.9839		175.115	190.947	195.988
R	0.2	0.209		30.868	-175.76	0.9705		185.928	200.327	**204.344**
R	0.1	0.104		33.377	-189.48	0.9236		189.354	202.879	**204.485**
	Field Data: 15T			23.207	-134.97	0.9559		179.949	198.719	**202.918**
	Field Data: 14T			19.874	-120.91	0.8719		211.888	**233.993**	
	Field Data: 13T			28.334	-171.85	0.8135		258.444	**276.377**	
	Field Data: 12T			28.840	-178.96	0.7408		299.992	**317.567**	

8.1.4 Oxford 2

	Percent Strain			Best Linear Fit				Critical Current (A)	
	Setting	Actual		n-value	Intercept	R^2-value		Quenched Value	
	0.0	0.000						**174.627**	
	0.1	0.104						**172.178**	
	0.2	0.209						**183.423**	
	0.3	0.313						**188.688**	
	0.4	0.415						**185.016**	
	0.5	0.516						**169.758**	
	0.3	0.313						**169.821**	
	0.0	0.000						---	
	0.5	0.516						**167.893**	
	0.6	0.615						**162.395**	
	0.3	0.313						---	
	0.7	0.714						**161.394**	
	0.6	0.615						---	
	0.5	0.516						---	
	0.3	0.313						---	
	0.0	0.000						---	
R	0.0	0.000						---	
	0.6	0.615						---	
	0.0	0.000						---	
C5	0.5	0.516						---	
C5	0.0	0.000						---	
R	0.0	0.000						---	
R	0.3	0.313						---	
R	0.5	0.516						---	
R	0.4	0.415						---	
R	0.2	0.209						---	
R	0.1	0.104						---	
	Field Data: 15T							**173.433**	
	Field Data: 14T							**189.673**	
	Field Data: 13T							**195.787**	
	Field Data: 12T							**194.062**	

8.2 High Bending Results (Day 2)

8.2.1 Hitachi 3

	Percent Strain		Best Linear Fit			Critical Current (A)		
	Setting	Actual	n-value	Intercept	R^2-value	Ic - 10 µV	Ic - 100 µV	Ic - 200 µV
	0.6	0.612	17.411	-100.27	0.9843	138.187	157.726	164.132
	0.7	0.708	15.105	-87.741	0.9787	127.942	149.010	156.007
	0.8	0.800	13.219	-77.621	0.9677	118.890	141.513	149.131
	0.9	0.889	11.603	-68.974	0.9406	109.776	133.873	142.114
	1.0	0.973	10.341	-62.113	0.9846	100.319	125.339	134.029
	1.2	1.124	10.512	-61.444	0.9711	87.335	108.722	116.133
	1.4	1.254	9.0636	-53.638	0.9413	75.399	97.206	104.932
	1.2	1.124	9.8231	-58.271	0.9616	86.505	109.356	117.351
	1.0	0.973	10.703	-63.745	0.9687	99.980	123.979	132.273
	0.8	0.800	13.351	-78.496	0.9439	121.086	143.878	151.545
	0.6	0.612	16.221	-94.279	0.9610	137.119	158.032	164.931
	0.4	0.414	25.704	-145.42	0.9789	163.205	178.500	183.379
	0.2	0.208	29.864	-168.27	0.9751	172.503	186.330	190.705
	0.0	0.000	35.606	-198.66	0.9739	176.504	188.295	191.997
R	0.0	0.000	33.264	-186.94	0.9679	178.617	191.420	195.450
R	0.2	0.208	29.054	-163.69	0.9667	170.097	184.126	188.571
R	0.4	0.414	22.149	-126.71	0.9781	158.863	176.267	181.870
R	0.6	0.612	18.406	-106.10	0.9790	145.318	164.683	171.003
R	0.8	0.800	13.699	-80.699	0.9743	125.897	148.941	156.671
R	1.0	0.973	13.264	-77.167	0.9740	113.042	134.472	141.686
R	1.2	1.124	7.1709	-46.08	0.8914	82.251	113.395	124.903
R	1.4	1.254	9.2045	-55.167	0.9790	83.324	107.007	115.376
	1.4	1.254	8.7536	-52.669	0.9768	78.664	102.332	110.765
C1	1.4	1.254	8.3179	-50.249	0.9744	73.913	97.487	105.959
C3	1.4	1.254	8.2366	-50.081	0.9695	75.563	99.935	108.709
C4	1.4	1.254	8.7959	-52.597	0.9858	76.401	99.264	107.403
C4	1.2	1.124	9.5349	-57.249	0.9580	88.928	113.219	121.756
C4	1.0	0.973	11.774	-69.193	0.9746	104.460	127.023	134.726
C4	0.8	0.800	13.165	-78.192	0.9661	126.618	150.818	158.972
C4	0.6	0.612	18.675	-107.99	0.9805	149.666	169.306	175.708
C4	0.4	0.414	26.689	-151.71	0.9114	171.168	186.591	**188.982**
C4	0.2	0.208	40.211	-223.61	0.8737	181.520	**190.463**	
C4	0.0	0.000	38.804	-216.40	0.9516	182.027	193.155	196.636
	Field Data: 15T		18.319	-104.90	0.9693	139.360	158.025	164.119
	Field Data: 14T		18.258	-108.01	0.9612	167.988	190.568	197.941
	Field Data: 13T		20.501	-123.49	0.9687	204.052	228.307	236.158
	Field Data: 12T		24.347	-147.14	0.9763	232.671	255.750	263.135

172

8.2.2　Hitachi 4

	Percent Strain			Best Linear Fit				Critical Current (A)		
	Setting	Actual		n-value	Intercept	R^2-value		Ic - 10 µV	Ic - 100 µV	Ic - 200 µV
	0.6	0.612		17.923	-101.51	0.9786		128.597	146.226	151.992
	0.7	0.708		15.18	-86.979	0.9643		118.751	138.202	144.659
	0.8	0.800		13.21	-76.574	0.9814		110.141	131.115	138.178
	0.9	0.889		11.841	-69.157	0.945		101.390	123.154	130.578
	1.0	0.973		11.045	-64.814	0.968		95.455	117.581	125.196
	1.2	1.124		9.6292	-56.913	0.9745		82.138	104.326	112.113
	1.4	1.254		9.3262	-54.573	0.9696		73.752	94.406	101.690
	1.2	1.124		9.6696	-57.222	0.9776		83.257	105.642	113.493
	1.0	0.973		10.771	-63.606	0.9726		95.819	118.658	126.545
	0.8	0.800		13.039	-75.993	0.9771		112.041	133.681	140.980
	0.6	0.612		15.999	-92.121	0.9783		128.238	148.088	154.645
	0.4	0.414		21.961	-123.34	0.9768		142.268	157.995	163.061
	0.2	0.208		27.327	-150.91	0.9838		147.392	160.349	164.469
	0.0	0.000		28.906	-163.01	0.9807		170.536	184.676	189.158
R	0.0	0.000		35.565	-197.63	0.9624		172.463	183.999	187.620
R	0.2	0.208		28.082	-157.73	0.9685		164.303	178.343	182.800
R	0.4	0.414		21.909	-124.71	0.9714		153.241	170.223	175.694
R	0.6	0.612		19.366	-110.45	0.9897		142.086	160.025	165.857
R	0.8	0.800		14.425	-83.99	0.9905		123.946	145.398	152.555
R	1.0	0.973		12.03	-70.669	0.9914		106.922	129.477	137.156
R	1.2	1.124		12.419	-71.273	0.9756		96.969	116.722	123.422
R	1.4	1.254		9.9889	-58.682	0.9902		83.659	105.347	112.917
	1.4	1.254		10.429	-60.221	0.9638		80.440	100.313	107.207
C1	1.4	1.254		9.356	-55.121	0.9878		77.137	98.662	106.249
C3	1.4	1.254		10.02	-58.33	0.9607		79.669	100.251	107.431
C4	1.4	1.254		10.354	-59.879	0.9713		80.339	100.348	107.296
C4	1.2	1.124		10.92	-63.549	0.9787		89.567	110.592	117.840
C4	1.0	0.973		12.126	-70.578	0.9727		102.269	123.655	130.929
C4	0.8	0.800		15.042	-86.66	0.9684		121.468	141.560	148.236
C4	0.6	0.612		18.321	-105.05	0.976		140.386	159.187	165.325
C4	0.4	0.414		---	---	---		---	---	---
C4	0.2	0.208		---	---	---		---	---	---
C4	0.0	0.000		---	---	---		---	---	---
	Field Data: 15T			17.923	-101.51	0.9635		128.597	146.226	151.992
	Field Data: 14T			21.409	-123.21	0.9793		160.688	178.934	184.823
	Field Data: 13T			17.672	-106.8	0.9796		185.862	211.728	220.198
	Field Data: 12T			20.008	-122.79	0.9861		224.562	251.951	260.832

8.2.3 Oxford 3

	Percent Strain			Best Linear Fit			Critical Current (A)		
	Setting	Actual		n-value	Intercept	R^2-value		Ic - 10 µV	Ic - 100 µV	Ic - 200 µV
	0.6	0.612		27.623	-155.75	0.9905		166.492	180.965	185.563
	0.7	0.708		29.291	-163.1	0.9834		159.908	172.986	177.129
	0.8	0.800		26.536	-147.79	0.9875		152.094	165.881	170.271
	0.9	0.889		25.32	-139.87	0.9873		141.600	155.081	159.385
	1.0	0.973		22.846	-125.89	0.9796		131.295	145.218	**148.373**
	1.2	1.124		13.811	-78.719	0.9532		104.873	123.900	**125.623**
	1.4	1.254		8.9693	-53.294	0.9933		75.919	98.140	106.025
	1.2	1.124		8.4217	-51.583	0.9616		82.108	107.926	117.184
	1.0	0.973		7.9754	-50.184	0.9665		88.172	117.684	128.369
	0.8	0.800		7.2125	-47.394	0.9432		96.183	132.358	**135.057**
	0.6	0.612		8.1433	-52.488	0.863		106.684	**138.52**	
	0.4	0.414		9.5172	-59.88	0.8065		118.206	**143.172**	
	0.2	0.208		11.369	-68.853	0.8942		119.622	**143.263**	
	0.0	0.000		16.117	-92.38	0.8309		125.795	**143.741**	
R	0.0	0.000		15.737	-90.51	0.8016		125.533	**139.545**	
R	0.2	0.208		10.119	-63.07	0.8645		121.979	**145.317**	
R	0.4	0.414		9.1125	-57.877	0.9149		117.281	**143.672**	
R	0.6	0.612		9.9682	-61.641	0.9138		113.655	**139.901**	
R	0.8	0.800		8.1419	-51.912	0.9711		99.477	131.991	**134.646**
R	1.0	0.973		9.0335	-55.394	0.9806		92.886	119.853	129.411
R	1.2	1.124		8.4458	-51.588	0.9825		81.130	106.557	115.671
R	1.4	1.254		8.1314	-49.084	0.9947		70.674	93.808	102.155
	1.4	1.254		8.1738	-49.362	0.9867		71.522	94.794	103.183
C1	1.4	1.254		7.6243	-46.782	0.9953		69.363	93.819	102.748
C3	1.4	1.254		8.5381	-51	0.9735		72.216	94.570	102.568
C4	1.4	1.254		9.5643	-55.758	0.9838		75.034	95.459	102.634
C4	1.2	1.124		8.4498	-51.492	0.9689		80.046	105.120	114.107
C4	1.0	0.973		8.6776	-53.592	0.9778		90.882	118.499	**125.417**
C4	0.8	0.800		8.6886	-55.177	0.9247		108.448	**130.779**	
C4	0.6	0.612		9.736	-60.275	0.8657		110.581	**132.669**	
C4	0.4	0.414		11.906	-70.951	0.8555		114.980	**134.433**	
C4	0.2	0.208		---	---	---		---	---	---
C4	0.0	0.000		---	---	---		---	---	---
	Field Data: 15T			27.623	-155.75	0.9615		166.492	180.965	185.563
	Field Data: 14T			31.374	-181.59	0.9825		205.825	221.499	226.447
	Field Data: 13T			35.372	-209.69	0.9773		249.471	266.250	271.519
	Field Data: 12T			36.409	-221.72	0.9885		296.650	316.016	322.090

8.2.4 Oxford 4

	Percent Strain			Best Linear Fit			Critical Current (A)		
	Setting	Actual		n-value	Intercept	R^2-value		Ic - 10 µV	Ic - 100 µV	Ic - 200 µV
	0.6	0.612		30.621	-171.62	0.9517		169.481	182.716	186.900
	0.7	0.708		31.422	-174.44	0.9644		162.657	175.024	178.928
	0.8	0.800		26.451	-147.35	0.9839		152.074	165.906	170.311
	0.9	0.889		24.204	-134.44	0.9732		142.228	156.423	160.967
	1.0	0.973		20.334	-113.44	0.9798		130.084	145.681	150.733
	1.2	1.124		13.559	-77.139	0.9706		101.839	120.689	127.019
	1.4	1.254		8.8793	-52.654	0.9879		73.888	95.762	103.537
	1.2	1.124		7.8738	-48.834	0.9512		78.794	105.559	115.273
	1.0	0.973		9.4888	-57.519	0.9558		93.587	119.289	128.330
	0.8	0.800		8.5684	-53.811	0.9558		98.859	129.337	**136.364**
	0.6	0.612		9.2309	-57.922	0.9536		110.981	142.423	**148.045**
	0.4	0.414		9.8478	-61.376	0.9361		117.341	148.250	**155.252**
	0.2	0.208		11.627	-70.514	0.9426		124.194	151.394	**155.962**
	0.0	0.000		13.099	-78.019	0.8591		128.116	**151.793**	
R	0.0	0.000		8.8812	-57.421	0.7714		126.265	**160.462**	
R	0.2	0.208		10.855	-67.164	0.8841		128.530	158.901	**160.094**
R	0.4	0.414		11.406	-69.704	0.9202		127.009	155.420	**158.966**
R	0.6	0.612		10.942	-66.772	0.9526		119.310	147.254	**154.918**
R	0.8	0.800		11.182	-66.975	0.9727		109.645	134.716	143.331
R	1.0	0.973		9.7027	-58.522	0.9785		93.897	119.047	127.862
R	1.2	1.124		9.2421	-55.002	0.9776		80.456	103.218	111.257
R	1.4	1.254		8.7193	-51.128	0.9722		67.120	87.406	94.638
	1.4	1.254		8.0517	-48.373	0.9737		67.566	89.934	98.019
C1	1.4	1.254		8.466	-50.448	0.9737		70.247	92.204	100.071
C3	1.4	1.254		7.8811	-47.748	0.9855		68.374	91.575	99.994
C4	1.4	1.254		8.5535	-50.979	0.9848		71.565	93.672	101.579
C4	1.2	1.124		8.5611	-51.777	0.9639		78.259	102.410	111.046
C4	1.0	0.973		8.9095	-54.223	0.9535		86.840	112.450	121.548
C4	0.8	0.800		9.7422	-59.125	0.9279		98.070	124.217	**133.28**
C4	0.6	0.612		8.4853	-53.462	0.9554		99.241	130.179	141.260
C4	0.4	0.414		9.0687	-55.43	0.9641		91.725	118.238	**125.724**
C4	0.2	0.208		9.581	-58.01	0.8474		94.298	119.915	**126.708**
C4	0.0	0.000		7.9693	-50.32	0.8959		90.105	120.290	**126.989**
	Field Data: 15T			30.621	-171.62	0.9505		169.481	182.716	186.900
	Field Data: 14T			35.376	-203.5	0.9692		209.350	223.430	227.851
	Field Data: 13T			41.088	-242.01	0.9582		254.257	268.913	273.488
	Field Data: 12T			42.377	-257.3	0.964		308.183	325.392	330.758

9.0 Appendix II: Photos

9.1 Preparation
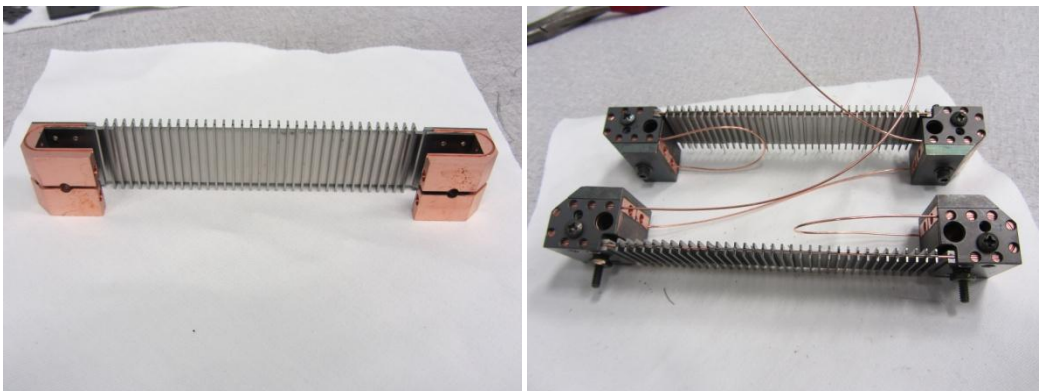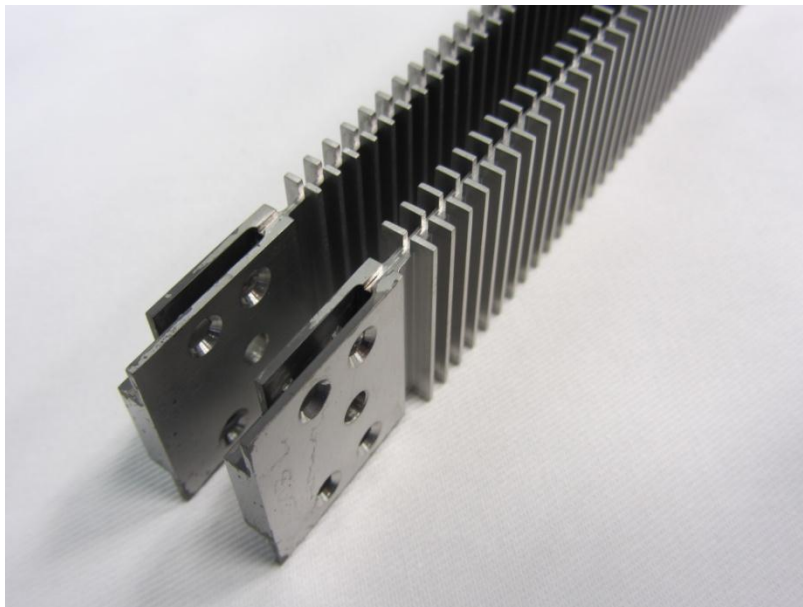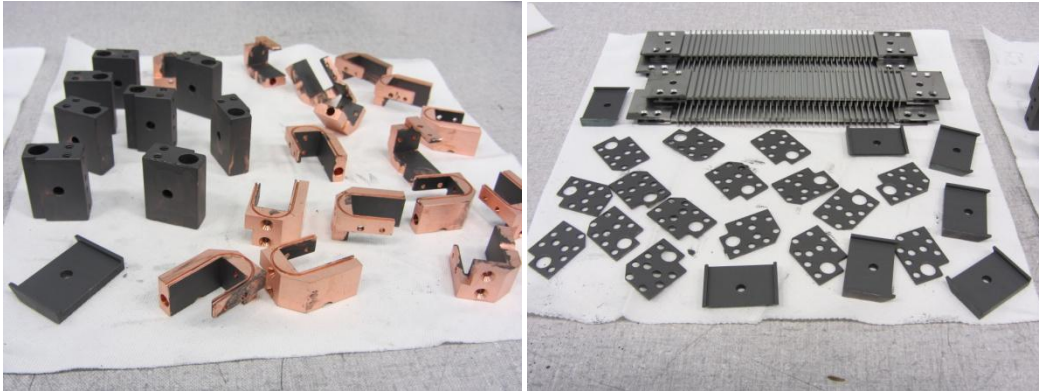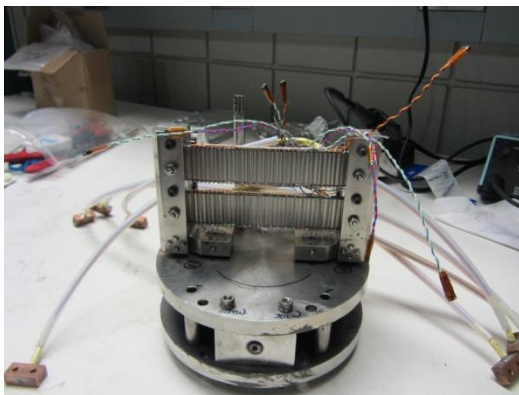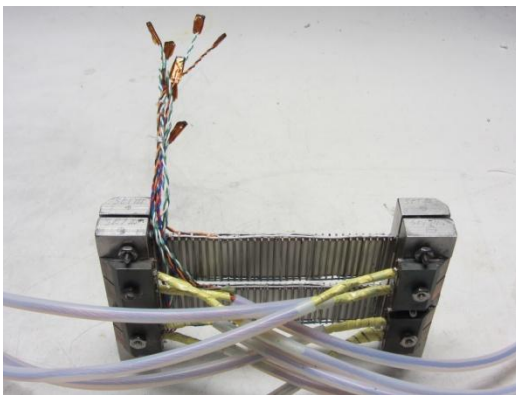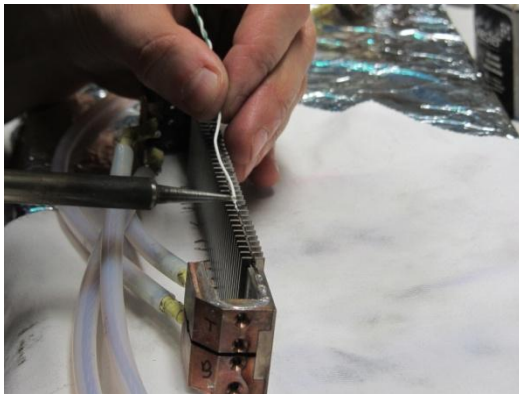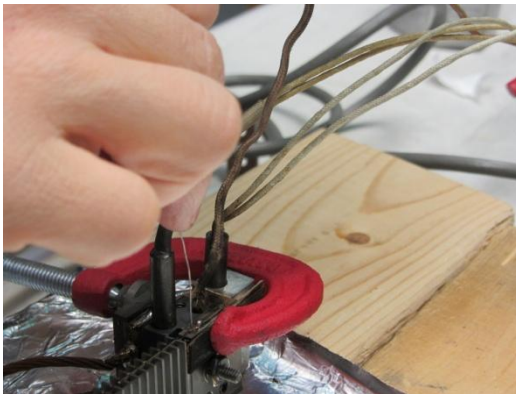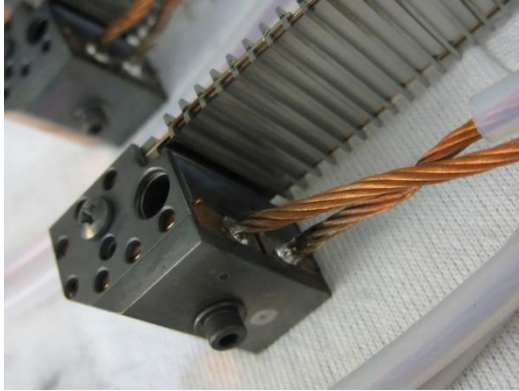
9.2 Experimental Process
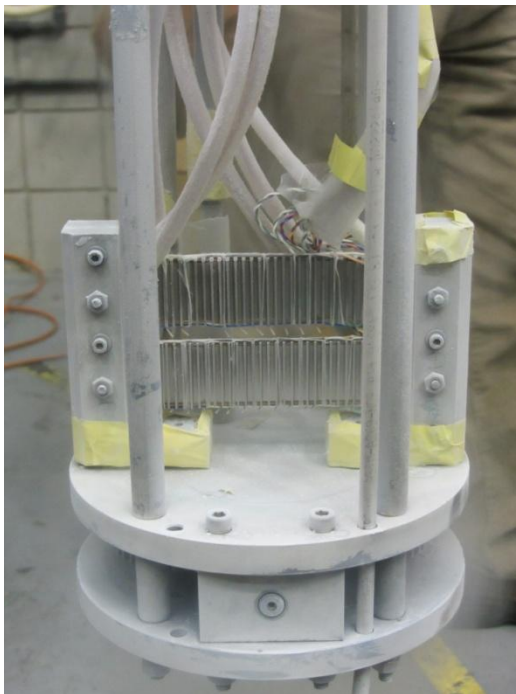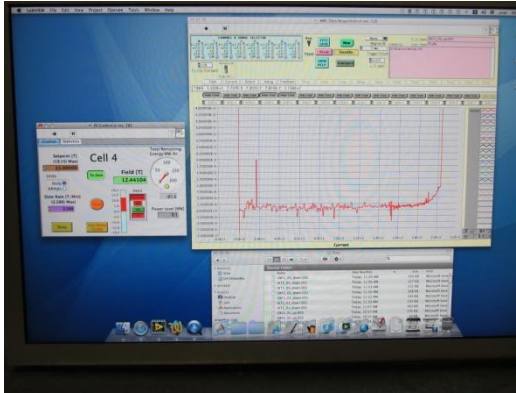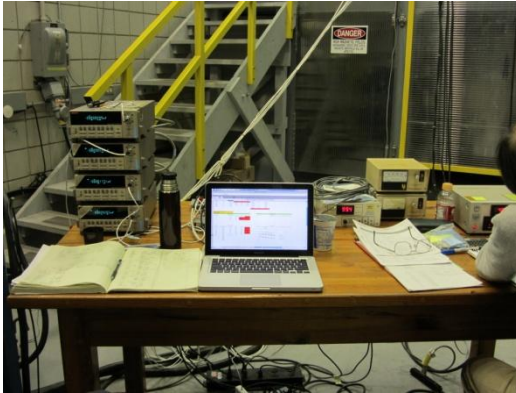
10.0 Appendix III: ANSYS® Script

10.1 New HB Sample Holder with Lorentz Load

```
!Changes Working Directory
/CWD,'E:\Pure Bending Research\Simulations\Gen 4 Design\High Bending\HB G4 LL (1.4%)'

!Changes File Name
/FILNAME,HB_G4_LL_14,0

!Inputs Solid Model
/AUX15
!*
IOPTN,IGES,NODEFEAT
IOPTN,MERGE,YES
IOPTN,SOLID,YES
IOPTN,SMALL,YES
IOPTN,GTOLER, DEFA
IGESIN,'Gen 4 HB Model','IGS',' '
VPLOT
!*

!Applies Volume Numbers
/PNUM,VOLU,1
/PNUM,AREA,1
/PNUM,LINE,1

!Makes Isometric Plot of Area
VPLOT
/VIEW,1,1,1,1
/ANG,1
/REP,FAST
/AUTO,1
/REP,FAST


!!!!!!!!!!!!!!!!!!!!!!!!!!!!!!!!!!!!!!!!!!!!!!!!!!!!!!!!!!!!!!!!!!!!!
!Solution Pre-Processor
/PREP7

ET,1,SOLID95    !Define element type
MPTEMP,1,4      !Define a temperature table, 4K

!Define material properties for Ti-6Al-4V
MPDATA,EX,1,1,132591.5          !Youngs Modulus [MPa]
MPDATA,PRXY,1,1,0.34   !Poisson's Ratio
MPDATA,MU,1,1,0.2        !Coefficient of Friction
TB,MISO,1,1,5                  !Define mutli-linear isotropic properties
TBTEMP,4
TBPT,,.0125,1657.4
TBPT,,.013,1709.9
TBPT,,.014,1758.16
```

```
TBPT,,.015,1785.74
TBPT,,.016,1792.64

!Define material properties for Cu
MPDATA,EX,2,1,110000    !Youngs Modulus [MPa]
MPDATA,PRXY,2,1,0.343            !Poisson's Ratio
MPDATA,MU,2,1,0.2        !Coefficient of Friction

!Define material properties for SS316
MPDATA,EX,3,1,201397.5
MPDATA,PRXY,3,1,0.33

!Glue volumes
ALLSEL
VGLUE,ALL

!Seperate bending arm along beam axis
WPCSYS
VSBW,3

!Seperates bending arms to create axis of rotation
WPCSYS
WPOFFS,-37.79139,-36.970
WPROTA,,,-90
VSBW,1
VSBW,4

!Creates strands
WPCSYS
WPOFFS,,12.5258
WPROTA,,,90
CYL4,0,0,.41,,,,-58.1914   !Cylindrical Strand Top
WPCSYS
WPOFFS,,-12.5258
WPROTA,,,90
CYL4,0,0,.41,,,,-58.1914   !Cylindrical Strand Bottom

!Makes Isometric Plot of Area
APLOT
/VIEW,1,1,1,1
/ANG,1
/REP,FAST
/AUTO,1
/REP,FAST

!Divide top strand into 4 parts
WPCSYS
WPOFFS,,12.5258
WPROTA,,45
VSBW,4
WPCSYS
WPOFFS,,12.5258
WPROTA,,135
VSBW,8
VSBW,9
```

```
!Divide bottom strand into 4 parts
WPCSYS
WPOFFS,,-12.5258
WPROTA,,45
VSBW,7
WPCSYS
WPOFFS,,-12.5258
WPROTA,,135
VSBW,9
VSBW,12

!Define Orientation Nodes
WPCSYS
WPOFFS,0,12.5258
WPROTA,,-90
LSBW,29
WPCSYS
WPOFFS,0,-12.5258
WPROTA,,-90
LSBW,68
WPCSYS

!Makes Isometric Plot
/VIEW,1,1,1,1
/ANG,1
/REP,FAST
/AUTO,1
/REP,FAST

!Apply Ti material properties to sample holder
VSEL,S,,,2
VATT,1

!Apply Cu material properties to copper wire
VSEL,S,,,4,8,4
VSEL,A,,,10,11,1
VSEL,A,,,7,9,2
VSEL,A,,,13,14,1
VATT,2

!Apply SS material properties to bending arms
VSEL,S,,,1,3,2
VSEL,A,,,5,6,1
VATT,3

!!!!!!!!!!!!!!! Surface Effect Elements !!!!!!!!!!!
!Defines Surface Effect Element Top
ET,8,SURF156    !3D structural surface line load effect
KEYOPT,8,4,1    !No midside node
KEYOPT,8,5,0    !Has orentation node

!Defines Surface Effect Element Bot
ET,9,SURF156    !3D structural surface line load effect
KEYOPT,9,4,1    !No midside node
KEYOPT,9,5,0    !Has orentation node
```

```
!Load elements (Top)
TYPE,8
REAL,10
LSEL,S,,,970
LESIZE,ALL, , ,200, , , , ,1
LATT,2,10,8,,69
LMESH,ALL

!Load elements (Bot)
TYPE,9
REAL,11
LSEL,S,,,991
LESIZE,ALL, , ,200, , , , ,1
LATT,2,11,9,,70
LMESH,ALL


!Mesh all parts with tetrahedral elements
ALLS
TYPE,1
MSHAPE,1,3D    !3D tetrahedral elements

!Channel Walls
ASEL,S, , ,423,503,5        !Top Outside
ASEL,A, , ,416
ASEL,A, , ,331,411,5        !Top Inside
ASEL,A, , ,515
ASEL,A, , ,419,504,5        !Bot Outside
ASEL,A, , ,332,412,5        !Bot Inside
ASEL,A, , ,516
ASEL,A, , ,417,418,1        !Base T/B
LSLA,S
LESIZE,ALL,0.22,,,,,,1

!Selects Sides of Ribs
ASEL,S, , ,574,619,3
ASEL,A, , ,330,410,5
ASEL,A, , ,573,618,3
ASEL,A, , ,571,572,1
ASEL,A, , ,518,566,3
ASEL,A, , ,422,502,5
ASEL,A, , ,519,567,3
ASEL,A, , ,415
ASEL,A, , ,568,621,53
ASEL,A, , ,509,568,58
ASEL,A, , ,507
LSLA,S
LESIZE,ALL,0.95,,,,,,1

!Strand ends
ASEL,S, , ,12,34,22        !Top Sym
ASEL,A, , ,45,49,4
ASEL,A, , ,30,39,9        !Bot Sym
ASEL,A, , ,59,63,4
```

```
ASEL,A, , ,10,33,23        !Top Bonded
ASEL,A, , ,43,47,4
ASEL,A, , ,29,38,9         !Bot Bonded
ASEL,A, , ,57,61,4
LSLA,S
LESIZE,ALL,0.22,,,,,,1

!Strand outer areas
ASEL,S, , ,40,48,8         !Top Outer
ASEL,A, , ,35,44,9         !Top Inner
ASEL,A, , ,37,42,5         !Top T/B
ASEL,A, , ,54,62,8         !Bot Outer
ASEL,A, , ,41,58,17        !Bot Inner
ASEL,A, , ,51,56,5         !Bot T/B
LSLA,S
LESIZE,ALL,0.22,,,,,,1

!Mesh strands
SMRTSIZE,3      !Mesh size -- Fine 1 - 10 Course
VSEL,S,,,4,8,4
VSEL,A,,,10,11,1
VMESH,ALL
SMRTSIZE,6      !Mesh size -- Fine 1 - 10 Course
VSEL,S,,,7,9,2
VSEL,A,,,13,14,1
VMESH,ALL

!Mesh sample holder
SMRTSIZE,3      !Mesh size -- Fine 1 - 10 Course
VSEL,S,,,2
VMESH,ALL

!Mesh bending arm
SMRTSIZE,6      !Mesh size -- Fine 1 - 10 Course
VSEL,S,,,1,3,2
VSEL,A,,,5,6,1
VMESH,ALL
ALLS


!!!!!!!!! Creating Strand Contact Pairs !!!!!!!!!
!Defines Target Element Type
ET,2,TARGE170 !3D target element

!Defines Contact Element Slidding
ET,3,CONTA174!3D 4node surface-to-surface contact element
KEYOPT,3,1,0    !Contact DOF (UX,UY,UZ)
KEYOPT,3,5,4    !Auto ICONT
KEYOPT,3,9,1    !Exclude initial penetration/gap effects
KEYOPT,3,10,2 !Update contact stiffness each iteration automatically
KEYOPT,3,12,0 !Standard

!Defines Contact Element slidding & no seperation
ET,4,CONTA174!3D 4node surface-to-surface contact element
KEYOPT,4,1,0    !Contact DOF (UX,UY,UZ)
```

184

```
KEYOPT,3,5,4    !Auto ICONT
KEYOPT,4,9,1    !Exclude initial penetration/gap effects
KEYOPT,4,10,2  !Update contact stiffness each iteration automatically
KEYOPT,4,12,2  !No seperation - sliding permitted

!Defines Contact Element Bonded
ET,5,CONTA174!3D 4node surface-to-surface contact element
KEYOPT,5,1,0    !Contact DOF (UX,UY,UZ)
KEYOPT,3,5,4    !Auto ICONT
KEYOPT,5,12,3  !Bonded Connection


!!!!!!!!!!! Top Strand !!!!!!!!!!!
!! Contact Pair 1 (Outside)
!Creating Target Elements
TYPE,2
REAL,1
ASEL,S, , ,423,503,5        !Top Outside
ASEL,A, , ,416
NSLA,S,1
ESLN,S,0
ESURF, ,TOP,

!Creating Contact Elements
TYPE,3
REAL,1
ASEL,S, , ,40,48,8          !Top Outer
NSLA,S,1
ESLN,S,0
ESURF, ,TOP,

!! Contact Pair 2 (Inside)
!Creating Target Elements
TYPE,2
REAL,2
ASEL,S, , ,331,411,5        !Top Inside
ASEL,A, , ,515
NSLA,S,1
ESLN,S,0
ESURF, ,TOP,

!Creating Contact Elements
TYPE,3
REAL,2
ASEL,S, , ,35,44,9          !Top Inner
NSLA,S,1
ESLN,S,0
ESURF, ,TOP,

!! Contact Pair 3 (Bottom)
!Creating Target Elements
TYPE,2
REAL,3
ASEL,S, , ,417
NSLA,S,1
```

```
ESLN,S,0
ESURF, ,TOP,

!Creating Contact Elements
TYPE,4
REAL,3
ASEL,S, , ,42
NSLA,S,1
ESLN,S,0
ESURF, ,TOP,

!! Contact Pair 4 (End)
!Creating Target Elements
TYPE,2
REAL,4
ASEL,S, , ,514
AMESH,ALL

!Creating Contact Elements
TYPE,5
REAL,4
ASEL,S, , ,10,33,23          !Top Bonded
ASEL,A, , ,43,47,4
AMESH,ALL
ALLS

!!!!!!!!!! Bottom Strand !!!!!!!!!!
!! Contact Pair 5 (Outside)
!Creating Target Elements
TYPE,2
REAL,5
ASEL,S, , ,419,504,5         !Bot Outside
NSLA,S,1
ESLN,S,0
ESURF, ,TOP,

!Creating Contact Elements
TYPE,3
REAL,5
ASEL,S, , ,54,62,8           !Bot Outer
NSLA,S,1
ESLN,S,0
ESURF, ,TOP,

!! Contact Pair 6 (Inside)
!Creating Target Elements
TYPE,2
REAL,6
ASEL,S, , ,332,412,5         !Bot Inside
ASEL,A, , ,516
NSLA,S,1
ESLN,S,0
ESURF, ,TOP,

!Creating Contact Elements
```

186

```
TYPE,3
REAL,6
ASEL,S, , ,41,58,17          !Bot Inner
NSLA,S,1
ESLN,S,0
ESURF, ,TOP,


!! Contact Pair 7 (Bottom)
!Creating Target Elements
TYPE,2
REAL,7
ASEL,S, , ,418
NSLA,S,1
ESLN,S,0
ESURF, ,TOP,


!Creating Contact Elements
TYPE,4
REAL,7
ASEL,S, , ,51
NSLA,S,1
ESLN,S,0
ESURF, ,TOP,


!! Contact Pair 8 (End)
!Creating Target Elements
TYPE,2
REAL,8
ASEL,S, , ,325
AMESH,ALL


!Creating Contact Elements
TYPE,5
REAL,8
ASEL,S, , ,29,38,9          !Bot Bonded
ASEL,A, , ,57,61,4
AMESH,ALL



!!!!!!!!! Creating Pilot Node For Ration !!!!!!!!!!

!Defines Target Element Type
ET,6,TARGE170              !3D target element
KEYOPT,6,2,0               !Automatic Boundary Conditions
KEYOPT,6,4,111111          !DOF (All 6 DOF)

!Defines Contact Element Slidding
ET,7,CONTA174             !3D 8node surface-to-surface contact element
KEYOPT,7,12,5             !Bonded (Always)
KEYOPT,7,4,2              !Contact Detection on Nodal Points (Target)
KEYOPT,7,2,2              !Multipoint Contraint Algorithm

!Creating Target Elements
TYPE,6
REAL,9
```

```
KSEL,S,,,24        !Selects Keypoint at Pilot Node Location
KMESH,ALL

!Creating Contact Elements
TYPE,7
REAL,9
ASEL,S,,,5,15,10
ASEL,A,,,19,24,5
NSLA,S,1
ESLN,S,0
ESURF
ALLS



!!!!!!!!!!!!!!!!!!!!!!!!!!!!!!!!!!!!!!!!!!!!!!!!!!!!!!!!!!!!!!!!!!!!!!!!
!Solution Processor
/SOLU

ANTYPE,STATIC              !Specify Solution type
NLGEOM,ON          !Specify large deflection
NROPT,FULL         !Specify full Newton-Raphson option (non-linear eq.)

NSUBST,20,200,0                    !Specify number of substeps
OUTRES,ALL,LAST                    !Write all data for each load step
RESCONTROL,DEFINE,ALL,LAST         !Writes restart info for each load step

!Apply symmetry boundary condition
ASEL,S, , ,507
ASEL,A, , ,12,34,22       !Top Sym
ASEL,A, , ,45,49,4
ASEL,A, , ,30,39,9        !Bot Sym
ASEL,A, , ,59,63,4
DA,ALL,SYMM
ALLS

!Fix all DOF for Axis of rotation
LSEL,S,,,48
DL,ALL,,UX,0
DL,ALL,,UY,0
DL,ALL,,UZ,0
ALLS


!Apply Rotation to Pilot Node (1.4%)
!First load step
NSEL,S,,,252133
D,ALL,UX,0
D,ALL,UY,O
D,ALL,UZ,0
D,ALL,ROTX,0
D,ALL,ROTZ,0
D,ALL,ROTY,0.04
ALLS
SOLVE
```

```
!Second load step
NSEL,S,,,252133
DCUM,ADD
D,ALL,ROTY,0.102          !Applying 0.1%
ALLS
SOLVE

!Third load step
NSEL,S,,,252133
DCUM,ADD
D,ALL,ROTY,0.142          !Applying 0.2%
ALLS
SOLVE

!Fourth load step
NSEL,S,,,252133
DCUM,ADD
D,ALL,ROTY,0.142          !Applying 0.3%
ALLS
SOLVE

!Fifth load step
NSEL,S,,,252133
DCUM,ADD
D,ALL,ROTY,0.142          !Applying 0.4%
ALLS
SOLVE

!Sixth load step
NSEL,S,,,252133
DCUM,ADD
D,ALL,ROTY,0.142          !Applying 0.5%
ALLS
SOLVE

!Seventh load step
NSEL,S,,,252133
DCUM,ADD
D,ALL,ROTY,0.142          !Applying 0.6%
ALLS
SOLVE

!Eight load step
NSEL,S,,,252133
DCUM,ADD
D,ALL,ROTY,0.142          !Applying 0.7%
ALLS
SOLVE

!Ninth load step
NSEL,S,,,252133
DCUM,ADD
D,ALL,ROTY,0.142          !Applying 0.8%
ALLS
SOLVE
```

```
!Tenth load step
NSEL,S,,,252133
DCUM,ADD
D,ALL,ROTY,0.142              !Applying 0.9%
ALLS
SOLVE

!Eleventh load step
NSEL,S,,,252133
DCUM,ADD
D,ALL,ROTY,0.142              !Applying 1.0%
ALLS
SOLVE

!Twelth load step
NSEL,S,,,252133
DCUM,ADD
D,ALL,ROTY,0.142              !Applying 1.1%
ALLS
SOLVE

!Thirteenth load step
NSEL,S,,,252133
DCUM,ADD
D,ALL,ROTY,0.142              !Applying 1.2%
ALLS
SOLVE

!Fourteenth load step
NSEL,S,,,252133
DCUM,ADD
D,ALL,ROTY,0.142              !Applying 1.3%
ALLS
SOLVE

!Fifteenth load step
NSEL,S,,,252133
DCUM,ADD
D,ALL,ROTY,0.142              !Applying 1.4%
ALLS
SOLVE


!!!!!!!!!!!!!!!!!!!!!!!!!!!!!!!!!!!!!!!!!!!!!!!!!!!!!!!!!!!!!!!!!!!!!!!!!
!Solution Processor
/SOLU

!Resumes Analysis from specific bending strain
ANTYPE,0,RESTART,15,LAST,CONTINUE

!Apply symmetry boundary condition
ASEL,S, , ,507
ASEL,A, , ,12,34,22
ASEL,A, , ,45,49,4
```

```
ASEL,A, , ,30,39,9
ASEL,A, , ,59,63,4
DA,ALL,SYMM
ALLS

!Fix pilot node and base
NSEL,S,,,252133
D,ALL,UX,0
D,ALL,UY,0
D,ALL,UZ,0
ALLS


!!!!! Lorentz Load on Top Strand !!!!!
!Load Step L1
SFCUM,ALL,ADD
ESEL,S,TYPE,,8
SFE,ALL,3,PRES,0,-1                !1000 N/m
ALLS
SOLVE

!Load Step L2
SFCUM,ALL,ADD
ESEL,S,TYPE,,8
SFE,ALL,3,PRES,0,-1                !2000 N/m
ALLS
SOLVE

!Load Step L3
SFCUM,ALL,ADD
ESEL,S,TYPE,,8
SFE,ALL,3,PRES,0,-1                !3000 N/m
ALLS
SOLVE

!Load Step L4
SFCUM,ALL,ADD
ESEL,S,TYPE,,8
SFE,ALL,3,PRES,0,-1                !4000 N/m
ALLS
SOLVE

!Load Step L5
SFCUM,ALL,ADD
ESEL,S,TYPE,,8
SFE,ALL,3,PRES,0,-1                !5000 N/m
ALLS
SOLVE


!!!!!!!!!!!!!!!!!!!!!!!!!!!!!!!!!!!!!!!!!!!!!!!!!!!!!!!!!!!!!!!!!!!!!!!
!Solution Post-Processor
/POST1

!Countour Plot of Nodal Solution
```

```
PLNSOL,EPTO,X          !Axial Strain
/VIEW,1,1,1,1
/ANG,1
/REP,FAST
/REPLOT


!Countour Plot of Nodal Solution
VSEL,S,,,4,8,4
VSEL,A,,,10,11,1
VSEL,A,,,7,9,2
VSEL,A,,,13,14,1
ESLV,S                      !Selects only strands
EPLOT
PLNSOL,EPTO,X                      !Axial Strain
/VIEW,1,1,1,1
/ANG,1
/REP,FAST
/REPLOT


!Displacement and Strain Data Collection

!!!!!!!!!!! Strain Within Strand !!!!!!!!!!!
!Defines Path A
PATH,Path-A,2,30,400,
PPATH,1,0,0,12.5258,0.405,0,
PPATH,2,0,-58.1914,12.5258,0.405,0,

!Maps results onto path
PMAP,'UNI ','    '
PDEF, ,EPTO,X,AVG

!Prints results
PRPATH,XG,EPTOX

!Defines Path B
PATH,Path-B,2,30,400,
PPATH,1,0,0,12.5258,0.3,0,
PPATH,2,0,-58.1914,12.5258,0.3,0,

!Maps results onto path
PMAP,'UNI ','    '
PDEF, ,EPTO,X,AVG

!Prints results
PRPATH,XG,EPTOX

!Defines Path C
PATH,Path-C,2,30,400,
PPATH,1,0,0,12.5258,0.2,0,
PPATH,2,0,-58.1914,12.5258,0.2,0,

!Maps results onto path
PMAP,'UNI ','    '
```

```
PDEF, ,EPTO,X,AVG

!Prints results
PRPATH,XG,EPTOX

!Defines Path D
PATH,Path-D,2,30,400,
PPATH,1,0,0,12.5258,0.1,0,
PPATH,2,0,-58.1914,12.5258,0.1,0,

!Maps results onto path
PMAP,'UNI ',' '
PDEF, ,EPTO,X,AVG

!Prints results
PRPATH,XG,EPTOX

!Defines Path E
PATH,Path-E,2,30,400,
PPATH,1,0,0,12.5258,0,0,
PPATH,2,0,-58.1914,12.5258,0,0,

!Maps results onto path
PMAP,'UNI ',' '
PDEF, ,EPTO,X,AVG

!Prints results
PRPATH,XG,EPTOX

!Defines Path F
PATH,Path-F,2,30,400,
PPATH,1,0,0,12.5258,-0.1,0,
PPATH,2,0,-58.1914,12.5258,-0.1,0,

!Maps results onto path
PMAP,'UNI ',' '
PDEF, ,EPTO,X,AVG

!Prints results
PRPATH,XG,EPTOX

!Defines Path G
PATH,Path-G,2,30,400,
PPATH,1,0,0,12.5258,-0.2,0,
PPATH,2,0,-58.1914,12.5258,-0.2,0,

!Maps results onto path
PMAP,'UNI ',' '
PDEF, ,EPTO,X,AVG

!Prints results
PRPATH,XG,EPTOX

!Defines Path H
PATH,Path-H,2,30,400,
```

```
PPATH,1,0,0,12.5258,-0.3,0,
PPATH,2,0,-58.1914,12.5258,-0.3,0,

!Maps results onto path
PMAP,'UNI ','   '
PDEF, ,EPTO,X,AVG

!Prints results
PRPATH,XG,EPTOX

!Defines Path I
PATH,Path-I,2,30,400,
PPATH,1,0,0,12.5258,-0.405,0,
PPATH,2,0,-58.1914,12.5258,-0.405,0,

!Maps results onto path
PMAP,'UNI ','   '
PDEF, ,EPTO,X,AVG

!Prints results
PRPATH,XG,EPTOX


!!!!!!!!!! Vertical Strain and Deformation !!!!!!!!!!
!Symmetry
PATH,Sym,2,30,20,
PPATH,1,0,0,12.5258,0,0,
PPATH,2,0,0,-12.5258,0,0,

!Maps results onto path
PMAP,'UNI ','   '
PDEF, ,EPTO,X,AVG
PDEF, ,U,Z,AVG

!Prints results
PRPATH,XG,YG,UZ,EPTOX


!25mm Offset
PATH,25Offs,2,30,20,
PPATH,1,0,-25,12.5258,0,0,
PPATH,2,0,-25,-12.5258,0,0,

!Maps results onto path
PMAP,'UNI ','   '
PDEF, ,EPTO,X,AVG
PDEF, ,U,Z,AVG

!Prints results
PRPATH,XG,YG,UZ,EPTOX


!45mm Offset
PATH,45Offs,2,30,20,
PPATH,1,0,-45,12.5258,0,0,
```

```
PPATH,2,0,-45,-12.5258,0,0,

!Maps results onto path
PMAP,'UNI ',' '
PDEF, ,EPTO,X,AVG
PDEF, ,U,Z,AVG

!Prints results
PRPATH,XG,YG,UZ,EPTOX


!!!!!!!! Strand Deformation Top !!!!!!!!!!

!Center of Strand
PATH,Path-CM,2,30,400,
PPATH,1,0,0,12.5258,0,0,
PPATH,2,0,-58.1914,12.5258,0,0,

!Maps results onto path
PMAP,'UNI ',' '
PDEF, ,U,Z,AVG
PDEF, ,U,X,AVG

!Prints results
PRPATH,XG,UX,UZ

!!!!!!!!!! Strand Deformation Bot !!!!!!!!!!

!Center of Strand
PATH,Path-CMB,2,30,400,
PPATH,1,0,0,-12.5258,0,0,
PPATH,2,0,-58.1914,-12.5258,0,0,

!Maps results onto path
PMAP,'UNI ',' '
PDEF, ,U,Z,AVG
PDEF, ,U,X,AVG

!Prints results
PRPATH,XG,UX,UZ
```

11.0   Appendix IV: Part Drawings

11.1 High Bending Sample Holder

DETAIL E
SCALE 2 : 1

ISOMETRIC VIEW

FRONT VIEW

SECTION F-F

8 x #2-56 TAP

4 x R.040

4 x R.047***

0.188

0.0315

0.137

68 x 0.094

DETAIL H
SCALE 2 : 1

0.905
0.789
0.155

0.292

0.219

0.160

$0.080^{+.002}_{-.000}$

$0.180 \times 82°$

8 x Ø0.089 THRU ALL

*** NOTE: R.047 ONLY AT FOUR
CORNERS ADJACENT TO CLAMPS

UNLESS OTHERWISE SPECIFIED:	Drawn By:	Nathaniel Allen		Mechanical Engineering Dept. Tufts University
DIMENSIONS ARE IN INCHES TOLERANCES: FRACTIONAL± ANGULAR: MACH± TWO PLACE DECIMAL ± THREE PLACE DECIMAL ±	Date:			
	ENG APPR.	4/12/2013		TITLE:
	COMMENTS:			High Bending Sample Holder
MATERIAL: Ti-6Al-4V				SIZE **A** DWG. NO. REV 1
Quantity: 2 Parts				SCALE: 1:2 WEIGHT: SHEET 2 OF 2
DO NOT SCALE DRAWING				

197

11.2 Low Bending Sample Holder

FRONT VIEW

DETAIL N
SCALE 2 : 1

ISOMETRIC VIEW

SECTION P-P

DETAIL T
SCALE 2 : 1

8 x #2-56 TAP

4 x R.040
4 x R.047***

0.250

0.066

0.905
0.789
0.155
0.292
0.219
0.160

0.137
68 x 0.094

0.080 +.002 -.000

8 x Ø0.089 THRU ALL
Ø0.180 x 82°

*** NOTE: R.047 ONLY AT FOUR
CONERS ADJACENT TO CLAMPS

11.3 Current Terminals

RIGHT VIEW

2 x ⌀0.089 THRU
⌀0.172 x 82°
0.120
0.413
0.296
0.117
0.298
0.750

DETAIL A
SCALE 6:1
0.036
0.034
R.017

FRONT VIEW

R.275
0.500
45.0°
0.250
0.700
0.489
0.789
0.460
0.210
0.080 +.000 -.002
R.040

BOTTOM VIEW

⌀0.070 THRU
⌀0.089 THRU
0.160
0.219
0.292
0.155
0.350
R.072
1.000
0.493
0.513

LEFT VIEW

⌀0.156 ▽ 0.500
0.105
0.303
0.493
0.233 +.000 -.003

ISOMETRIC VIEW

Mechanical Engineering Dept.
Tufts University

TITLE:
Left Copper
Terminator

Drawn By: Nathaniel Allen
Date: 4/12/2013
ENG APPR.
COMMENTS:

UNLESS OTHERWISE SPECIFIED:
DIMENSIONS ARE IN INCHES
TOLERANCES:
FRACTIONAL±
ANGULAR: MACH±
TWO PLACE DECIMAL ±0.01
THREE PLACE DECIMAL ±0.003

MATERIAL: OFHC
Quantity: 8 Parts

DO NOT SCALE DRAWING

SIZE: A
DWG. NO.
REV: 1

SCALE: 2:1   WEIGHT: SHEET 1 OF 1

200

RIGHT VIEW

0.303
Ø0.156 ⊽0.50
0.233 +.000 -.003
0.493

DETAIL A
SCALE 6 : 1
R.017
0.036
0.034

FRONT VIEW

0.250
0.700
0.210
0.080 +.000 -.002
R.040
0.460
0.489
0.789
45.0°
0.500
R.275

BOTTOM VIEW

0.292
0.155
0.493
0.513
R.072
0.350
1.000
Ø0.070 THRU
Ø0.089 THRU
0.160
0.219

LEFT VIEW

0.296
0.117
8 x Ø0.089 THRU
⌵ Ø0.172 x 82°
0.298
0.413
0.120
0.750

ISOMETRIC VIEW

Mechanical Engineering Dept.
Tufts University

TITLE:

Right Copper
Terminator

SIZE DWG. NO.   REV
A   1

SCALE: 2:1 WEIGHT: SHEET 1 OF 1

UNLESS OTHERWISE SPECIFIED:
DIMENSIONS ARE IN INCHES
TOLERANCES:
FRACTIONAL±
ANGULAR: MACH±
TWO PLACE DECIMAL ±0.01
THREE PLACE DECIMAL ±0.003

Drawn By: Nathaniel Allen
Date: 4/12/2013
ENG APPR.
COMMENTS:

MATERIAL: OFHC
Quantity: 8 Parts

DO NOT SCALE DRAWING

201

12.0   References

[1]   D. Harris, "Characterization of Nb3Sn Superconducting Strand Under Pure Bending," M.S. thesis, Dept. Mech. Eng., MIT, Cambridge, MA, 2005.

[2]   J. King, "Effects of Wide Range Bending Strain on Critical Current of Bronze Route Nb3Sn Superconducting Strands," M.S. thesis, Dept. Mech. Eng., Tufts Univ., Medford, MA, 2012.

[3]   W. Buckel, R. Kleiner, *Superconductivity: Fundamentals and Applications,* 2nd ed. Weinheim, Germany: Wiley-VCH, 2004.

[4]   W. Meissner and R. Ochsenfeld, "Ein neuer effekt bei eintritt der supraleitfähigkeit," *Naturwissenschaften*, vol. 21, no. 44, pp. 787–788, Nov., 1993.

[5]   Large Hadron Collider Design Report, "Chapter 7: Main magnets in the arcs," LHC website, http://lhc.web.cern.ch/lhc/LHC-DesignReport.html.

[6]   "Uses for Superconductors." http://www.superconductors.org/Uses.htm, web. June 2012.

[7]   G. R. Polgreen, "Magnetic System of Transportation," U.S. Patent 3 158 765, Nov. 24, 1964.

[8]   ITER technical basis, "The plant description document," *Chapter 2.1 Magnets*, ITER website http://www.naka.jaea.go.jp/ITER/official-J/pdfs/PDD2-12.pdf.

[9]   "ITER: the world's largest tokamak," *Official ITER webpage*, http://www.iter.org/, web. March 2013.

[10]   N. Mitchell, "Summary, assessment and implications of the ITER model coil test results," *Fus. Eng. and Design*, vol. 66–68, pp. 971–993, 2003.

[11]   A. Corte, "Conduttori e Magneti," Official *ENEA webpage*, http://www.fusione.enea.it/SUPERCOND/condmag.html.it Accessed March 2013.

[12]   K. Dulon, "From 100 kg billets to millimeter-thin strands," ITER timeline, http://www.iter.org/newsline/140/340 Accessed March 2013.

[13]   J.W. Ekin, "Strain scaling law for flux pinning in practical superconductors. Part 1: Basic relationship and application to Nb_3Sn conductors", Cryogenics, v 20, n 11, Nov. 1980, p 611-24.

[14]   B. Senkowicz, M. Takayasu, P. Lee, "Effects of bending on cracking and critical current of Nb3Sn ITER wires," *IEEE Trans. on App. Supercond.*, vol. 15, n. 2, pt. III, pp. 3470-473, June 2005.

[15]   A. Allegritti, "Sviluppo E Speriment Azione Di Un Dispositivo Per La Misura Della Corrente Critica Di Fili Superconduttori In Condizioni Di Pura Flessione" B.S. Thesis, Universita' Degli Studi Di Bologna, 2006.

[16]   P. Mallon, "Characterization of Nb_3Sn Superconducting Strands under Wide Range Pure-Bending Strain," M.S. thesis, Dept. Mech. Eng., Tufts Unv., Medford, MA, 2011.

[17]   J. Case, L. Chilver, C. Ross, *Strength of Materials and Structures,* 4th ed. London: Arnold, 1999.

[18]   *Contact Technology Guide*, ANSYS, Inc., Canonsburg, PA, 2009.

[19]   *Aerospace Structural Metals Handbook*, CINDA/USAF CRDA Handbooks, Purdue University, 1993.

[20]   "Mechanical Properties of Copper and Copper Alloys at Low Temperatures," *Copper Development Association Inc.*, http://www.copper.org/resources/properties/144_8/144_8.html, web. March 2013.

[21]   M. Takayasu et al., "Pure Bending Strains of Nb3Sn Wires", *Supercond. Sci. Technol.*, vol. 24, Feb. 2011.